An Investigation of the Structural Phase Transitions in a Weyl Semimetal Using Neutron Scattering

Yu Tao

Jiangsu, China

B.S., Nanjing University, China (2016)

A Dissertation presented to the Graduate Faculty of the University of Virginia in Candidacy for the Degree of Doctor of Philosophy

Department of Physics

University of Virginia

Nov. 2022

Abstract

Two-dimensional (2D) transition metal dichalcogenides (TMDs) have been widely explored due to their exotic quantum behaviors that include a nontrivial band topology, extreme magnetoresistance (XMR), pressure-induced superconductivity, charge density waves and Mott physics. In the last decade or so, TMDs $MoTe_2$ and WTe_2 have garnered attention because their non-centrosymmetric orthorhombic phase is host to Weyl fermions. Bulk $MoTe_2$ and WTe_2 consist of van der Waals bound layers stacked along the c-axis following an A/B-type of stacking sequence, where their electronic band structures can be tuned through layer stacking order. Bulk $MoTe_2$ exhibits a structural phase transition at around 260 K from the high temperature monoclinic 1T' phase to the orthorhombic T_d phase upon cooling. On the other hand, in WTe_2, the orthorhombic phase is presumed to be the stable phase at all temperatures. The transition from 1T' to T_d breaks inversion symmetry and allows the Weyl quasiparticles to emerge. The T_d-1T' transition is accompanied by substantial stacking disorder, the effects of which are not well understood. To this end, the structural properties of $MoTe_2$ and WTe_2 and their solid solutions play a critical role in determining the topological properties of this system. A study of the structural mechanism leading to the nontrivial topology will provide insights into the nature of the Weyl electronic structure.

The structural phase diagram of $Mo_{1-x}W_xTe_2$ has been explored. The T_d-1T' structural phase transition and associated stacking disorder across the phase boundary were investigated using elastic neutron scattering and X-ray diffraction (XRD). In $MoTe_2$, a cell doubling structure T_d*, present between T_d and 1T', was observed. The T_d* phase appears only on warming from T_d, whereas on cooling from 1T', broad diffuse scattering was observed across the structural phase transition instead. The T_d* structure consists of four layers in the unit cell and is constructed by an 'AABB' layer stacking sequence rather than the 'AA' and 'AB' sequences of the T_d and 1T' phases,

respectively. Compared with T_d, the T_d* phase has additional Bragg peaks at half integer L, which appears to be orthorhombic. However, structural refinements showed that T_d* is centrosymmetric with the same space group as the monoclinic 1T' phase.

The composition dependence of the T_d-1T' transition in $Mo_{1-x}W_xTe_2$ was additionally investigated. The T_d* phase observed in $MoTe_2$ appears only on warming from T_d in $Mo_{1-x}W_xTe_2$ in low W-substitution ($x \leqslant 0.21$). Increasing the W fraction to x = 0.34 and beyond leads to phase coexistence of T_d and 1T' across the transition and the vanishing of the T_d* phase. With W-substitution the structural phase transition temperature increases from 260 K in x = 0, to near 500 K by x = 0.54.

The pressure dependence of the T_d-1T' transition was also investigated. In a $Mo_{0.8}W_{0.2}Te_2$ single crystal, the T_d* phase appears only on warming from T_d at pressures lower than 0.88 GPa and disappears by 1.20 GPa. Hydrostatic pressure suppresses the T_d-1T' transition, and only the 1T' phase remains at 1.40 GPa and beyond. The structural transition temperature range remains roughly constant with increased W-substitution but broadens with pressure.

In WTe_2, the monoclinic 1T' phase has not been observed from previous studies. It was assumed that the system enters into the T_d phase on cooling from the melt. However, in this work, a sharp T_d-1T' transition at ambient pressure was observed in a WTe_2 single crystal near 565 K that proceeded without hysteresis. In WTe_2 powder, however, the thermal transition from the T_d to the 1T' phase is much broader, and a two-phase coexistence was observed until 700 K. No T_d* phase is present in WTe_2. The observation of the T_d* phase in $MoTe_2$ and the 1T' phase in WTe_2 at ambient pressure explains the inversion symmetry breaking mechanism from 1T' to T_d in $Mo_{1-x}W_xTe_2$.

Acknowledgements

Over the course of my Ph.D. work, I am privileged to have worked with and learned from many excellent professors and scientists. I am benefited from their knowledge and experience and would like to acknowledge the many people who have contributed to the work in this thesis.

First, I would like to thank my Ph.D. advisor Professor Despina Louca, who has provided me with great support and guidance over the past six years. Professor Louca is the person who introduced me to the experimental condensed matter physics and taught me how to conduct research independently. Professor Louca gave me opportunities to participate in experiments at national laboratories and to attend national conferences. Her priceless guidance and professional attitude are very appreciable in completing this thesis.

I would also like to thank my research committee and thesis committee members, Professor Utpal Chatterjee, Professor Jeffrey Teo, Professor Gia-Wei Chern and Professor Keivan Esfarjani, for the guidance and suggestions they provided during my committee meetings.

I am also very thankful to Dr. John Schneeloch. John joined the group as a postdoc in the summer of 2017 at the same time as me, and he has been a role model for me to learn from since then. John is always open to answer my questions and he taught me with great patience how to prepare samples, perform neutron scattering experiments and analyze data. I will never forget his help and those days traveling together to ORNL and NIST for neutron scattering experiments.

I would also like to thank my past and present group members, Chunruo Duan, Aaron Wegner, Zhenyang Xu, Sharon Philip and Srimal Rathnayaka, for the days we worked together. I have benefited a great deal from our discussions at every group meeting.

During my Ph.D. work, I have been fortunate to work with many knowledgeable and excellent instrument scientists. In particular, I would like to thank Masaaki Matsuda, Adam Aczel, Jaime Fernandez-Baca and Sachith Dissanayake at Oak Ridge National Laboratory, Guangyong Xu at the NIST Center for Neutron Research for their expertise and assistance at the many neutron scattering experiments. I would also like to thank Richard White at Nanoscale Materials Characterization Facility at UVA for his training on the SEM and EDS measurements.

Lastly, I wish to thank family who has supported me throughout my studies at UVA in the past six years. They always had confidence in me even when I did not. I would also thank all my friends here in Charlottesville. Although in a foreign land, the company of my friends always makes me feel happy and warm.

Contents

Chapter 1 Introduction.....013
1.1 2D transition metal dichalcogenides.....014
1.2 Properties of $MoTe_2$ and WTe_2.....016
1.2.1 Topological Weyl semimetal.....016
1.2.2 Extreme magnetoresistance.....018
1.2.3 Superconductivity.....019
1.3 Structures of $MoTe_2$ and WTe_2.....020
1.4 Outline of the thesis.....021
Chapter 2 Background.....024
2.1 Introduction.....024
2.2 Layer stacking for T_d- and 1T'-$MoTe_2$.....025
2.3 Layer displacement parameter δ.....026
2.4 T_d-1T' structural phase transition in $MoTe_2$.....027
2.5 Stacking disorder across the T_d-1T' transition.....030
Chapter 3 Neutron / X-ray scattering.....032
3.1 Introduction.....032
3.2 Neutron scattering.....032
3.2.1 Neutron properties.....033
3.2.2 Neutron sources.....033
3.2.3 Triple-axis neutron spectrometer.....033
3.2.4 Time-of-flight neutron spectrometer.....035
3.3 Diffraction.....036
3.4 Scattering process.....036
3.5 Bragg's law.....038
3.6 Nuclear scattering equations.....039
3.7 X-ray vs. neutron.....042
Chapter 4 Sample preparation and characterization.....043
4.1 Introduction.....043

4.2 Sample preparation.....043
4.2.1 Solid state reaction method.....043
4.2.2 Self-flux growth method.....043
4.3 Sample characterization.....045
4.3.1 X-ray diffraction.....045
4.3.2 Rietveld refinements.....046
4.3.3 Energy-dispersive X-ray spectroscopy.....047
4.3.4 Bulk resistivity.....049
4.4 Summary.....050
Chapter 5 Emergence of T_d* phase in $MoTe_2$.....051
5.1 Introduction.....051
5.2 Measurement plan.....052
5.3 Emergence of T_d*.....054
5.4 'AABB' stacking of T_d*.....058
5.5 T_d* structural refinement.....060
5.6 Centrosymmetric T_d* phase.....063
5.7 Resistivity of $MoTe_2$ revisited.....064
5.8 Discussion.....066
5.9 Summary.....067
Chapter 6 Controllable T_d-1T' transition in $MoTe_2$ through W-substitution.....068
6.1 Introduction.....068
6.2 Neutron scattering on $Mo_{1-x}W_xTe_2$.....069
6.3 Diffuse scattering simulation.....071
6.4 Negative thermal expansion in $Mo_{1-x}W_xTe_2$.....073
6.5 Temperature dependence of β and δ parameters.....075
6.6 Unusual broad transitions in $MoTe_2$.....077
6.7 Structural phase diagram of $Mo_{1-x}W_xTe_2$.....080
6.8 Discussion.....082
6.9 Summary.....082
Chapter 7 T_d-1T' transition in WTe_2.....084

7.1 Introduction.....084
7.2 Neutron scattering on single crystal WTe_2.....085
7.3 X-ray diffraction on powder WTe_2.....087
7.4 Stacking disorder in powder WTe_2.....089
7.5 Temperature dependence of lattice parameters.....091
7.6 Discussion.....092
7.7 Summary.....093
Chapter 8 T_d-1T' transition under pressure.....094
8.1 Introduction.....094
8.2 Neutron scattering on $Mo_{0.8}W_{0.2}Te_2$.....095
8.3 Pressure-temperature phase diagram.....096
8.4 β and δ parameters under pressure.....097
8.5 Discussion.....098
8.6 Summary.....099
Chapter 9 Discussion.....100
9.1 Evolution of T_d* with W-substitution.....100
9.2 Phase diagram from $MoTe_2$ to WTe_2.....101
Chapter 10 Conclusion.....103
Bibliography.....108

List of Figures

Fig. 1.1 Lattice structure and 3D electronic band structure of graphene.....014

Fig. 1.2 Structures of a single-layer TMD in the trigonal (2H), octahedral (1T) distorted octahedral (1T') phases.....015

Fig. 1.3 Comparison between type-I Weyl point and type-II Weyl point.....017

Fig. 1.4 Topological Fermi arcs observed in the T_d phase of $MoTe_2$.....018

Fig. 1.5 Temperature and field dependence of the extreme magnetoresistance in WTe_2.....019

Fig. 1.6 Electrical resistivity of $MoTe_2$ as a function of temperature and pressure, showing clear superconductivity.....020

Fig. 2.1 Crystal structures of the T_d and 1T' phases of $MoTe_2$. For each phase, two equivalent representations are used to showing stacks of layers along the c-axis according to A/B-type of operations.....026

Fig. 2.2 Stacking orders for the T_d and 1T' phases (simplified version) 027

Fig. 2.3 Reported temperature dependence of the electrical resistivity of 1T'-$MoTe_2$.....028

Fig. 2.4 Reported phase diagram of $Mo_{1-x}W_xTe_2$ system as functions of composition x and temperature.....029

Fig. 2.5 Neutron scattering intensity on a $MoTe_2$ single crystal, showing diffuse scattering streaks along L across the T_d-1T' transition.....031

Fig. 3.1 Layout of a triple-axis neutron spectrometer.....034

Fig. 3.2 Layout of a time-of-flight neutron spectrometer.....035

Fig. 3.3 Schematic representation of a neutron scattering event, with the scattering geometry.....038

Fig. 3.4 Bragg diffraction geometry from a simple cubic lattice.....039

Fig. 3.5 Comparison of X-ray and neutron scattering length.....042

Fig. 4.1 Photos of single crystals of $MoTe_2$ and $Mo_{0.94}W_{0.06}Te_2$.....044

Fig. 4.2 XRD data collected on a $MoTe_2$ single crystal at room temperature.....045

Fig. 4.3 Powder XRD on Fe at 300 K with Rietveld refinement performed.....046

Fig. 4.4 Relationship between room-temperature c_{300K}, and W fraction x for $Mo_{1-x}W_xTe_2$.....048

Fig. 4.5 Electrical resistivity of $MoTe_2$ and magnetic field dependence of electrical resistivity of WTe_2.....050

Fig. 5.1 Simulated neutron scattering intensity in the H0L plane for the T_d/1T' phase of $MoTe_2$ (also applies to $Mo_{1-x}W_xTe_2$ and WTe_2) 053

Fig. 5.2 Elastic neutron scattering intensity measured along the (2, 0, L) direction combined at different temperatures through the hysteresis loop on two $MoTe_2$ single crystals, showing the T_d* phase on warming.....055

Fig. 5.3 Integrated Bragg peak intensities as a function of temperature for $MoTe_2$.....056

Fig. 5.4 Diffuse scattering intensity along (2, 0, L) at selected temperatures for $MoTe_2$ when the crystal was warmed up to or cooled down from temperature extremes.....057

Fig. 5.5 Resistivity measured on a $MoTe_2$ crystal between 2 and 300 K showing long hysteresis across transition.....058

Fig. 5.6 The stacking sequences for the T_d, 1T' and T_d* structures.....058

Fig. 5.7 Elastic neutron scattering intensity of $MoTe_2$ taken along (2, 0, L) and (1, 0, L) in the T_d* phase, together with simulated intensity based on 'AABB' stacking proposed for T_d*.....059

Fig. 5.8 Elastic neutron scattering intensities in the 0KL and 2KL planes in the T_d* phase of $MoTe_2$, together with the refined atomic coordinates for the T_d* structure.....061

Fig. 5.9 Schematic representation of the structural transformation from 1T' to T_d* from layer translations along the a-axis that preserve the inversion symmetry center.....063

Fig. 5.10 Integrated neutron scattering intensity near (2, 0, 2.5) for $MoTe_2$ along a narrow and a wide hysteresis loop, compared with resistance data of a $MoTe_2$ crystal measured through the same hysteresis loops.....065

Fig. 6.1 Elastic neutron scattering scans along (2, 0, L) on seven $Mo_{1-x}W_xTe_2$ crystals with different W fractions as a function of temperature.....070

Fig. 6.2 Calculated elastic neutron scattering intensities along (2, 0, L), that simulate the V-shaped diffuse scattering and the phase-coexistence-like transition behavior seen in $Mo_{1-x}W_xTe_2$.....072

Fig. 6.3 Temperature and compositional dependence of the lattice constant and the derivative for $Mo_{1-x}W_xTe_2$.....074

Fig. 6.4 Change of the monoclinic β angle and the interlayer displacement parameter δ of $Mo_{1-x}W_xTe_2$ as a function of W-fraction and temperature.....076

Fig. 6.5 Elastic neutron scattering intensities as a function of temperature measured on two other $MoTe_2$ crystals that show unusual broad transitions.....079

Fig. 6.6 Elastic neutron scattering intensity near (2, 0, 3) for all the $MoTe_2$ and $Mo_{1-x}W_xTe_2$ crystals studied with neutron scattering, together with phase diagrams of $Mo_{1-x}W_xTe_2$ as a function of temperature and W-fraction.....081

Fig. 6.7 comparison of the electrical resistance of $MoTe_2$ and WTe_2.....082

Fig. 7.1 Elastic neutron scattering intensity along (2, 0, L) on a single crystal of WTe_2.....085

Fig. 7.2 Integrated intensity of the T_d and 1T' Bragg peaks as a function of temperature, and the temperature dependence of the interlayer spacing for WTe_2.....086

Fig. 7.3 XRD data taken on a WTe_2 powder sample between 300 and 700 K with Rietveld refinements.....088

Fig. 7.4 The volume fractions of the T_d and 1T' phases as a function of temperature from refinements of the XRD patterns on WTe_2.....089

Fig. 7.5 Simulated XRD intensities for T_d, 1T' and disordered stacking compared with the XRD data taken on powder WTe_2.....090

Fig. 7.6 Temperature dependence of the lattice constants and the δ parameter of WTe_2.....091

Fig. 8.1 Elastic neutron scattering intensity along (2, 0, L) measured on $Mo_{0.8}W_{0.2}Te_2$ under 0.53, 0.88, 1.20 and 1.40 GPa.....095

Fig. 8.2 Pressure-temperature phase diagrams for $Mo_{0.8}W_{0.2}Te_2$.....096

Fig. 8.3 Changes in β and δ plotted against c_{300K} for measurements on $Mo_{1-x}W_xTe_2$ at ambient pressure, and under pressure for $MoTe_2$ and $Mo_{0.8}W_{0.2}Te_2$.....098

Fig. 9.1 Schematic diagrams of the transition pictures for $Mo_{1-x}W_xTe_2$ for three levels of W-substitution.....101

Fig. 9.2 Phase diagram of $Mo_{1-x}W_xTe_2$ as a function of temperature and W-fraction from $MoTe_2$ to WTe_2.....102

List of Tables

Table I Values of room temperature lattice constant c_{300K} and the effective W-fraction for eight $Mo_{1-x}W_xTe_2$ crystals studied with neutron scattering.....049

Table II Refined atomic coordinates for the T_d* phase of $MoTe_2$ using the $P2_1/m$ symmetry.....062

Table III Temperature dependence of the lattice constants of the T_d and 1T' phases of powder WTe_2 between 300 and 700 K.....092

Chapter 1

Introduction

Since the discovery of graphene in 2004 [1], two-dimensional (2D) materials with van der Waals bound layers have attracted considerable attention because of their unique electronic and optical properties. In 2D materials, electrons are free to move in the two-dimensional plane, but are restricted in the third direction, making possible further miniaturization of current electronic devices, such as electronic chips and solid-state storage devices [2, 3]. Research on 2D materials has exploded over the last two decades, where graphene is probably the best known. In 2004, Novoselov and Geim used scotch tapes to produce stable monocrystalline graphitic films and showed that graphene is a good electronic and thermal conductor even at the one-atom thickness [1, 4-6]. Single-layer graphene forms an infinite sheet of hexagons (Fig. 1.1 (a)) and the corresponding electronic band structure is shown in Fig. 1.1 (b). At the crossings of the valance and conduction bands, Dirac nodes are formed. The linear dispersion at the K point gives rise to an anomalous room temperature quantum Hall effect [7]. In 2018, unconventional superconductivity in twisted bilayer graphene was reported, where under a small twist through an angle of 1.1°, superconductivity appears with a critical temperature of 1.7 K [8].

Graphene has important limitations, one of which is the lack of an electronic band gap. This has restricted the applications in the fields of nanoelectronics, nanophotonics, nanoscale sensing and actuation, that require a narrow band gap with semiconducting characteristics. Thus, the search for other 2D materials with semiconducting features has exploded in the last decade or so. A well-known class of materials with properties dominated by their 2D structural units is layered transition metal dichalcogenides that exhibit fascinating properties such as charge density waves and

superconductivity [9, 10]. Layered transition metal dichalcogenides provide a promising alternative to graphene due to the presence of an electronic band gap [11].

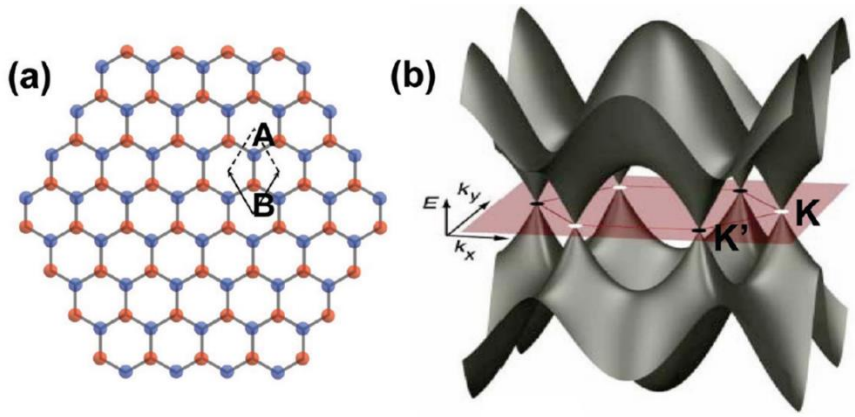

Fig. 1.1 (a) Hexagonal honeycomb lattice of graphene with two atoms (A and B) per unit cell. (b) The 3D electronic band structure of graphene. The figure is from Ref. [12].

1.1 2D transition metal dichalcogenides

2D transition metal dichalcogenides (TMDs) are a class of layered materials with strong in-plane bonding and weak out-of-plane van der Waals interactions, and like graphene, can be exfoliated into single layers with unit cell thickness [13]. Layered TMDs share a very simple chemical formula, MX_2, where the metal atoms M are mainly from group 4 through 7 in the periodic table and the chalcogen atoms X include sulfur (S), selenium (Se) or tellurium (Te) [14].

One advantage of 2D TMDs over graphene is the existence of electronic band gaps in both monolayer and bulk compounds [15, 16]. Thus, many 2D TMDs are semiconducting and can be engineered into ultra-small transistors that are more efficient than state-of-the-art silicon-based transistors [17]. Moreover, the electronic properties of 2D TMDs can be further tuned through changes of their chemical compositions. For example, monolayer dichalcogenides such as MoS_2

(1.8 eV), $MoSe_2$ (1.5 eV), 2H-$MoTe_2$ (1.1 eV), WS_2 (2.1 eV) and WSe_2 (1.7 eV) have a direct band gap of various sizes, whereas their bulk phases exhibit indirect gaps with smaller energies [18].

Layered TMDs usually crystallize in several structural polytypes resulting in different coordinations of the transition metal atoms. The transition metal atoms are surrounded by the chalcogen atoms in either a trigonal or an octahedral local environment [19]. The trigonal environment gives rise to the 2H phase, while the octahedral environment gives rise to the 1T phase [11]. Another common phase is the 1T' that arises because of a distortion of the 1T phase that lowers the overall periodicity [20]. The atomic structures for the 2H, 1T and 1T' phases are shown in Fig. 1.2.

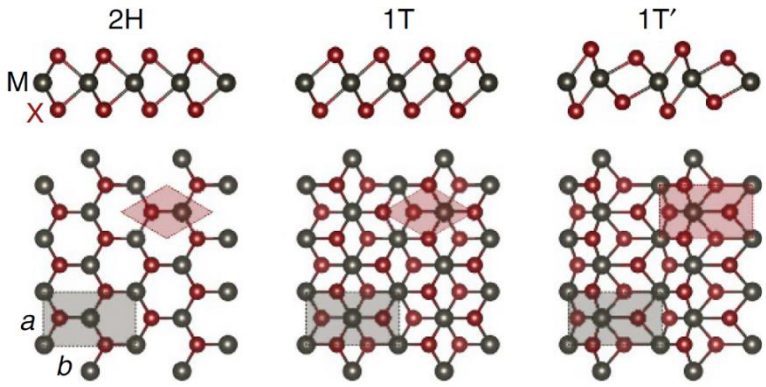

Fig. 1.2 Structures of a single-layer TMD in the trigonal (2H), octahedral (1T) and distorted octahedral (1T') phases. The figure is from Ref. [21].

The structure of layered TMDs can be further defined by the stacking configuration of the individual layers [11]. If single layers of TMDs are stacked directly on top of each other, the T_d

bulk structure is formed. If there is a displacement between adjacent layers along the a-axis, the 1T' bulk structure is formed [11].

1.2 Properties of $MoTe_2$ and WTe_2

A class of widely studied layered TMDs are compounds that contain Mo or W, which have great potential for applications. It was reported that MoS_2 and $MoSe_2$ exhibit indirect-to-direct gap transition when the thickness is reduced to a single monolayer, which opens up opportunities for optoelectronic applications of the materials [22]. MoS_2 nanoparticles are an advanced catalyst for the hydrogen evolution reaction [23]. $MoTe_2$ and WTe_2 are two other well-known representatives. $MoTe_2$ and WTe_2 have received considerable attention recently because of their fascinating electronic properties arising from nontrivial band structure topologies [24-27], the emergence of superconductivity [28] and extreme magnetoresistance [29, 30].

1.2.1 Topological Weyl semimetal

Topological insulators (TI) and topological semimetals (TSM) are new classes of quantum materials characterized by metallic surface states induced by the topology of the bulk band structure. Topological Dirac or Weyl semimetals show linear dispersions in their electronic band structures. At energies near the Fermi level, the valence band and conduction band linearly intersect at a single point called Dirac or Weyl point [31]. There are two types of Weyl semimetals: type-I and type-II. Type-I Weyl semimetals have point-like Fermi surfaces, whereas type-II Weyl semimetals have Weyl points that appear at the contact points between electron and hole pockets [32]. The two types of dispersions are shown in Fig. 1.3.

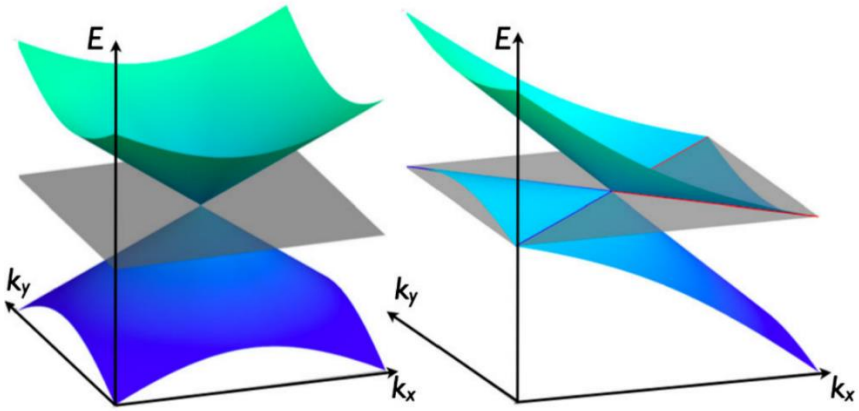

Fig. 1.3 Conventional type-I Weyl point with point like Fermi surface (left) vs. type-II Weyl point, which is the contact point between electron and hole pockets (right). The figure is from Ref. [33].

To realize a Weyl semimetal phase, either the inversion symmetry or time reversal symmetry of the crystal need to be broken [34]. If time reversal symmetry is preserved (usually for non-magnetic materials without applying an external magnetic field), then inversion symmetry must be broken. The Weyl fermions can thus emerge in the electronic band structure if the quasiparticles at the band crossing point are topologically protected against symmetry preserving perturbations. $MoTe_2$ has three crystal structures which are 2H, T_d and 1T', while only the T_d structure has been reported for WTe_2. Both $MoTe_2$ and WTe_2 are known as type-II Weyl semimetals in the T_d phase [25, 27]. In fact, WTe_2 was the first theoretically predicted candidate for type-II Weyl semimetal [32].

A typical characteristic of Weyl semimetals is the existence of surface Fermi arcs. It is because Weyl nodes come in pairs, and bulk Fermi surface (an energy contour crossing the Weyl points) exhibits an unclosed line that starts from one Weyl point and ends at the other with opposite chirality, creating Fermi arcs [31]. Fermi arcs are the surface manifestation of the topological nature of Weyl semimetals, which can be experimentally observed using surface probing

techniques such as angle-resolved photoemission spectroscopy (ARPES). Shown in Fig. 1.4 (e-h) are ARPES intensity maps measured on $MoTe_2$ at energies from the Fermi level, E_F, to -0.06 eV. The red arrows point to the topological surface states where Fermi arcs can be clearly seen [25]. Through ARPES measurements, the Weyl semimetal nature is evident in bulk $MoTe_2$ [25], WTe_2 [35] and recently in $Mo_{0.45}W_{0.55}Te_2$ [36] from the observation of topological Fermi arcs.

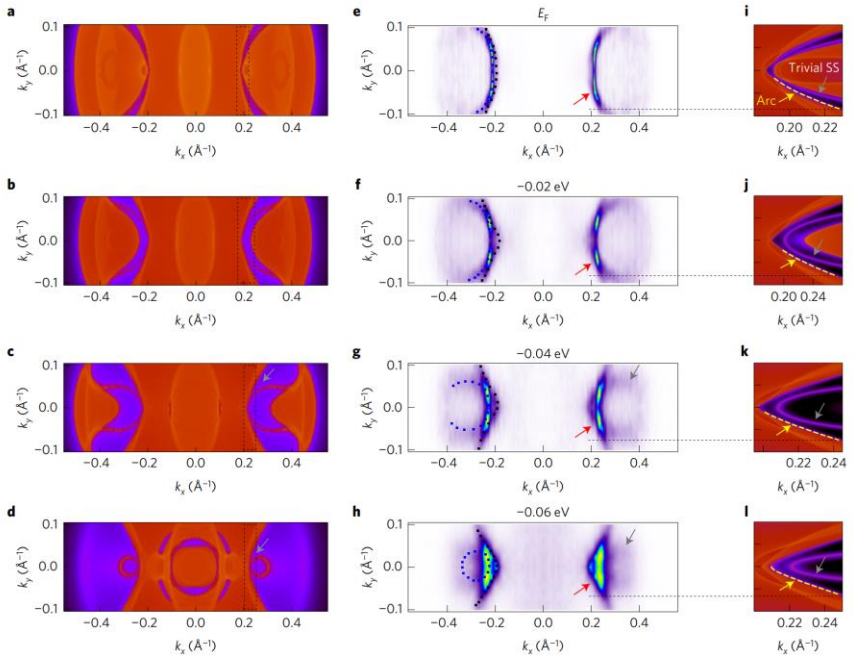

Fig. 1.4 Observation of topological Fermi arcs in the T_d phase of $MoTe_2$ (data in panels e-h) The figure is from Ref. [25].

1.2.2 Extreme magnetoresistance

In addition to the nontrivial topological band structures, $MoTe_2$ and WTe_2 have other fascinating properties. For example, in WTe_2, a non-saturating XMR was observed, which is very uncommon for nonmagnetic materials. Shown in Fig. 1.5 is the electrical resistivity as a function of temperature for WTe_2 under different magnetic fields that shows that the XMR effect in WTe_2 can

be turned on at low temperatures with an external magnetic field. The XMR in WTe_2 reaches 2,500,000% at 45 T and 4.5 K and does not saturate [29]. Such XMR in WTe_2 has been explained by the nearly perfect balanced electron-hole populations in the T_d-phase [37]. Therefore, WTe_2 has the potential for low-temperature applications in 2D magnetic sensors or computing-related devices. $MoTe_2$ also has a very large magnetoresistance (MR), reaching up to 32,000% at 9 T [38].

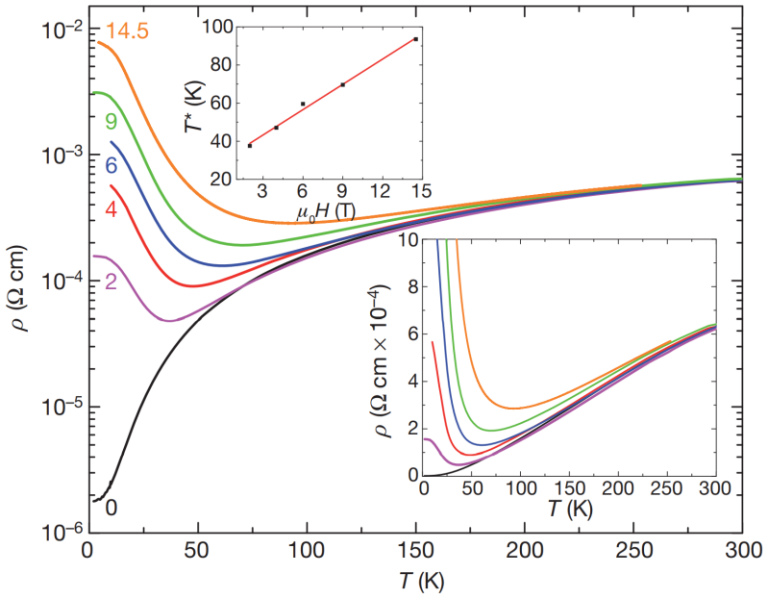

Fig. 1.5 Temperature and magnetic field dependence of the XMR in WTe_2, when the current is applied along the b-axis (W-chain direction) and magnetic field is parallel to c-axis (perpendicular to the layers). The figure is from Ref. [29].

1.2.3 Superconductivity

Another interesting property for $MoTe_2$ is superconductivity. At ambient pressure, bulk $MoTe_2$ exhibits superconductivity with a critical temperature T_c of 0.1 K. By applying pressure, the critical temperature can be increased [28]. Shown in Fig. 1.6 is the electrical resistivity of $MoTe_2$ as a function of temperature under pressure from 0.7 to 11.7 GPa in (a), and from 11.7 to 34.9 GPa in

(b). Drops in electrical resistivity and zero-resistance behavior are apparent. T_c first increases with increasing pressure and reaches a maximum superconducting transition temperature corresponding to T_c = 8.2 K at 11.7 GPa. By further increasing the pressure, however, the zero-resistance-point T_c is gradually suppressed [28].

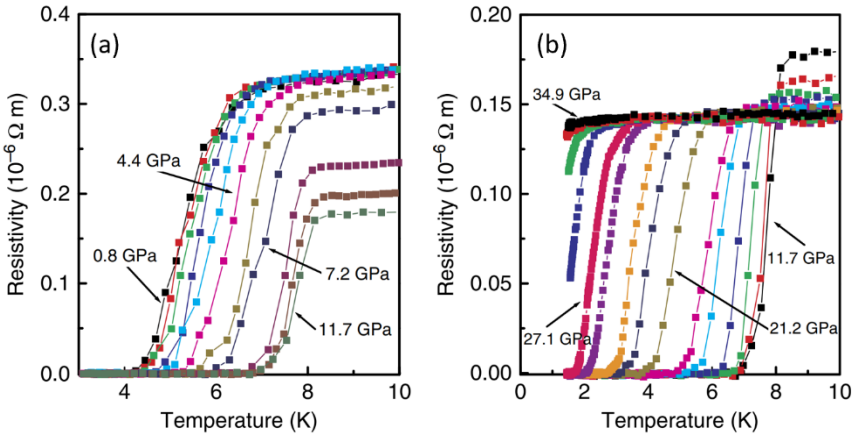

Fig. 1.6 Electrical resistivity of $MoTe_2$ as a function of temperature and pressure, showing clear superconductivity. The figure is from Ref. [28].

1.3 Structures of $MoTe_2$ and WTe_2

$MoTe_2$ crystallizes in three crystal structures, which are T_d, 1T' and 2H [39]. In the bulk form, while the T_d and 1T' phases are semimetals, the 2H phase of $MoTe_2$ is a semiconductor with an indirect band gap of ~0.85 eV [40]. In the few-layered form, the 1T' phase exhibits a band gap opening of up to 60 meV [41], and the 2H phase shows a direct band gap, the size of which is inversely proportional to the number of layers [42]. In bulk $MoTe_2$, there is a structural phase transition at ~260 K from the high-temperature 1T' phase to the low-temperature T_d phase [43]. In bulk WTe_2, only the T_d phase has been reported under ambient pressure [44, 45]. The T_d phase of

WTe_2, however, can be converted into 1T' by applying an external pressure from 4.0 to 18.2 GPa [46, 47].

1.4 Outline of the thesis

The research described in the thesis mainly consists of neutron scattering and X-ray diffraction measurements exploring the structural phase transitions in the Weyl semimetal $Mo_{1-x}W_xTe_2$. The objective was to provide an experimental basis for the understanding of inversion symmetry breaking mechanism across the 1T'-T_d transition in this material, which is a prerequisite for the emergence of Weyl fermions. The composition and pressure dependence of the structure phase diagram of $Mo_{1-x}W_xTe_2$ was also investigated, as both factors are known to influence the sliding layer transitions, thus the electronic band structures of $Mo_{1-x}W_xTe_2$.

The following chapters of the thesis are organized as follows. Chapter 2 will focus on the discussion of the structures of $Mo_{1-x}W_xTe_2$. The T_d and 1T' phases of bulk $MoTe_2$ will be discussed and compared in detail, and two structural parameters will be defined. The T_d-1T' structural phase transition in bulk $MoTe_2$ and the associated stacking disorder will also be discussed, with questions raised that require further investigation.

Chapter 3 will provide an overview of the experimental techniques in detail. An overview of the theoretical background of scattering will be provided. Current neutron sources in the US and two types of neutron scattering spectrometers, triple-axis neutron spectrometer and time-of-flight neutron spectrometer will also be introduced. In chapter 4, the experimental methods used for sample preparation will be discussed, that include solid-state reaction method used to prepare powders of $Mo_{1-x}W_xTe_2$, and self-flux growth method used in the preparation of single crystals of $Mo_{1-x}W_xTe_2$. Sample characterization, data collection and analysis methods are also described.

Experimental work on the T_d-1T' transition in $Mo_{1-x}W_xTe_2$ will be presented in chapters 5 through 8. Chapter 5 focuses on the T_d-1T' transition in $MoTe_2$. Results from elastic neutron scattering measurements on two $MoTe_2$ single crystals will be discussed. Direct evidence of the presence of a novel structure, T_d*, across the T_d-1T' phase boundary will be provided. Discussion on the stacking sequence and the crystal structure of this centrosymmetric, pseudo-orthorhombic T_d* phase will be included as well. In addition, the stacking disorders associated with the structural changes between T_d, T_d* and 1T' will be described.

In chapter 6, the compositional dependence of the T_d-1T' transition in $Mo_{1-x}W_xTe_2$ will be investigated. Single crystals of $MoTe_2$ were chemically doped with various levels of W, and the evolution of the T_d-1T' transition as a function of W-fraction, not only in terms of the overall transition temperature, but also the transition behavior that involves changes in the T_d* phase and diffuse scattering, will be discussed based on results from elastic neutron scattering measurements. A phase diagram of $Mo_{1-x}W_xTe_2$ as a function of temperature and W-substitution will be presented, and discussions on the change in the lattice constants and the layer sliding parameter δ are also provided.

In chapter 7, the crystal structure of WTe_2 at ambient pressure at various temperatures will be explored, and evidence will be presented for a T_d-1T' transition. Evidence of the transition from both single crystal neutron scattering and powder XRD measurements will be described. A comparison of the transition behavior between WTe_2 and $MoTe_2$ will be provided.

In chapter 8, the effects of hydrostatic pressure on the T_d-1T' transition in $Mo_{0.8}W_{0.2}Te_2$ will be studied. The suppression of the T_d phase with increasing pressure will be discussed. A pressure-temperature phase diagram for $Mo_{0.8}W_{0.2}Te_2$ that follows the T_d* phase will be established.

In chapter 9, a qualitative model that describe the T_d-1T' transition in $Mo_{1-x}W_xTe_2$ as a function of W-substitution will be provided, together with a phase diagram for the $Mo_{1-x}W_xTe_2$ system. Conclusions on the T_d-1T' transition in $Mo_{1-x}W_xTe_2$ will be presented in chapter 10. Connections are made between the experimental work in the thesis and current theories on $MoTe_2$ and WTe_2. Some possible future directions for further studies on the structural properties of $Mo_{1-x}W_xTe_2$ will be given.

Chapter 2

Background

2.1 Introduction

Bulk $MoTe_2$ consists of layers of Mo octahedrally (T_d and 1T' phases) or trigonally (2H phase) coordinated with Te stacked along the c-axis, where the layers are held together by weak van der Waals forces. The stable phase for bulk $MoTe_2$ at room temperature is 2H. But if the melt is quenched, then the 1T' phase is reached. $MoTe_2$ undergoes a structural phase transition at around 260 K from the monoclinic 1T' phase to the orthorhombic T_d phase on cooling. The transition from 1T' to T_d breaks inversion symmetry and allows the Weyl quasiparticles to emerge. The T_d phase of $MoTe_2$ is reported to be type-II Weyl semimetals [25].

WTe_2 is isostructural to $MoTe_2$, with Mo atoms replaced by W. In contrast to $MoTe_2$, only the T_d phase has been reported for bulk WTe_2 under ambient pressure [44, 45]. WTe_2 hosts Weyl fermions in the electronic band structure and exhibits XMR [29, 35]. In WTe_2, there are zigzag W-chains running along the b-axis, and the XMR can reach to 2,500,000% at 45 T and 4.5 K but is only achieved when the current is applied along the b-axis and magnetic field is parallel to c-axis [29]. The anisotropic behavior of XMR in WTe_2 has been explained by the nearly perfect balanced electron-hole populations along the b-axis in the T_d-phase, suggesting the XMR in WTe_2 is closely related to the crystal structure.

The difference between the T_d and 1T' structures of $MoTe_2$ can be described by a shift of layers along the a-axis in the 1T' phase relative to T_d. Therefore, the T_d-1T' transition in $MoTe_2$ is a type of sliding layer transitions, in which the layers shift from one stacking to another as a function of temperature. During the T_d-1T' transition there is substantial stacking disorder. Overall, though,

the nature of the transition itself has not been closely studied, despite the apparent simplicity of the change in structure and the opportunity to investigate the role of disorder in the transition.

In this chapter, the T_d and 1T' structures of bulk $MoTe_2$ will be discussed in detail. Two parameters are defined to describe the stacking sequences along the c-axis for T_d and 1T': an A/B-type of stacking operation that describes how the neighboring layers are relatively positioned, and a δ parameter that characterizes the magnitude of layer displacements along the a-axis. Earlier neutron diffraction measurements on a single crystal of $MoTe_2$ will also be presented, that show diffuse scattering upon cooling across the T_d-1T' phase boundary, suggesting the necessity of further investigation.

2.2 Layer stacking for T_d- and 1T'-$MoTe_2$

The orthorhombic T_d phase of $MoTe_2$ is non-centrosymmetric with a space group of $Pnm2_1$, whereas the monoclinic 1T' phase of $MoTe_2$ is centrosymmetric with a space group of $P2_1/m$ [24, 25]. The T_d and 1T' phases have similar structures; they both consist of a two-layer unit cell and differ mainly by an in-plane displacement along the a-axis. Both T_d and 1T' phases have nearly identical, centrosymmetric layers stacked along the c-axis according to an A- or B-type of operations, as shown in Fig. 2.1. The A operation basically maps one layer of T_d to the layer below it, so T_d can be built from repeating "AA" sequences. The B operation is the same as for A but followed by a translation of the layer along the a-direction, the magnitude of which is defined as ϵ as shown in Fig. 2.1. For $MoTe_2$, $\epsilon = \pm 0.15$ lattice units. The 1T' phase of $MoTe_2$ has a stacking sequence of "ABAB...". Equivalently, these two types of stacking orders can also be represented by centering the small squares in Fig. 2.1 at the inversion symmetry center of each layer, denoted

by the black dots. For the 1T' phase, the inversion symmetry center of the second layer is also the inversion symmetry point of the monoclinic unit cell. For $MoTe_2$, the T_d-1T' structural phase transition is first-order in nature [43].

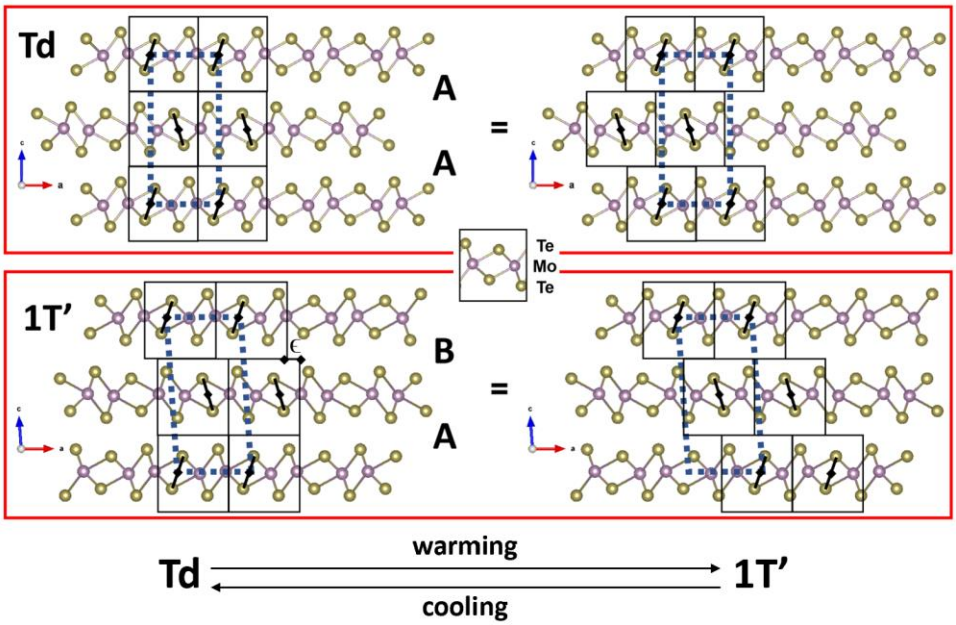

Fig. 2.1 Crystal structures of the T_d and 1T' phases of $MoTe_2$ in the a-c plane, showing stacks of layers along the c-axis. For each phase, two equivalent representations are used to demonstrate the A/B-type of stacking sequences. The solid black squares represent cells that make up a single $MoTe_2$ layer, the dashed blue boxes denote the unit cell for T_d/1T', ϵ represents the magnitude of interlayer shift for B-type of stacking in fractional unit, and the black dots show the inversion symmetry centers of each layer.

2.3 Layer displacement parameter δ

Shown in Fig. 2.2 is a schematic representation of the stacking sequence 'AAAA' for the T_d and 'ABAB' for the 1T' phases. By using the squares centered at the inversion symmetry center of each layer, the amount of displacement along a-axis between all pairs of neighboring layers,

regardless of A-or B-type stacking, is essentially the same, because the A and B stacking operations are ideally symmetry-equivalent. A becomes B on inversion, as shown on the right of the figure. Therefore, an in-plane displacement parameter δ, which is defined as the distance along the a-axis between the inversion symmetry centers of neighboring layers, can be used to characterize the layer displacement. Therefore, the structures of $MoTe_2$ are specified by two parameters: the A/B stacking sequence and δ. For the monoclinic 1T' phase, the 'ABAB' stacking is tilted with an angle β, as shown in Fig. 2.2.

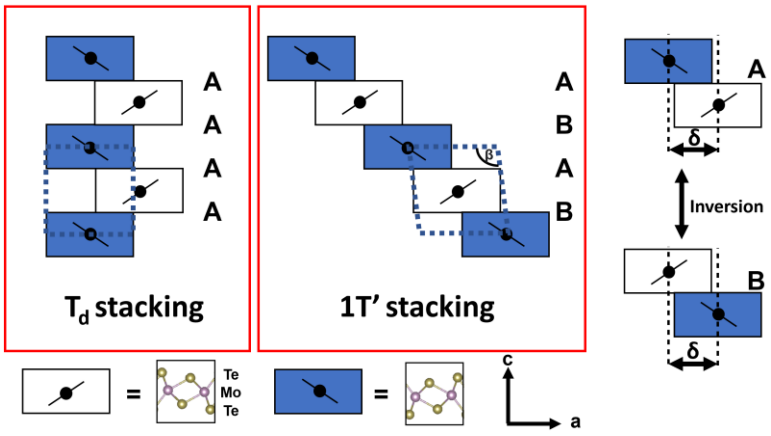

Fig. 2.2 Stacking orders for the T_d and 1T' phases using the inversion-symmetry-point-centered cells. Dashed-line boxes denote unit cell. It is shown that A- and B-type of layer stacking are symmetry equivalent.

2.4 T_d-1T' structural phase transition in $MoTe_2$

When $MoTe_2$ is cooled below ~260 K, the layers slide from the stacking arrangement of the monoclinic 1T' phase toward that of the orthorhombic T_d phase [24, 25, 43]. The T_d-1T' transition in $MoTe_2$ has been studied from transport measurements. Shown in Fig. 2.3 is the electrical

resistivity of 1T'-$MoTe_2$ as a function of temperature. Upon cooling from room temperature, an anomaly in resistivity is observed at around 250 K, indicating the onset to T_d [48].

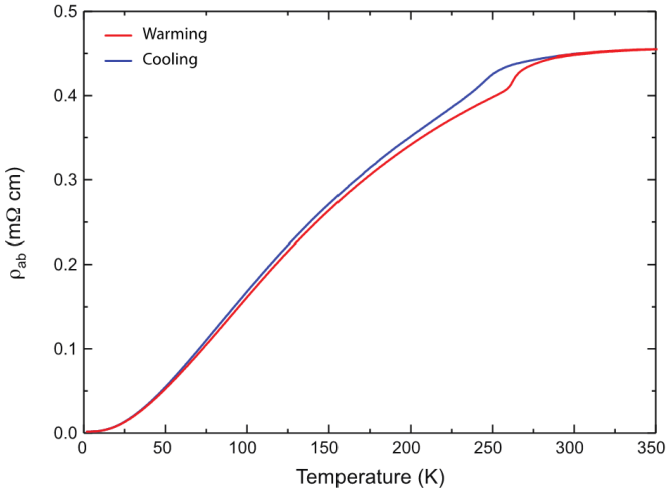

Fig. 2.3 Temperature dependence of the electrical resistivity of 1T'-$MoTe_2$. The figure is from Ref. [48].

Such sliding layer transition is often seen in 2D materials, and it can be thought of as a distinct kind of structural phase transition mechanism, in which the layers shift from one stacking to another as a function of temperature or other external parameters, such as pressure, electric field, or thickness of the sample [49]. For instance, the T_d-1T' transition in $MoTe_2$ can be tuned by strain, electric field and chemical substitution. It is reported that pressure decreases the T_d-1T' transition temperature in bulk $MoTe_2$ [50]. By applying an external electric field or strain, the stable 2H-phase can transform into the metastable 1T' phase in monolayer or thin films of $MoTe_2$ at room temperature [51, 52]. With Se substitution, a structural phase transition from T_d to 1T' to 2H can be realized in $MoTe_{2-x}Se_x$ thin films [53].

W-substitution is another tuning parameter for $MoTe_2$. Given W has a larger atomic size compared to Mo, doping $MoTe_2$ with W in the form of $Mo_{1-x}W_xTe_2$ is equivalent to applying a negative chemical pressure to the lattice, which increases the atomic distances. Varying x in $Mo_{1-x}W_xTe_2$ can shift the compound's Fermi level, thus having a great effect on physical and structural properties. W-substitution also affects the T_d-1T' sliding layer transition in $MoTe_2$. It is reported that increasing the W fraction in $Mo_{1-x}W_xTe_2$ increases the T_d-1T' transition temperature [54]. A phase diagram of the $Mo_{1-x}W_xTe_2$ system as functions of temperature and W-fraction was established, as shown in Fig. 2.4 [39].

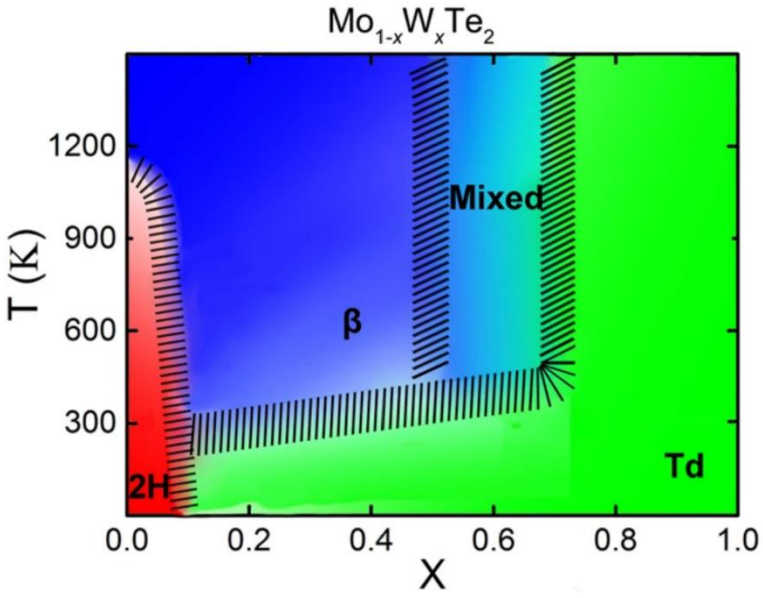

Fig. 2.4 Phase diagram of $Mo_{1-x}W_xTe_2$ system as functions of composition x and temperature. The β phase in the figure is the 1T' phase. The figure is from Ref. [39].

However, the phase diagram of $Mo_{1-x}W_xTe_2$ in Fig. 2.4 is not complete, as the W-substitution dependence of the structures of $Mo_{1-x}W_xTe_2$ has only been investigated up to x = 0.5. For the region that is labeled 'mixed', the structures have not been measured directly. At the range from

x = 0.5 to 0.7, the phase of $Mo_{1-x}W_xTe_2$ is described as a mixing phase of 1T' and T_d, given 1T' exists from x = 0.1 to 0.5 at room temperature, and T_d lies in a composition x ranging from 0.7 to 1, without temperature-dependent phase transitions being reported [39]. The increase in the T_d-1T' transition temperature with W-substitution suggests the possibility of an ambient-pressure transition at high temperatures in WTe_2 that require further investigation.

Some other materials with reversible temperature-induced sliding layer transitions include CrX_3 (X=Cl, Br, I) [55] and α-$RuCl_3$ [56], of interest for their magnetic properties; Bi_4I_4 [57], of interest as a weak topological insulator in the β phase. In fact, many layered materials have structure-property relationships that depend on their layer stacking. For example, a twist in bilayer graphene can result in superconductivity [8]. $MoTe_2$ can be a prototype for understanding how stacking variations in layered materials can lead to exotic states of matter and have an effect on the topological properties.

2.5 Stacking disorder across the T_d-1T' transition

Though the T_d-1T' structural phase transition in $MoTe_2$ mainly involves layer shifts along the a-axis, the transition behavior is more complex than usually thought as stacking disorders are known to occur. Previous neutron diffraction measurements on $MoTe_2$ showed the presence of substantial diffuse scattering upon cooling across the phase boundary [58]. Shown in Fig. 2.5 is the neutron scattering intensity in the H0L and 0KL planes measured on a $MoTe_2$ single crystal across T_d-1T' phase boundary. The diffuse scattering is only observed in the H0L plane but not 0KL plane, which indicates a disordered stacking pattern along the c-axis in the ac-plane [58]. A better understanding of the stacking disorder in the phase transition is needed.

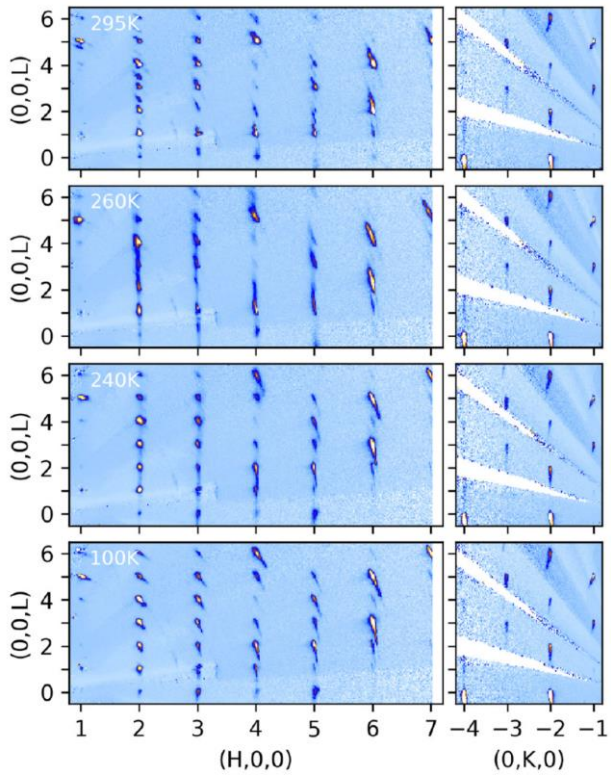

Fig. 2.5 Neutron scattering intensity measured on a $MoTe_2$ single crystal in the H0L and 0KL planes. Diffuse scattering streaks appear along L in the H0L plane only, upon cooling from 295 to 240 K. The figure is from Ref. [58].

Chapter 3

Neutron / X-ray scattering

3.1 Introduction

Neutrons and X-rays are widely used in scattering experiments to investigate microscopic details of the static structures and dynamics. Neutron or X-ray scattering involves creating a beam of neutrons or X-ray photons, passing that beam through a sample, and detecting where and when neutrons or X-ray photons scattered from the sample hit a detector. From the changes in energy (E) and momentum (Q) of neutrons or X-ray photons, the crystal structure of the material can be determined. The principles underlying the scattering process are the same regardless of the particle (neutron or X-ray) used to probe the periodic structure of materials. In this chapter, an introduction on both neutron scattering and XRD techniques will be provided. Neutron sources and two types of neutron spectrometers, which are triple-axis spectrometer and time-of-flight spectrometer, will be discussed.

3.2 Neutron scattering

The neutron was first discovered by James Chadwick in 1932 [59]. Neutron scattering technique has been developed into a powerful probe that is now widely used in condensed matter physics to study both the static crystal structures and the dynamic properties, such as phonon and spin wave, of different materials [60]. The 1994 Nobel Prize in Physics was awarded for pioneering contributions to the development of neutron scattering techniques for studies of condensed matter jointly with one half to Bertram N. Brockhouse for the development of neutron spectroscopy and with one half to Clifford G. Shull for the development of the neutron diffraction technique [61].

3.2.1 Neutron properties

The basic properties of neutron make it an ideal probe with which to study condensed matter [62]. First, neutrons carry zero charge. They can bypass the Coulomb barrier of the electron cloud, penetrate deeply into the sample and scatter off the nuclei. Second, the de Broglie wavelength of thermal neutrons (5-100 meV) are comparable to the interatomic distance (on the order of 10^{-10} m) of solids. The interference effect allows thermal neutrons to detect the microscopic structure of the scattering system. Third, neutrons have magnetic moments (1.913 nuclear magnetons, μ_N), and they also interact with the unpaired electrons of the magnetic atoms, yielding information on the magnetic structure. In addition, the energy of thermal neutron is of the same order as that of many excitations in solids. Using inelastic neutron scattering (where neutrons gain or lose energy during the scattering process), the excitation energy can be precisely determined [63, 64].

3.2.2 Neutron sources

There are two methods to produce the neutron beams used in a scattering experiment, either through nuclear fission in a reactor (a continuous source) or through spallation when accelerated protons strike a heavy metal target (a pulsed source). The High Flux Isotope Reactor (HFIR) at the Oak Ridge National Laboratory (ORNL) [65] and the research reactor at NIST Center for Neutron Research (NCNR) [66] are both reactor-based neutron sources, while the Spallation Neutron Source (SNS) at ORNL is based on spallation [67].

3.2.3 Triple-axis neutron spectrometer

At a neutron facility, specialized instruments with different Q and E coverages are built to carry out a wide variety of experiments. The two most commonly used neutron scattering spectrometers are triple-axis spectrometer [68] and time-of-flight spectrometer [69], which differ by how energy

transfer is measured. Data shown in the thesis was mostly collected on triple-axis neutron spectrometers, that include HB1, CG4C, HB1A at HFIR, and SPINS at NIST center for neutron research. Elastic neutron scattering measurements were also performed on time-of-flight spectrometers, such as CORELLI and NOMAD at the SNS.

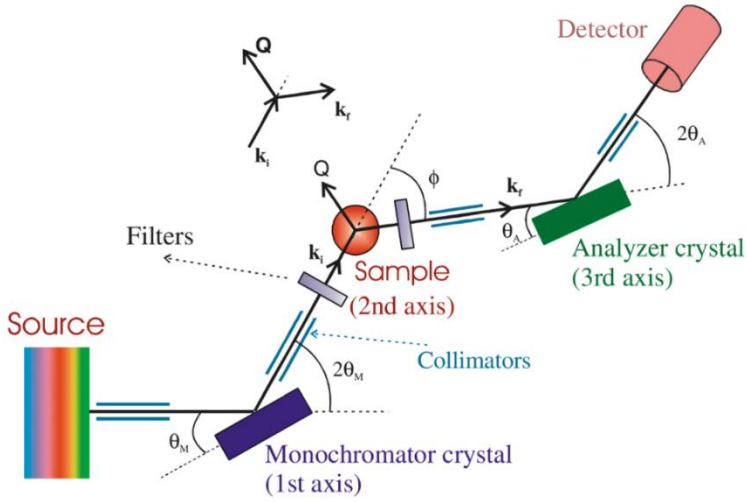

Fig. 3.1 A schematic layout of a triple-axis neutron spectrometer. The figure is from Ref. [70].

A schematic layout of a triple-axis neutron spectrometer is shown in Fig. 3.1. White neutron beams generated from the reactor first pass through a single crystal monochromator that selects neutrons with a specific wavelength (energy). The beam is then directed onto the sample. The neutrons scattered off the sample are Bragg reflected from the single crystal analyzer to determine the final energy. The analyzer also uses Bragg scattering to select outgoing neutron energies. Lastly, neutrons reflected by the analyzer are detected by the neutron detector [70]. For measurements on triple-axis neutron spectrometers, the scattered intensity is obtained for one location in the space of momentum and energy transfer at a time. Triple-axis neutron spectrometer allows for the variations of three dimensions by being able to rotate a sample (typically a single crystal), the

monochromator, and the detector independently, which enables the study of intermediate-energy excitations, phase transitions and structures of the material [68].

3.2.4 Time-of-flight neutron spectrometer

For neutron scattering experiments performed on a time-of-flight spectrometer, pulsed neutron beams are used. At the pulsed sources, neutrons are produced in bursts of roughly 10^{14} particles, with an initial pulse width on the order of 1 μs at a frequency of 10-50 Hz [68]. Time-of-flight spectrometers provide neutron pulses with a distribution of wavelengths and choppers are often used to selects neutrons with a specific energy. For measurements on time-of-flight spectrometers, the time between the pulse hitting the sample and each neutron arriving at a detector is recorded. Time-of-fight spectrometers usually have an array of detectors so that many energy and momentum transfers can be measured with each pulse, resulting in data sets that cover a region in reciprocal space. The layout of a time-of-fight neutron spectrometer is shown in Fig. 3.2.

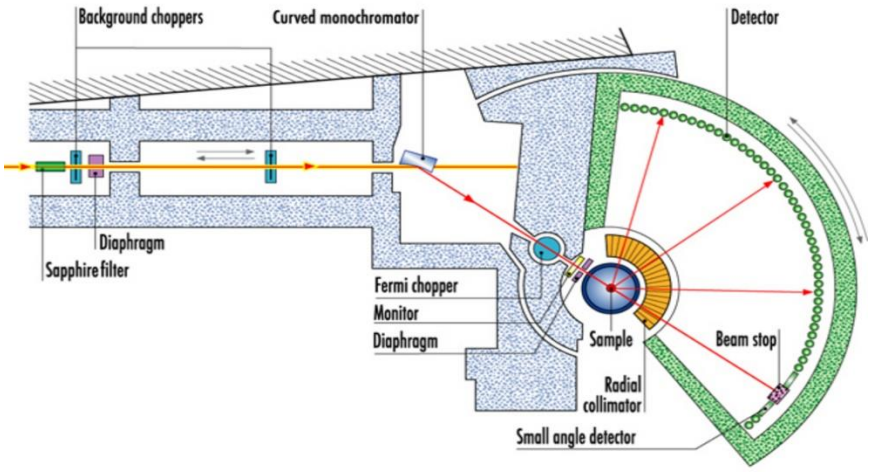

Fig. 3.2 A schematic layout of a time-of-flight neutron spectrometer. The figure is from Ref. [71].

3.3 Diffraction

Diffraction is based on wide-angle elastic scattering and has been widely used to characterize the crystal structures of single crystal and polycrystalline materials. In a diffraction measurement, the incident neutrons or X-ray photons interact with the sample and the intensities of the diffracted beam are measured by the detector as a function of the scattering angle 2θ [72]. Constructive interference of the diffracted particles or waves occurs only in specific directions governed by Bragg's law. Depending on the crystal structure, the diffraction patterns are uniquely obtained that are used to obtain useful information on the lattice parameters, crystallite size, strain and atomic coordinates of solid materials.

3.4 Scattering process

When a beam of neutrons or X-ray photons interacts with the sample in a scattering process, the total energy and the total momentum are conserved. The momentum transferred from the beam to the sample is defined as:

$$\vec{Q} = \vec{k} - \vec{k'} \tag{3.1}$$

where $\vec{k}$ and $\vec{k'}$ are the wavevectors of the incident and scattered beams. The angle between $\vec{k}$ and $\vec{k'}$ is 2θ. The scattering geometry is shown in the inset of Fig. 3.3. The energy gained or lost by the beam can be expressed as:

$$dE = E - E' = \hbar\omega = \frac{\hbar^2}{2m}(|\vec{k}|^2 - |\vec{k'}|^2) \tag{3.2}$$

In Eq. 3.2, $\hbar$ is the reduced Planck constant, ω is the angular frequency, and m is the mass of the neutron or X-ray photon. By comparing the kinetic energy and momentum of the incident beam vs. the scattered beam, the orientation of the lattice, the energy gained or lost by the sample, thus

the structural and vibrational information can be obtained. Neutron scattering experiments are usually categorized in two types, based on whether the kinetic energy of the neutron is unchanged before and afterwards. They are elastic and inelastic neutron scattering. Elastic neutron scattering is usually used to determine the crystal structure, while inelastic neutron scatting is often used to measure the excitations. In addition, neutron scattering measurements can also be classified into nuclear or magnetic neutron scattering, depending on whether the neutrons interact with the unpaired spins of the magnetic atoms in the sample. Magnetic neutron scattering is usually performed to probe the magnetic properties of the material such as the spin structure and magnon [62].

In a neutron scattering experiment, the double differential cross section $d^2\sigma/\mathrm{d}\Omega\mathrm{d}\omega$ is measured, that is, the number of neutrons scattered per second into a solid angle $\mathrm{d}\Omega$, with an energy between $\hbar\omega$ and $\hbar(\omega + \mathrm{d}\omega)$, normalized by the incident neutron flux. The double differential cross section is usually referred to as "intensity". Shown in Fig. 3.3 is a schematic representation of a scattering event. Incoming neutrons with initial wavevector $\vec{k}$ interacts with an atomic nucleus and is scattered at an angle 2θ, with final wavevector $\vec{k'}$.

The double differential cross section consists of a coherent part and an incoherent part. The coherent scattering depends on the correlation between the positions of the same nucleus at different times, and on the correlation between the positions of different nuclei at different times. It gives interference effects. The incoherent scattering depends only on the correlation between the positions of the same nucleus at different times [62]. The coherent elastic nuclear neutron scattering is essential for the determination of the crystal structures and characterization of the phase transitions.

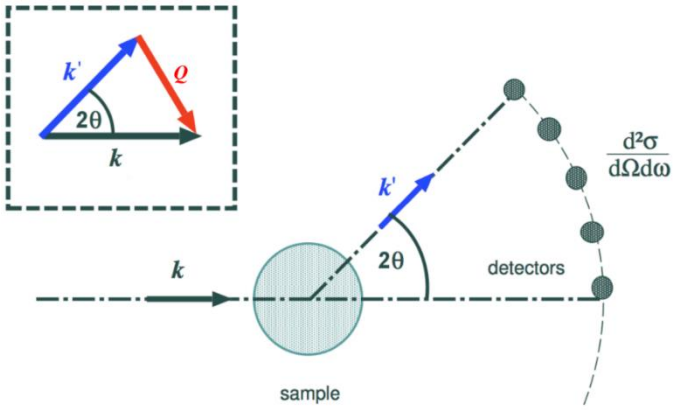

Fig. 3.3 Schematic representation of a neutron scattering experiment. Inset: Scattering geometry. The figure is from Ref. [73].

3.5 Bragg's law

Diffraction from a crystal result in sharp spots of intensity in the reciprocal (momentum) space. These sharp spots are known as Bragg peaks, which occur because of the periodic structure of the crystal [74]. For coherent scattering, it only occurs when the momentum transfer vector $\vec{Q}$ is equal to the reciprocal lattice vector $\vec{G}$. The positions of the Bragg peaks in reciprocal space are closely related to the real space crystal structure. If the crystal unit cell vectors in real space are given by $\vec{a}$, $\vec{b}$ and $\vec{c}$, and the basis vectors in momentum space are $\overrightarrow{a^*}$, $\overrightarrow{b^*}$ and $\overrightarrow{c^*}$, the vector $\vec{G}$ is then integer combinations of these three basis vectors, given by the formula $\vec{G} = H \cdot \overrightarrow{a^*} + K \cdot \overrightarrow{b^*} + L \cdot \overrightarrow{c^*}$, where H, K, L make up the reciprocal lattice index, also called Miller index. $\vec{G}$ is perpendicular to a set of crystal planes in real space, the magnitude of which is given by:

$$|\vec{G}| = n\frac{2\pi}{d} \tag{3.3}$$

where d is the interplane spacing and n is an arbitrary integer.

Bragg's law can then be derived from the scattering geometry shown in Fig. 3.3. For elastic scattering, $|\vec{k}| = |\vec{k'}|$, where $|\vec{k}| = 2\pi/\lambda$. Here λ is the wavelength and it gives:

$$|\vec{Q}| = 2|\vec{k}| \cdot \sin\theta \tag{3.4}$$

Combined with Eq. 3.3, it gives:

$$n\lambda = 2d \cdot sin\theta \tag{3.5}$$

This is the familiar form of Bragg's law. Eq. 3.5 shows the condition for constructive interference, which is illustrated in Fig. 3.4, using the example of Bragg diffraction from a simple cubic lattice.

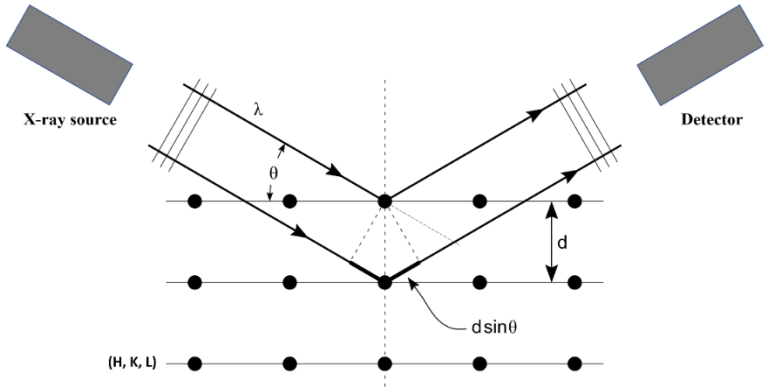

Fig. 3.4 Schematic plot of Bragg diffraction from a simple cubic lattice. The figure is from Ref. [75].

3.6 Nuclear scattering equations

The relations of the double differential cross section for nuclear scattering can be derived from Fermi's golden rule that involves an initial state λ and a final state λ' of the scattering system. The double differential cross section is given as follows [62]:

$$\left(\frac{d^2\sigma}{d\Omega dE'}\right)_{\lambda\to\lambda'} = \frac{k'}{k}\left(\frac{m}{2\pi\hbar^2}\right)^2 | < k'\lambda'|V|k\lambda > |^2\delta(E_\lambda - E_{\lambda'} + E - E') \tag{3.6}$$

In Eq. 3.6, the matrix $| < k'\lambda'|V|k\lambda > |^2$ is proportional to the number of transitions per second from the state λ to the state λ', V is a potential that the neutron interacts with, and the δ function represents the energy distribution of the scattered neutrons.

Since V is short ranged in nuclear scattering, it can be represented as a δ function. The V potential from the j-th nucleus at R_j is:

$$V_j(x_j) = \frac{2\pi\hbar^2}{m} b_j \delta(x_j) \tag{3.7}$$

where b_j is the scattering length. For a positive scattering length, it implies a repulsive potential. Here $x_j = r - R_j$ where r is the neutron coordinate.

During neutron scattering, there is a weak perturbation of the material being probed. Therefore, both incident and scattered neutrons can be assumed as plane waves based on the Born approximation, and the double differential cross section for nuclear scattering can be simplified as:

$$\frac{d^2\sigma}{d\Omega dE'} = \frac{k'}{k}\frac{1}{2\pi\hbar}\sum_{jj'} b_j b_{j'} \int_{-\infty}^{\infty} < \exp\{-i\vec{Q}\cdot\overrightarrow{R_{j'}}(0)\}\exp\{i\vec{Q}\cdot\overrightarrow{R_j}(t)\} > \times \exp(-i\omega t)dt \tag{3.8}$$

A scattering system usually contains a large number of nuclei. If they are all identical, the scattering lengths would be same. However, incoherence is often present in the system. Incoherent comes from random occupations of the nuclei with different scattering lengths in a lattice, which might be due to different elements, or multiple spin states or isotopes of a single element. The double differential cross section can then be further divided into coherent and incoherent parts:

$$\left(\frac{d^2\sigma}{d\Omega dE'}\right)_{coh} = \frac{\sigma_{coh}}{4\pi}\frac{k'}{k}\frac{1}{2\pi\hbar}\sum_{jj'}\int_{-\infty}^{\infty} < \exp\{-i\vec{Q}\cdot\overrightarrow{R_{j'}}(0)\}\exp\{i\vec{Q}\cdot\overrightarrow{R_j}(t)\} > \times \exp(-i\omega t)\,dt \tag{3.9}$$

$$\left(\frac{d^2\sigma}{d\Omega dE'}\right)_{inc} = \frac{\sigma_{inc}}{4\pi}\frac{k'}{k}\frac{1}{2\pi\hbar}\sum_{j}\int_{-\infty}^{\infty} < \exp\{-i\vec{Q}\cdot\overrightarrow{R_j}(0)\}\exp\{i\vec{Q}\cdot\overrightarrow{R_j}(t)\} > \times \exp(-i\omega t)\,dt \tag{3.10}$$

where coherent cross section $\sigma_{coh} = 4\pi(\bar{b})^2$, and incoherent cross section $\sigma_{inc} = 4\pi[\overline{b^2} - (\bar{b})^2]$. $\bar{b}$ and $\overline{b^2}$ stand for averaging over all b or b^2.

For elastic scattering, the neutron energy is unchanged. Therefore, by taking a time average, the expression of the differential cross section for coherent elastic nuclear scattering can be written as follows [68]:

$$\left(\frac{d\sigma}{d\Omega}\right)_{coh\ el} = N\frac{(2\pi)^3}{v_0}\sum_G \delta(\vec{Q} - \vec{G})\,|F_N(\vec{G})|^2 \tag{3.11}$$

$$F_N(\vec{G}) = \sum_j \bar{b_j}\exp(i\vec{G}\cdot\overrightarrow{d_j})\exp(-W_j) \tag{3.12}$$

In Eq. 3.11, N is the number of unit cells, v_0 is the volume of the unit cell, Q is the momentum transfer vector, G is a reciprocal lattice vector. $F_N(\vec{G})$ is the static nuclear structure factor, with atom sites labeled as j within the unit cell. $\bar{b_j}$ is the coherent neutron scattering length that depends on specific atomic species, $\overrightarrow{d_j}$ is the atomic coordinates. $\exp(-W_j)$ is the Debye-Waller factor that is related to random displacements of atoms from their thermal equilibrium. For small displacement:

$$W_j = \frac{1}{2} < (\vec{Q}\cdot\overrightarrow{u_j}) >^2 \tag{3.13}$$

where $\overrightarrow{u_j}$ is the atomic displacement vector.

The δ function in Eq. 3.11 determines that coherent elastic nuclear scattering only occurs when:

$$\vec{Q} = \vec{k} - \overrightarrow{k'} = \vec{G} \tag{3.14}$$

In contrast, incoherent elastic nuclear scattering usually appears as a sharp peak at E = 0 meV for all Q. Thus, elastic neutron scattering allows one to distinguish different crystal structures and characterize structural phase transitions in solid materials [62].

3.7 X-ray vs. neutron

Though the general principles for neutron and X-ray scattering are the same, XRD differs from neutron scattering in many ways. First, instead of scattering off the nuclei, X-rays interact strongly with the electron clouds of atoms via the electromagnetic force [72]. As a result, X-ray diffraction does not require to use of a large sample. Second, as shown in Fig. 3.5, the scattering length for X-ray increases with the atomic number. An atom with a larger number of electrons usually produces a stronger signal [76]. Meanwhile, the scattering length for neutron does not follow a specific pattern with the atomic number and can be very sensitive to different isotopes [77]. Finally, since X-ray photons carry zero magnetic moments, XRD is usually not used to probe the magnetic structures of the material (one exception is X-ray magnetic circular dichroism, which uses polarized light to obtain information on the magnetic properties of the atoms).

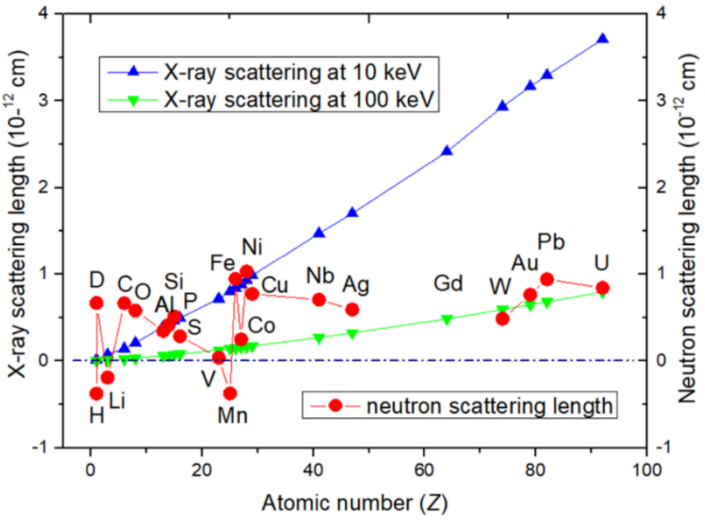

Fig. 3.5 A comparison of X-ray and neutron scattering length. The figure is from Ref. [78].

Chapter 4

Sample preparation and characterization

4.1 Introduction

Powder samples $Mo_{1-x}W_xTe_2$ were prepared using solid state reaction method while single crystals of $Mo_{1-x}W_xTe_2$ were obtained via self-flux growth method. In this chapter, the solid state reaction method and the self-flux growth method for sample preparation will be discussed. In addition, several measurement or analysis techniques have been utilized for sample characterization, including Rietveld refinements on powder XRD data, energy-dispersive X-ray spectroscopy and bulk resistivity measurements. These methods will be discussed as well.

4.2 Sample preparation

4.2.1 Solid state reaction method

$Mo_{1-x}W_xTe_2$ powders were prepared via solid state reaction method. For $MoTe_2$ and $Mo_{1-x}W_xTe_2$, elemental powders of Mo, W and Te, in a nominal ratio of $Mo_{1-x}W_xTe_{2.1}$, were thoroughly mixed and pressed into a pellet. The pellet was then sealed into an evacuated silica ampoule and heated at 950 °C for one to two days, before quenching in liquid nitrogen or water. For $x \lessapprox 0.08$, quenching is necessary to avoid the formation of the 2H phase [79]. For WTe_2, stoichiometric ratios of W and Te powders were used, and the sintering was done in an evacuated quartz silica ampoule at 900 °C for two days [49, 80, 81].

4.2.2 Self-flux growth method

Single crystals of $Mo_{1-x}W_xTe_2$ were grown using the self-flux growth method, and the temperature profiles used to prepare the crystals in the furnace differ depending on the W-level. To begin with,

$MoTe_{2.1}$, $Mo_{1-x}W_xTe_{2.1}$ or WTe_2 powder samples were prepared using solid state reaction. The sintered powder was then pressed into a pellet and sealed in an evacuated silica ampoule with excess Te flux, in a typical mass ratio of 1:3 of $Mo_{1-x}W_xTe_{2.1}$ to Te for $MoTe_2$ and $Mo_{1-x}W_xTe_2$, and in a molar ratio of 1:13 of WTe_2 to Te for WTe_2. The ampoule was then laid horizontally with a slight tilt downward toward the front of the box furnace. For $MoTe_2$ and $Mo_{1-x}W_xTe_2$ (x up to ~0.5), the ampoule was heated to 1150 °C at 100 °C/h and cooled steadily down to 950 °C in one to three weeks, before quenching at 950 °C in liquid nitrogen or water. For $Mo_{1-x}W_xTe_2$ having $0.5 < x < 1$, the ampoule with the initial material was heated to 950 °C at a rate of 100 °C/h, then cooled to 750 °C in one week. For WTe_2, the ampoule was heated at a constant temperature of 850 °C for 7 days, then quenched in water. The mass after the flux growth contains the $Mo_{1-x}W_xTe_2$ crystals and excess Te. Excess Te was removed in a post-annealing step. The ampoule was reinserted into a tube furnace at 1000 °C (for $MoTe_2$ and $Mo_{1-x}W_xTe_2$) or 900 °C (for WTe_2) with the material at the hot end (center) of the tube furnace, which enables to decant the molten Te flux towards the cold end. The ampoule was then quenched in water [49, 80, 81].

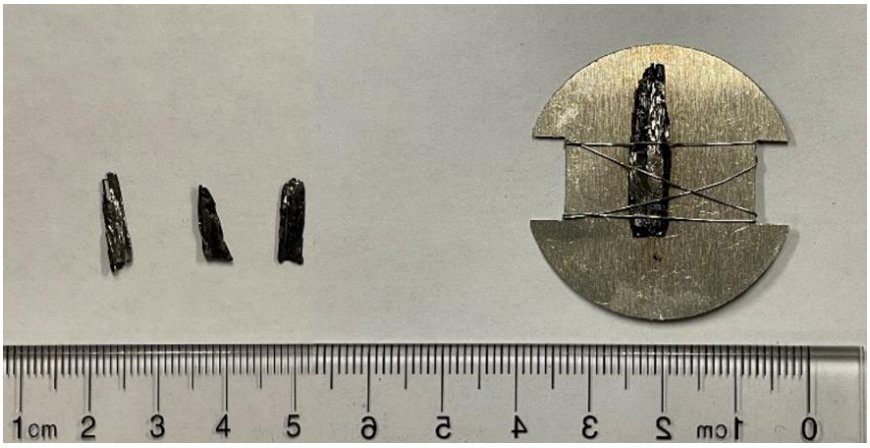

Fig. 4.1 Single crystals of $MoTe_2$ (three on the left) and $Mo_{0.94}W_{0.06}Te_2$ (the one on right, mounted on an aluminum plate).

Multiple single crystals of $Mo_{1-x}W_xTe_2$ with mass up to 0.1 g were usually obtained per flux growth. The crystals tend to grow along the b-direction, with a dimension of ~1 cm. The largest crystal used for elastic neutron scattering measurements is a $Mo_{0.94}W_{0.06}Te_2$ single crystal that weighs 0.6 g. Some $Mo_{1-x}W_xTe_2$ single crystals grown are shown in Fig. 4.1.

4.3 Sample characterization

4.3.1 X-ray diffraction

The general principle of diffraction was discussed in the previous chapter. In practice, room-temperature powder XRD data were collected on a laboratory X-ray diffractometer (Rigaku SmartLab SE), which is also equipped with an Anton-Paar TTK600 unit that allows measurements as a function of temperature.

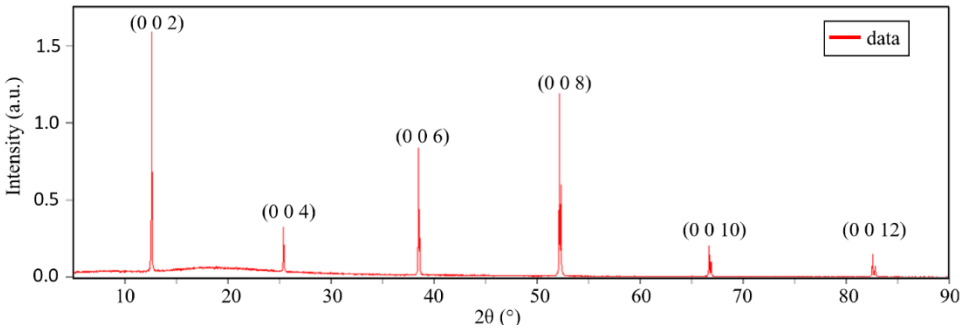

Fig. 4.2 XRD data collected on a $MoTe_2$ single crystal at room temperature. The pattern shows the expected layer spacing for the 1T' phase of $MoTe_2$. Similar XRD measurements were also performed on other $Mo_{1-x}W_xTe_2$ crystals that are discussed in later chapters.

Shown in Fig. 4.2 is the XRD data collected on a $MoTe_2$ single crystal as a function of the scattering angle 2θ at room temperature. For the XRD measurement, the crystal was positioned inside the diffractometer with their c-axis aligned along the perpendicular bisector between the X-

ray source and the detector. Therefore, only the (00L) Bragg peaks can be detected. The (00L) reflections appear at the correct 2θ positions which confirms the crystal structure is as expected for the 1T' phase of $MoTe_2$.

4.3.2 Rietveld refinements

Rietveld refinement is the most common powder XRD refinement technique used today, based on the method proposed in the 1960s by Hugo Rietveld [82]. The neutron or X-ray diffraction of powder samples results in patterns characterized by reflections (peaks in intensity) at certain positions. By fitting these peaks, the height, width and position can be obtained, which can then be used to determine the unit cell parameters, the atomic coordinates, the grain size and strain in the material. The Rietveld refinement was performed using the GSAS-II software [83], and the goodness of fitting is determined by a weighted residual of least-squares refinement parameter wR. The Rietveld refinement on the XRD pattern of Fe powder at 300 K is shown below in Fig. 4.3 as an example.

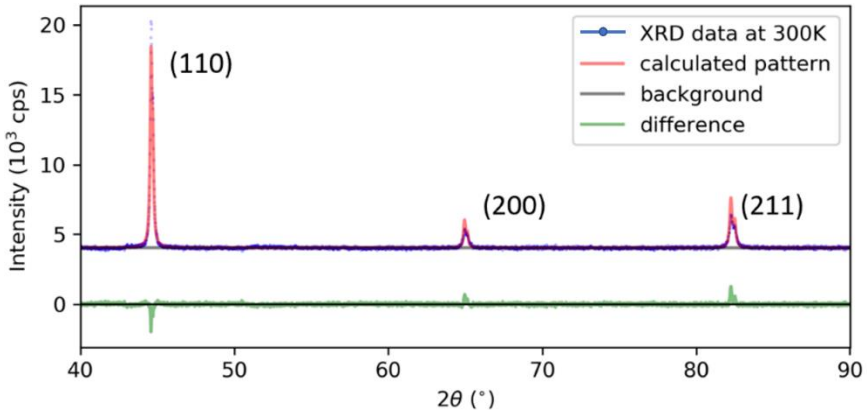

Fig. 4.3 Powder XRD on Fe at 300 K with Rietveld refinement performed. Peaks indexed in the pattern correspond to Bragg reflections. The wR value is 2.216%.

4.3.3 Energy-dispersive X-ray spectroscopy

A common elemental analysis method used to determine the atomic concentration of different elements in the material is EDS or EDX. EDS relies on the interaction of an X-ray source with the sample. The characterization capabilities are due in large part to the fundamental principle that each element has a unique atomic structure allowing a unique set of peaks on the electromagnetic emission spectrum [84]. For the EDS data collection, an FEI Quanta LV200 Environmental Scanning Electron Microscope instrument was used, housed in the Nanoscale Materials Characterization Facility (NMCF).

EDS measurements were performed on multiple $Mo_{1-x}W_xTe_2$ crystals to determine their W fractions. However, the W fractions estimated from EDS often differ substantially from their nominal x, potentially due to sample inhomogeneity (and also because EDS is a surface probing technique). Thus, in addition to EDS, c_{300K}, which is the spacing between the next nearest neighboring layers at 300 K (equivalent to the c-axis lattice constant of the T_d phase), is also used to help characterize the doping levels.

To establish a relationship between x and c_{300K}, XRD measurements were performed at room temperature on multiple $Mo_{1-x}W_xTe_2$ single crystals, and the c lattice parameters were obtained from the (00L) peak positions (calculated from Bragg's law using (002), (004), (006), (008)). Shown in Fig. 4.4 is a plot of the c lattice constants from XRD against the W fraction x from EDS measured on the same crystals. An overall nonlinear trend, where c monotonically increases with x, was observed. The uncertainty in measuring c_{300K} was small, evidenced by the low spreads in c_{300K} for $MoTe_2$ and WTe_2, which suggests that most of the scatter seen in Fig. 4.4 is due to

uncertainty in the EDS determination of x. Thus, the data points were fit with a quadratic curve that was kept fixed at the mean values for $MoTe_2$ and WTe_2.

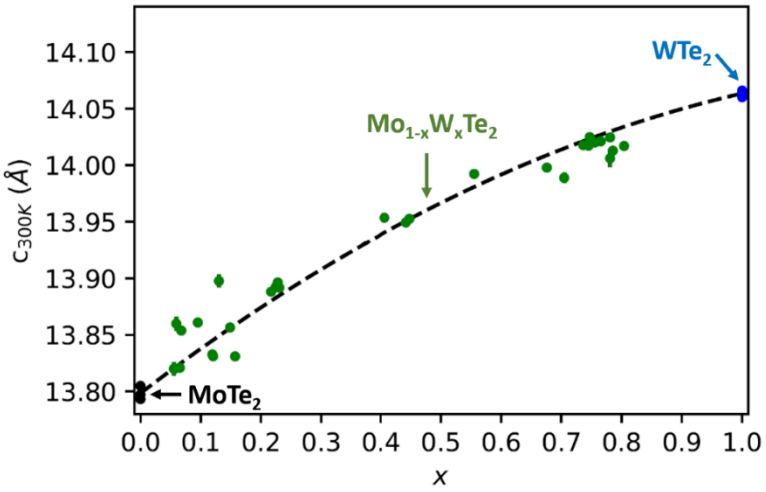

Fig. 4.4 Relationship between room-temperature c_{300K}, obtained from the positions of (00L) Bragg peak in XRD scans, and W fraction x, estimated from EDS measurements, of many small $Mo_{1-x}W_xTe_2$ crystal flakes. The dashed line represents a quadratic fitting of the data points, fixed at the endpoints to the mean c_{300K} values for $MoTe_2$ and WTe_2.

This quadratic relation was then used to convert c_{300K}, obtained from neutron scattering scans across the (004) nuclear Bragg peak, to the effective values of x in $Mo_{1-x}W_xTe_2$. One advantage of this method is that it allows to characterize samples by a quantity determined from the same aligned crystal domain as that used to obtain the rest of the neutron scattering data. Shown in Table I are the estimated effective W-fraction x, compared with the nominal W-fraction x from sample preparation, and c_{300K} of eight W-doped $Mo_{1-x}W_xTe_2$ crystals measured via neutron scattering. For convenience, $Mo_{1-x}W_xTe_2$ crystals are labeled as "MWT", and "MT" is used to for $MoTe_2$ crystals.

Table I: Values of c at 300 K extracted from neutron scattering scans, and the effective W-fraction x obtained from the quadratic relation as described for eight $Mo_{1-x}W_xTe_2$ crystals used for neutron scattering.

Sample name	Estimated x	Nominal x	c_{300K} (Å)
MWT1	0.087(25)	0.1	13.810(10)
MWT2	0.171(25)	0.4	13.842(10)
MWT3	0.21(4)	0.2	13.855(13)
MWT4	0.335(25)	0.3	13.897(10)
MWT5	0.420(25)	0.5	13.922(10)
MWT6	0.505(25)	0.7	13.946(10)
MWT7	0.542(25)	0.7	13.955(10)
MWT8	0.445(6)	0.5	13.9518(16)

4.3.4 Bulk resistivity

Resistivity is a measure of electron mobility of materials. Resistivity profiles are used to distinguish metals from insulators, and to discover novel physical phenomena such as superconductivity. Zero-field resistance on a $MoTe_2$ single crystal, and magneto-resistivity on a WTe_2 single crystal were measured using a Physical Property Measurement System from Quantum Design. The electrical resistance data collected on a $MoTe_2$ single crystal on cooling from 310 K to 2 K is shown in Fig. 4.5 (a). An anomaly in resistance was observed at ~250 K that corresponds to the T_d-1T' structural phase transition.

The quality of single crystals of WTe_2 was also characterized by measuring their XMR. Magneto-resistivity measurements were performed on a WTe_2 crystal under magnetic fields of 0 and 9 T, the results are shown in Fig. 4.5 (b). The residual resistivity ratio (RRR) from the 0 T data is calculated to be ~118(3). The WTe_2 crystal also have a large MR, with a magnitude of 51,553%

at 2 K under a 9 T magnetic field. These values are reasonably high [85], though higher values have been reported in literature, such as an RRR of ~370 and a MR of 452,700% at 4.5 K in an applied field of 14.7 T [29]. The resistivity data indicate the high quality of the WTe_2 crystals.

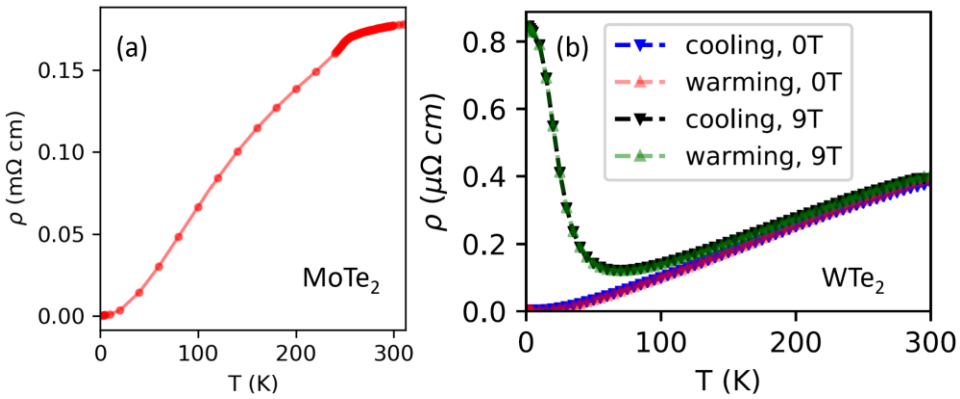

Fig. 4.5 (a) Electrical resistivity of $MoTe_2$, data collected on cooling from 310 to 2 K with the current applied along the b-axis. (b) Temperature and magnetic field dependence of resistivity in WTe_2, for current along the b direction and H || c. The relative error of each data point is ~0.001.

4.4 Summary

The solid state reaction method and the self-flux growth method to prepare $Mo_{1-x}W_xTe_2$ samples were discussed in this chapter. By combining the results from EDS measurements and the values of the c-axis lattice constants of the single crystals, the W-doping levels in $Mo_{1-x}W_xTe_2$ can be precisely determined. In addition, powder XRD and resistivity measurements show the high quality of the $Mo_{1-x}W_xTe_2$ single crystals.

Chapter 5

Emergence of T_d* phase in $MoTe_2$

5.1 Introduction

TMDs host many novel topological quantum phenomena such as quantum spin Hall effect and Weyl fermions. Recently, it was understood that a Weyl fermion can emerge as a quasiparticle in certain crystals, called Weyl semimetals. Weyl semimetals are conductors whose low-energy bulk excitations are Weyl fermions, whereas their surfaces possess metallic Fermi arc surface states [86]. Weyl fermions can be realized by breaking either the time-reversal symmetry or inversion symmetry of a three-dimensional Dirac fermion such that a pair of degenerate Dirac points separate into two bulk Weyl points with opposite chirality, which are connected by topological Fermi arcs when projected on the surface [32, 86-88]. Moreover, these exotic properties are topologically protected as they are robust against symmetry preserving perturbations.

Weyl semimetals can be classified into type-I and type-II depending on whether Weyl fermions emerge at the topological protected touching points of an electron and a hole pocket with strongly tilted Weyl cones. Weyl semimetals have not been realized until the discovery of TaAs in 2015 [88, 89]. While TaAs is the first known type-I Weyl semimetal, type-II Weyl fermions have been observed in the non-centrosymmetric, orthorhombic T_d phase of $MoTe_2$ from ARPES and scanning tunnelling spectroscopy studies [90]. Meanwhile, the high-temperature monoclinic 1T' phase of $MoTe_2$ is centrosymmetric, thus is topologically trivial.

Despite the discovery of the T_d and 1T' phases of $MoTe_2$ and the observation of a T_d-1T' transition [43], little work has been done on the structures of the two phases as well as the transition itself. As discussed in chapter 2, the T_d-1T' structural phase transition in $MoTe_2$ is more complex than

often thought, evidenced by the presence of diffuse scattering observed in both X-ray [43] and neutron scattering [58] measurements. Single crystal neutron diffraction measurements on TOPAZ suggest an inversion symmetry breaking in the 1T' phase during the transition to T_d, which is accompanied by substantial diffuse scattering suggesting stacking disorder.

Given the complexity of the stacking disorder that emerges across transition, it is critical to reveal the inversion symmetry breaking in $MoTe_2$ from elastic neutron scattering measurements, which are sensitive to the crystal symmetry. An examination of the T_d-1T' transition in $MoTe_2$ in more detail and a better understanding of the diffuse scattering across the phase boundary are needed. For a closer look at how the transition proceeds, elastic neutron scattering measurements were performed on two $MoTe_2$ single crystals, which are referred to as 'MT1' and 'MT2' for convenience, on the triple-axis spectrometers HB1, CG4C and HB1A at the High Flux Isotope Reactor (HFIR), and on the time-of-flight spectrometer CORELLI [91] at the Spallation Neutron Source (SNS) of Oak Ridge National Laboratory (ORNL) [80].

5.2 Measurement plan

Neutron scattering from a single crystal result in Bragg peak intensities in the reciprocal space, which can be uniquely indexed by the Miller indices of HKL. During the T_d-1T' transition in $MoTe_2$, the layer sliding along the a-axis (as shown in Fig. 2.1) will cause shifts of Bragg peaks along the L direction in the H0L plane. Therefore, to study the structural phase transition in $MoTe_2$, changes of certain Bragg peaks can be tracked as a function of temperature. Shown in Fig. 5.1 is simulated neutron scattering intensities in the H0L plane for the T_d and 1T' phases of $MoTe_2$. The black/red circles show the positions of Bragg reflections for T_d/1T', and the size of circles is proportional to the calculated nuclear structure factor squared (thus the peak intensity). Upon warming from T_d, the T_d Bragg peaks at integer values of L are expected. During the T_d-1T'

transition, the intensity of these T_d Bragg peaks will gradually decrease, and 1T' Bragg peaks will start to appear. Therefore, neutron scattering scans along the L direction can reveal the details of the T_d-1T' transition in $MoTe_2$.

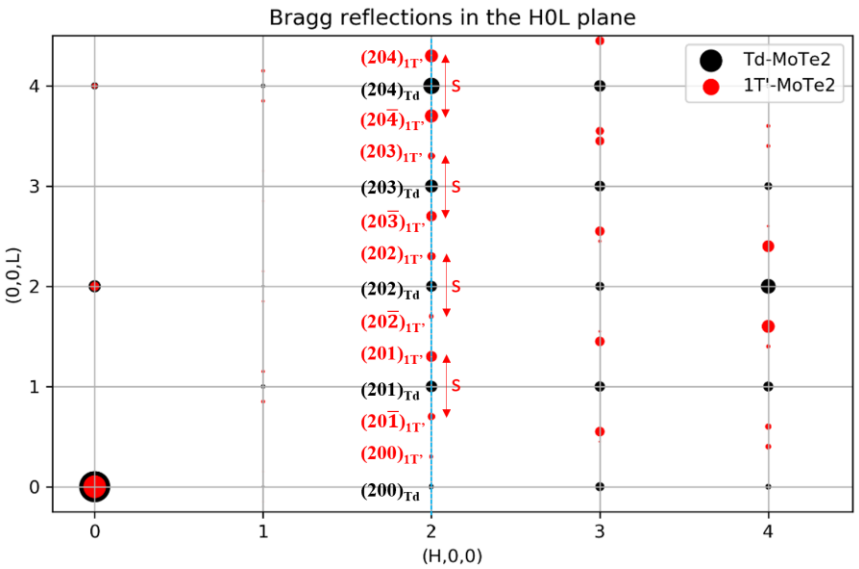

Fig. 5.1 Simulated neutron scattering intensity in the H0L plane for $MoTe_2$ (this map also applies in general to $Mo_{1-x}W_xTe_2$ and WTe_2). Black/red circles represent the Bragg reflections for the T_d/1T' phase, the size of the circles is determined by the calculated nuclear structure factor squared, which is proportional to the scattering intensity. s represents the distance along (2, 0, L) separating neighboring Bragg peaks of opposite 1T' twins. Here the orthorhombic (T_d) coordinates are used so Bragg peaks for the T_d phase appear at integer L.

For neutron scattering measurements on a triple-axis spectrometer, a single Bragg peak or scan along a specific direction in the reciprocal space is measured at a time. Therefore, the experimental plan is to perform measurements along the (2, 0, L) direction, mainly between L = 2 and L = 3. This is because: (1) The Bragg peaks of T_d and 1T' are well separated along L, which is beneficial in terms of resolution. (2) On average, the peak intensities are relatively strong. In addition,

longitudinal scans across the (002) or (004) peaks are performed to track changes in interlayer spacing. Though $MoTe_2$ is in the monoclinic phase at room temperature, for simplicity, all coordinates for the neutron scattering experiments are reported in an orthorhombic coordinate system with a ≈ 6.3 Å, b ≈ 3.5 Å, and c ≈ 13.8 Å, with c defined as twice the layer spacing, equivalent to the c-axis lattice constant in the T_d phase.

5.3 Emergence of T_d*

Shown in Fig. 5.2 (a-d) are scans of neutron scattering intensity along (2, 0, L) as a function of temperature on cooling and warming through the hysteresis for MT1 measured on HB1A and MT2 measured on HB1. The orthorhombic coordinates are used, which means the Bragg peaks of the T_d phase will appear at integer H, K, L indexes. Therefore, at low temperatures, Bragg peaks at L=2 and L=3 come from the T_d phase. Upon warming to ~260 K, an additional peak appears at L=2.5, which indicates a doubling of the unit cell along the c-axis. This peak is labeled as (205) T_d*, which is also shown in Fig. 5.2 (f), from an individual scan on MT1 on warming at 280 K. The transition from T_d to T_d* proceeds without diffuse scattering. On further warming, there is a gradual change from the T_d* phase to the 1T' phase, however, it is accompanied by substantial diffuse scattering that indicates stacking disorder. The diffuse scattering appears in a V-shape that spreads out from L = 2.5. In the 1T' phase, (202) and $(20\bar{3})$ Bragg peaks are observed at L=2.3 and L=2.7, respectively, from each of the two 1T' twins (D1 and D2). In contrast, on cooling from 1T' to T_d, the T_d* phase is absent and only diffuse scattering is observed, which also appears in a similar V-shape as on warming. However, the intensity shifts toward L=2.5 on cooling, suggesting a frustrated tendency toward T_d*. An example of the diffuse scattering is plotted in Fig. 5.2 (e), measured on cooling at 266 K. The T_d* phase is stable between 260 and 280 K, which is reproducible after the crystal was cycled through the hysteresis loop multiple times. The same cell

doubling pattern at the same temperatures on warming, regardless of the rate the sample was heated, and the same diffuse scattering pattern, on both warming and cooling along the hysteresis were observed.

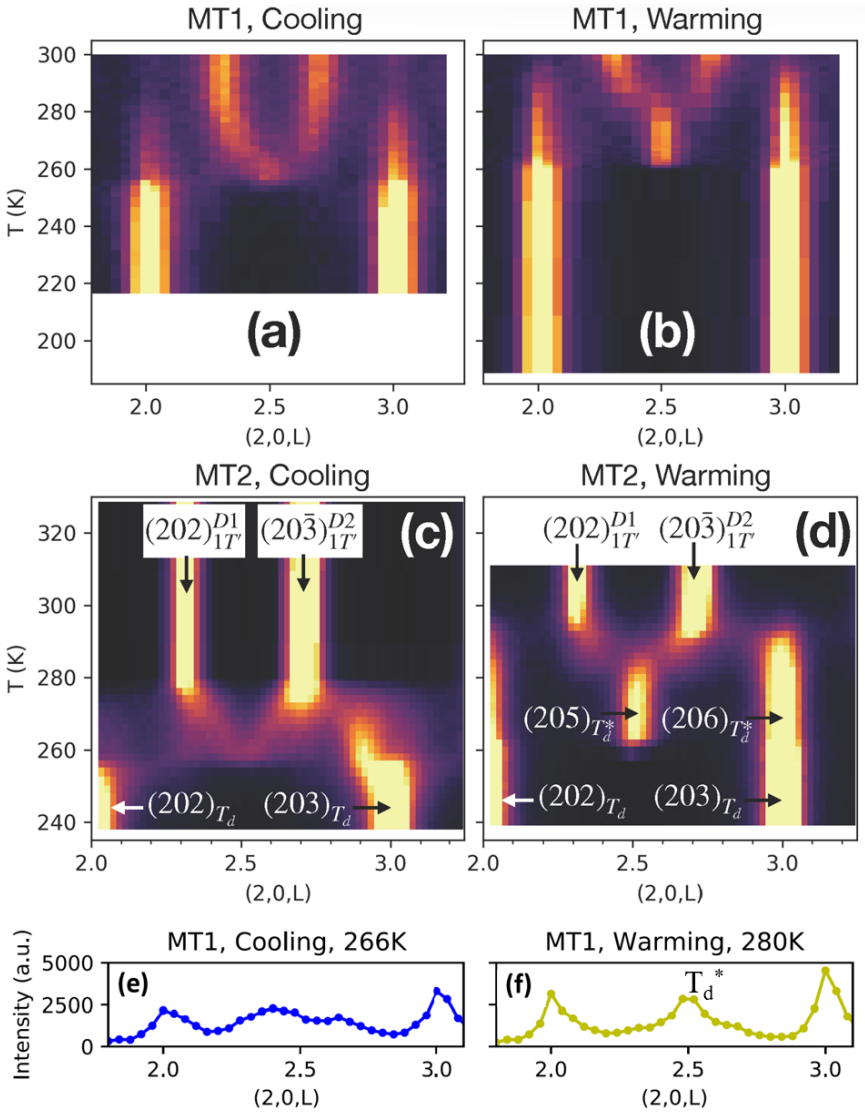

Fig. 5.2 (a–d) Elastic neutron scattering intensity measured along the (2, 0, L) direction combined at different temperatures on cooling and warming through the hysteresis loop for the MT1 (a, b) and MT2 (c, d) single crystals. (e, f) Individual scans along (2, 0, L) on MT1, showing diffuse scattering on cooling at 266 K, and the T_d* phase on warming at 280 K.

For a closer look at how the structural phase transition proceeds, in Fig. 5.3 the integrated intensity of four Bragg peaks as a function of temperature is plotted. The (203) T_d peak, the (205) T_d* peak, and the (202) and (20$\bar{3}$) 1T' peaks are included. The integrated intensities of these peaks were obtained from Gaussian fits of the data shown in Fig. 5.2 (c, d). Upon warming, the intensity of the T_d peak remains constant until a sudden decrease observed at around 260 K. At this temperature, the T_d* peak appears at the expense of the T_d peak. On further warming, the T_d* peak intensity decreases and disappears by 280 K, together with the T_d phase. At this temperature, diffuse scattering is observed, from which the Bragg peaks eventually become difficult to resolve. Therefore, fitting was not done within the pink shaded region. On further warming, the 1T' peaks appear. Meanwhile, on cooling below ~280 K, there is a steady decrease in the intensity of the 1T' peaks. At this temperature, diffuse scattering starts to appear prior to the crystal transforming fully back into T_d on further cooling.

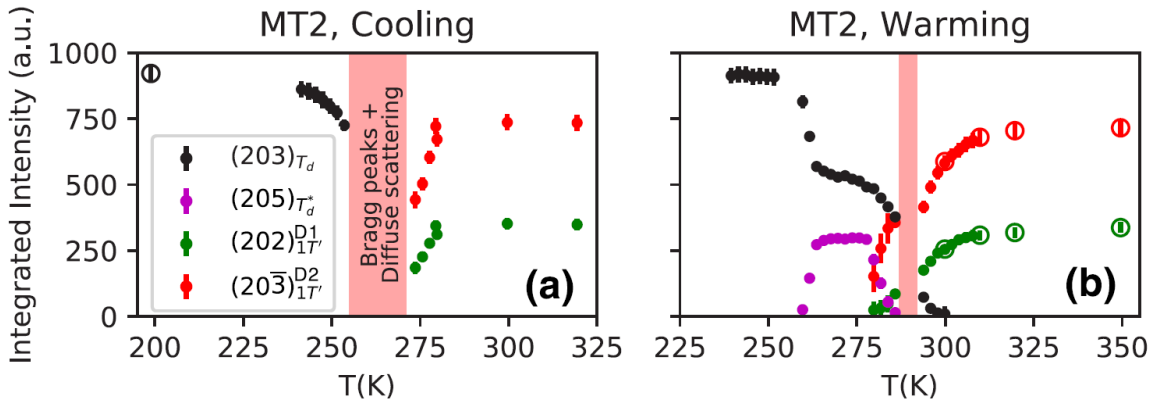

Fig. 5.3 Integrated Bragg peak intensity as a function of temperature on (a) warming and (b) cooling collected on MT2. Red bands denote regions where fits were poor due to the presence of substantial diffuse scattering. Solid symbols denote fits to the same hysteresis loop (with cooling data measured before warming). Open symbols correspond to another hysteresis loop.

On both cooling into full T_d or warming into full 1T', as shown in Fig. 5.3, there is a gradual increase in the integrated intensities of the T_d and 1T' peaks. It occurs due to a decrease in the remnant diffuse scattering. The diffuse scattering intensity along (2, 0, L) between Bragg peaks at several selected temperatures for MT2 is shown in Fig. 5.4 (from the same data set as Fig. 5.2 (c, d)). As the 1T' and T_d Bragg peak intensity increases on heating or cooling toward the temperature extremes, the diffuse scattering decreases. Meanwhile, on heating from T_d or cooling from 1T', no change is seen in the diffuse scattering until an onset temperature is reached (~280 K on cooling from 1T' to frustrated T_d*, and ~260 K on warming from T_d to ordered T_d*).

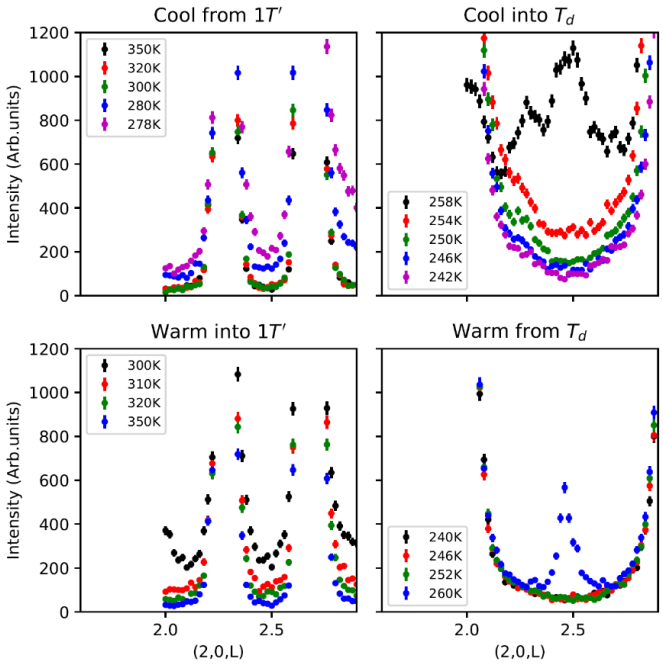

Fig. 5.4 Diffuse scattering intensity along (2, 0, L) at selected temperatures for MT2 when the crystal was warmed up or cooled down to and from the full T_d or 1T' phase.

The decrease in the remnant diffuse scattering in Fig. 5.4 is probably related to the long residual hysteresis observed in the resistivity measurements [92]. Shown in Fig. 5.5 (a) is the resistivity

data taken through a hysteresis loop from 300 K to 2 K and back to 300 K on a $MoTe_2$ crystal. A long tail in the hysteresis persists to low temperature. The difference between the cooling and warming resistivity data is plotted in Fig. 5.5 (b), the hysteresis persists down to at least 50 K. Therefore, the residual hysteresis in resistivity and the remnant diffuse scattering from neutron scattering scans are both likely related to changes in the presence of 1T' and T_d twin boundaries.

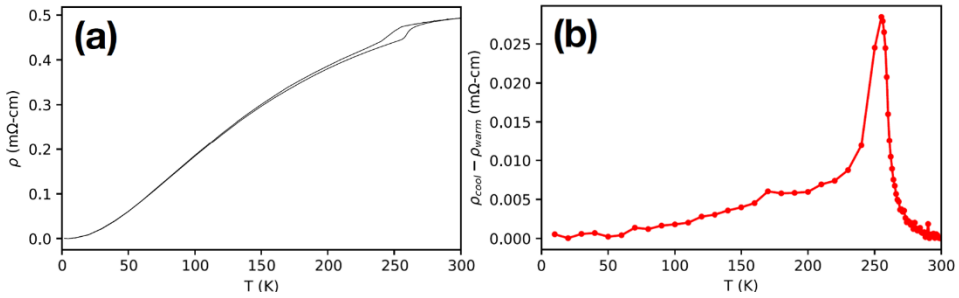

Fig. 5.5 (a) Resistivity measured on a $MoTe_2$ crystal. Data were taken on cooling from 300 to 2 K, then warming up to 300 K. (b) Difference between cooling and warming resistivity data in (a).

5.4 'AABB' stacking of T_d*

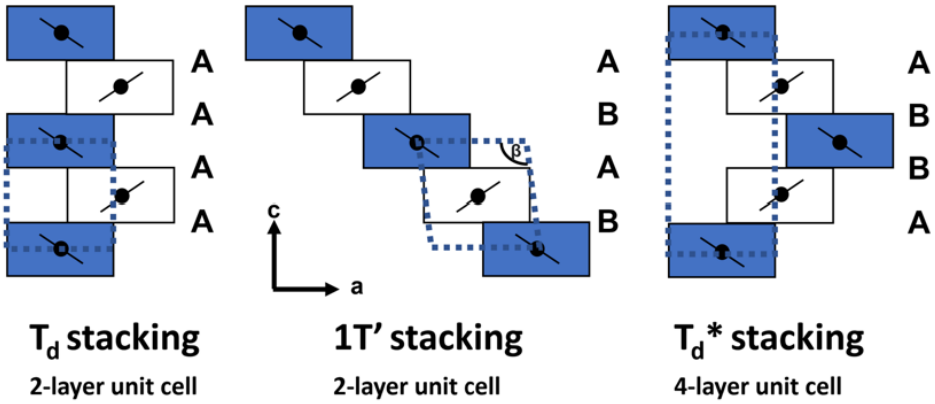

Fig. 5.6 The stacking sequences for the T_d, 1T' and T_d* structures. Dashed lines indicate the size of the unit cell, Rectangles show cells centered on inversion symmetry points for each layer.

Since the T_d and 1T' structures can both be built from the A- or B-type of stacking sequences, it is likely that the same is true for T_d*. The stacking sequence for T_d* can be deduced from the observation that it appears to be orthorhombic but has additional Bragg peaks at half-integer L values relative to T_d, indicating a four-layer unit cell. It turns out that there are only two possibilities, 'AABB' and 'ABBA', which are twins to each other. Shown in Fig. 5.6 is a comparison of the stacking patterns in the a-c plane for the T_d, 1T' and the proposed T_d* structures.

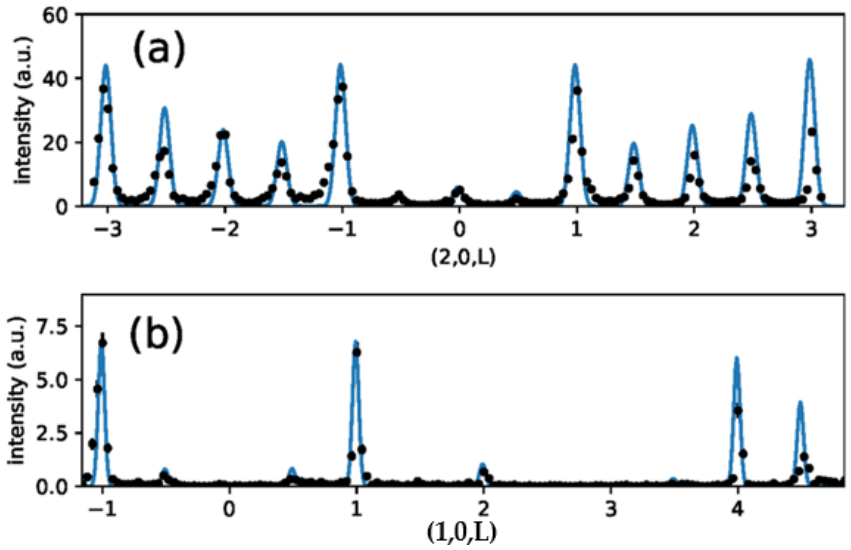

Fig. 5.7 Elastic neutron scattering intensity of MT2 (black dots) measured along (a) (2, 0, L) and (b) (1, 0, L), taken in the T_d* phase at ~266 K. Data were taken on CG4C at HFIR. Intensities in these plots are in the same arbitrary units. The blue curve is a simulation based on a model for the T_d* phase described in the text.

In Fig. 5.7, the neutron scattering intensity along (2, 0, L) and (1, 0, L) for the MT2 crystal in the T_d* phase is compared with a calculation that simulates the scattering intensity along the same directions using the proposed 'AABB' stacking model for T_d*. The calculation was optimized using a T_d* twin fraction distribution of 48% vs. 52%. There is a qualitative agreement between

the model and the data, suggesting that the "AABB" sequence does indeed describe the T_d* phase, though more data and refinement is needed to determine the atomic coordinates more precisely, which will be discussed in the next section.

5.5 T_d* structural refinement

To verify the proposed 'AABB' stacking sequence for T_d* and to determine the crystal symmetry, additional single-crystal neutron diffraction measurements were carried out on the MT1 crystal on CORELLI at the SNS of ORNL. The CORELLI experiment was conducted by Dr. Chunruo Duan. The data were collected on warming to 300 K. Shown in Fig. 5.8 (a, b) are the neutron scattering intensities in the 0KL and 2KL planes taken in the T_d* phase at 300 K. The presence of peaks at half-integer L in the 2KL plane confirms the presence of the T_d* phase. Besides, there is a lack of change in the (00L) and (01L) peak intensities between the T_d phase at 240 K and the T_d* phase at 300 K, as seen from the near-unity intensity ratios in Fig. 5.8 (c). (For context, intensity ratios for (20L) and (30L) peaks are also included.) A lack of change in the 0KL peak intensities as a function of temperature implies a lack of change in atomic positions along the b or c direction between T_d and T_d*, and it is consistent with the fact that layer displacements are along the a-axis, as is also the case between 1T' and T_d [58]. Interestingly, diffuse scattering from stacking disorder is also observed in the 2KL plane in the T_d* phase, which was already present on warming from 240 K, and there is a discrepancy between the detection of T_d* in MT1 at 300 K on CORELLI and up to ~280 K on HB1A. A possible explanation could be that the crystal measured on CORELLI was not cooled sufficiently into T_d beforehand (only cooled to 240 K, then measured on warming).

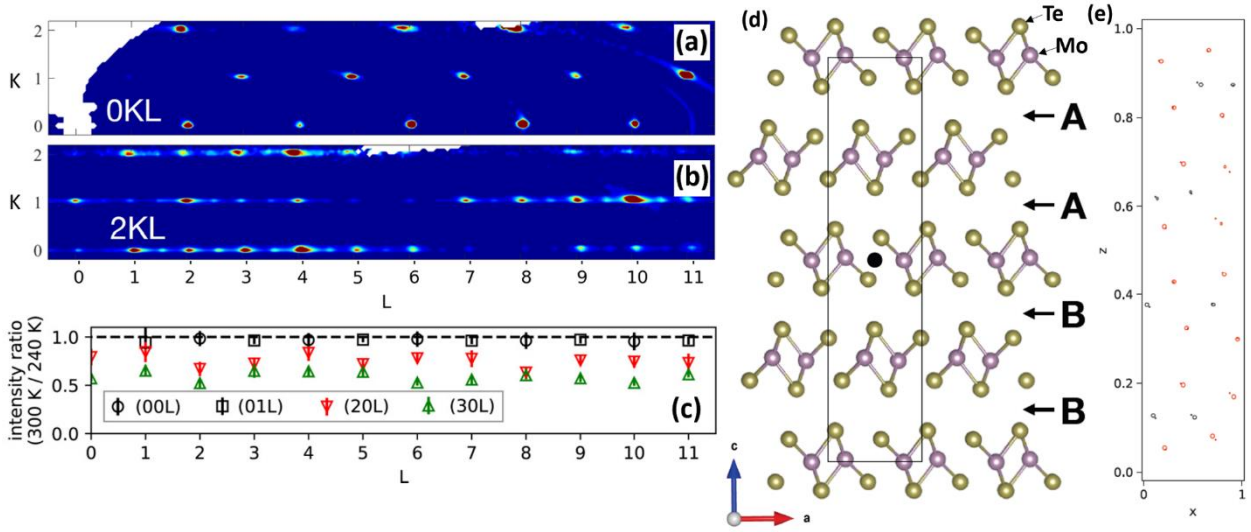

Fig. 5.8 (a, b) Neutron scattering intensities in the 0KL and 2KL planes in the T_d* phase measured on MT1 on warming at 300 K, data collected at CORELLI. (c) Intensity ratios of (00L), (01L), (20L) and (30L) peaks between the Td phase at 240 K and the Td* phase at 300 K. (d) Ideal crystal structure of the T_d* phase in the a-c plane, constructed from the 'AABB' stacking sequence. The black dot represents the inversion symmetry center. (e) Comparison between the refined T_d* coordinates (ellipses) and the ideal atomic positions (dots) in the a-c plane.

Refinements of the CORELLI single crystal neutron scattering data were performed to obtain the atomic coordinates of the T_d* structure. The fitting was done using Bragg peaks within $-1 \leqslant H \leqslant 8$, $-1 \leqslant K \leqslant 1$, $-20 \leqslant L \leqslant 20$, with the crystal symmetry set to $P2_1/m$, the highest possible for the AABB stacking. To match the data, it was necessary to consider a 47.8% volume fraction of T_d as well as 28.2% and 24.0% volume fractions of the two T_d* twins. The refinement shows an Rw factor of 0.13 and a $\chi 2$ value of 5.8. Fig. 5.8 (d) shows a comparison of the refined coordinates with the ideal atomic positions (constructed from AABB stacking of layers with the T_d-phase coordinates reported in Ref. [28]). The ideal atomic positions are plotted as dots and the refined coordinates are plotted as ellipses with heights and widths given by twice the uncertainties. The

two sets of coordinates overall agree with each other, with some deviations. However, such deviation would result in visible Bragg peaks in the 0KL plane at non-even K+L values, which were not seen in the data. Therefore, the ideal coordinates from the AABB stacking model are likely to be closer to the true T_d* structure than the refined coordinates. The refined atomic coordinates for the T_d* structure using the $P2_1/m$ space group are shown in Table II. Besides, refinement using another crystal symmetry, $P2_1$, was also attempted. However, it led to excessive peak intensities at locations where observed Bragg peaks are weak.

Based on the structural refinement results, the AABB stacking for T_d* is centrosymmetric, and the crystal symmetry of T_d* is $P2_1/m$, which is the same as that of the high temperature 1T' phase. To conclude, though T_d* appears to have an orthorhombic unit cell, the atomic positions are incompatible with the orthorhombic $Pnm2_1$ symmetry of T_d. As shown in Fig. 5.8 (d), the inversion symmetry center for the AABB structure is depicted as the black dot. Thus, T_d* is referred to as pseudo-orthorhombic.

Table II: Refined atomic coordinates in the T_d* phase of MT1 using the $P2_1/m$ space group. The lattice constants were a = 6.33 Å, b = 3.48 Å, c = 27.66 Å, and β = ~90°. The U_{iso} parameters were -0.002(5) for Mo and 0.002(4) for Te.

atom	x	y	z	atom	x	y	z
Mo1	0.71(2)	0.75	0.995(4)	Mo2	0.91(2)	0.25	0.250(3)
Mo3	0.33(1)	0.25	0.491(3)	Mo4	0.22(2)	0.75	0.253(4)
Te1	0.06(2)	0.75	0.054(5)	Te2	0.47(2)	0.25	0.308(4)
Te3	0.58(2)	0.25	0.074(5)	Te4	0.01(2)	0.75	0.322(4)
Te5	0.16(2)	0.25	0.170(4)	Te6	0.40(2)	0.75	0.429(5)
Te7	0.64(2)	0.75	0.199(4)	Te8	0.92(1)	0.25	0.452(3)

5.6 Centrosymmetric T_d* phase

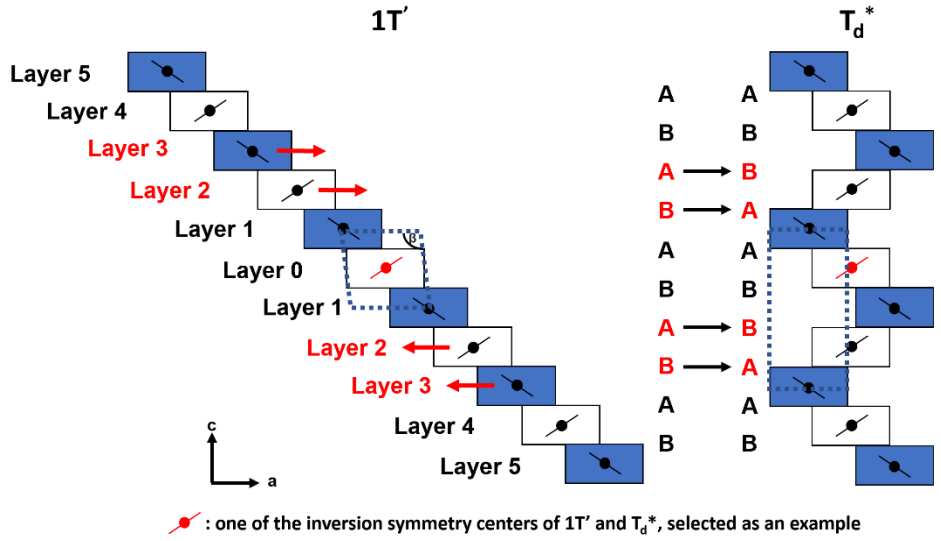

Fig. 5.9 Schematic representation of the structural transformation from 1T' to T_d*, that involves a series of layer translations along the a-axis (or equivalently, a series of A-to-B or B-to-A flips) that preserve the overall inversion symmetry center (red dot).

In addition to the structural refinements, another explanation is provided in this section as why the AABB stacking should be centrosymmetric, since the T_d* structure can be built from the centrosymmetric AB-stacked 1T' phase by applying a series of centrosymmetric translations along the a-axis. As shown in Fig. 5.9, starting from the ABAB stacking sequence for 1T', a layer (Layer 0) is randomly selected and fixed. In 1T', every layer has centers of inversion symmetry, the inversion symmetry center of Layer 0 (denoted by the red dot) is also the inversion symmetry center of the entire 1T' crystal. Next, let i denote the i-th nearest neighboring layer from the fixed Layer 0, either above or below as specified (Layer 1, 2, 3, etc.). Then, layers with indexes of $i = 2 + 4n$ and $i = 3 + 4n$ for every integer $n \geqslant 0$ are flipped. Flip means either A-to-B or B-to-A transformation, which involves a translation along the a-axis applied to the outside (Layer i+1) of

the given layer (Layer i). Because every A-to-B operation is balanced by a B-to-A operation on the opposite side of the fixed layer, the total sequence of translations mapping 1T' to T_d* preserves inversion symmetry. First-principles calculations also show that small non-centrosymmetric distortions are unlikely to happen, and $MoTe_2$ layers isolated from the non-centrosymmetric T_d environment tend to become centrosymmetric [93]. Thus, if T_d* has the AABB stacking, it should be centrosymmetric.

5.7 Resistivity of $MoTe_2$ revisited

Temperature dependence of the electrical resistivity of $MoTe_2$ has been widely studied before [28, 48, 94], and the hysteretic behavior observed at ~260 K was thought to be induced by the structural transition between the T_d and 1T' phases. To further investigate the phase boundaries between T_d, T_d* and 1T', the bulk resistivity of $MoTe_2$ is revisited, which suggests that the kink seen on warming near 260 K is likely the onset of the T_d* phase, not 1T'.

In Fig. 5.10 (a), integrated neutron scattering intensities near (2 0 2.5) are plotted for two different thermal hysteresis loops for MT2, which will be referred to as the 'narrow' and 'wide' hysteresis loops. The narrow hysteresis loop (black curve) corresponds to the sample being warmed into T_d*, then cooled back to T_d without entering the 1T' phase. Fig. 5.10 (b) shows how the (205) T_d* peak intensity changes along this narrow hysteresis loop as a function of temperature. It is clear that the transition from T_d to T_d* is likely to proceed without disorder, as diffuse scattering is not present even at a temperature a few Kelvin below the disappearance of the T_d* peak on cooling. In contrast, the wide hysteresis loop (green curve) is when the sample is warmed from T_d into 1T', then cooled back to T_d, from the frustrated T_d* region. The wide hysteresis loop is coupled with substantial diffuse scattering present on both warming and cooling, as can be also seen in Fig. 5.2 (c, d).

Nevertheless, for both narrow and wide hysteresis loops, a sudden decrease of intensity near (2, 0, 2.5) appears on cooling below 255 K, though more gradually for the wide hysteresis loop.

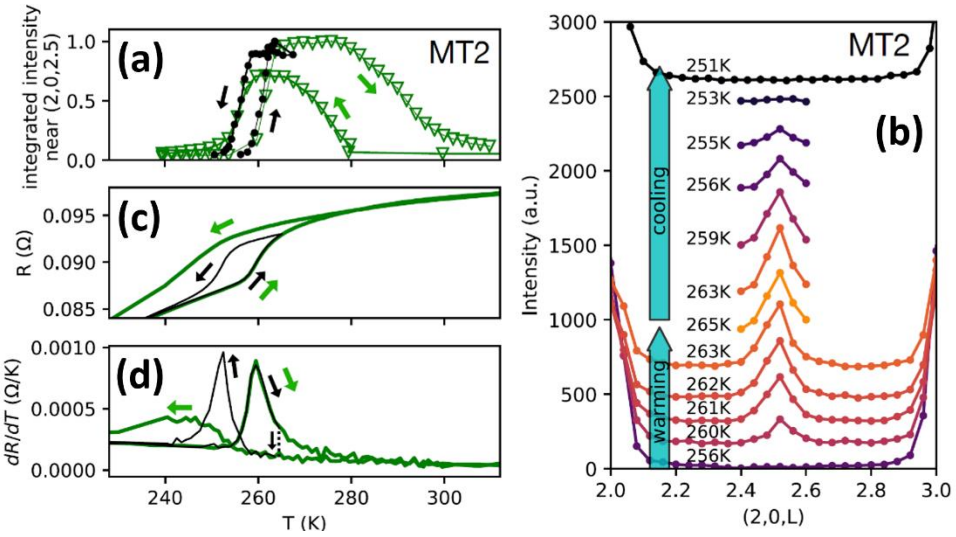

Fig. 5.10 (a) Integrated neutron scattering intensity near (2 0 2.5), within 2.39 ≤ L ≤ 2.61, for MT2 along two different hysteresis loops. Data taken on CG4C for the narrow hysteresis (black), and on HB1 for the wide hysteresis (green). (b) Neutron scattering scans along (2, 0, L) on MT2 at various temperatures along the narrow hysteresis loop. (c) Resistance of a $MoTe_2$ crystal measured through two hysteresis loops that begin on warming from 200 K. (d) The derivative dR/dT of the data shown in (c).

Interestingly, a similar pattern is observed in the resistance data measured on the MT2 crystal (residual resistance ratio RRR ~460) through the same narrow (200 to 265 K) and wide (200 to 350 K) hysteresis loops, the data were shown in Fig. 5.10 (c). On cooling, the resistance decreases quickly and in a symmetric manner for the narrow hysteresis loop, but more slowly and asymmetric for the wide hysteresis loop. Even so, the temperature at which both loops begin to bend downward on cooling is similar, which is more evident from the plot of derivative of resistance shown in Fig. 5.10 (d). Given the similarities in the onset transition temperatures between the hysteresis loops of

the neutron scattering intensity and bulk resistance of MT2, the conclusion can be made that the kink observed on warming at ~260 K indicates the onset temperature from T_d to T_d*, but not 1T'.

5.8 Discussion

Since the structural phase transitions in $MoTe_2$ involves layer sliding along the a-axis, the transition can be tuned by changing dimensionality (thickness). For example, in thin $MoTe_2$ crystals (hundreds of nanometers or less), the T_d-1T' transition is known to be broadened or suppressed completely [95, 96]. It is also shown that the magnetoresistance of $MoTe_2$ is also systematically suppressed with reduced thickness [97]. Therefore, a change of crystal thickness fundamentally affects the interlayer interaction in 2D materials. In this section, a qualitative discussion is provided on how the structural transition proceeds in $MoTe_2$ and the kinds of interlayer interactions that may be responsible.

First, from the integrated neutron scattering intensity near (2 0 2.5) shown in Fig. 5.10 (a), it is noted that the onset temperatures to the T_d phase are similar on cooling (both at ~255 K), regardless of whether it is from the ordered T_d* phase, or from the frustrated T_d* region. Given that the onset temperature to T_d does not appear to vary substantially with overall stacking disorder, short-range interlayer interactions might play the major role, which determine the onset temperatures to different phases (T_d, as well as T_d* and 1T).

On the other hand, long-range interlayer interactions may govern the gradual increase in Bragg peak intensities on warming into full 1T' or cooling into full T_d. As mentioned before, such gradual increase in Bragg peak intensities at temperature extremes corresponds to gradual decrease in the remnant diffuse scattering. This is because, at the twin boundaries, shifts of A to B or B to A (e.g., AAAABBB . . . to AAABBBB . . .) would not change the short-range environment. And the

decrease in diffuse scattering into T_d on cooling can be explained by the annihilation of these twin boundaries that result in changes in long-range interlayer interactions, either by joining in pairs or by exiting a crystal surface.

It is noted that interlayer interactions represent the dependence of an interlayer boundary's contribution to the free energy on the surrounding stacking, and can be indirect, involving changes to band structure, phonon dispersion, etc. Though the term "interlayer interactions" is used, these are effective interactions. Whether an interlayer boundary shifts from A to B depends on the free energy, which depends on the surrounding environment, which is specified by the A/B stacking sequence.

5.9 Summary

Using elastic neutron scattering on single crystals, the structural phase transition between a high-temperature monoclinic 1T' phase, and a low-temperature orthorhombic T_d phase in $MoTe_2$ is investigated. The structural phase transition in $MoTe_2$ mainly involves changes in layer stacking along the c-axis as a function of temperature. On warming from T_d, a cell-doubling structure T_d* is observed, that arises without diffuse scattering and corresponds to an 'AABB' sequence of stacking. The T_d* phase has a pseudo-orthorhombic structure and a four-layer unit cell, with a refined lattice symmetry of $P2_1/m$. Diffuse scattering is present on further warming from T_d* to 1T'. On the other hand, on cooling from 1T' to T_d, the T_d* phase is absent and only diffuse scattering is seen that suggests a frustrated tendency toward the 'AABB' stacking.

Chapter 6

Controllable T_d-1T' transition in $MoTe_2$ through W-substitution

6.1 Introduction

Interest in $MoTe_2$ has emerged due to the unique electronic properties associated with the structural phases, and doping $MoTe_2$ is known to be an effective approach to engineer the electronic band structures and controlled transitions between these phases. Among the doped compounds, $Mo_{1-x}W_xTe_2$ demonstrates a rich structure phase diagram and interesting physical properties. $Mo_{1-x}W_xTe_2$ has been predicted to be a tunable Weyl semimetal by varying x [36]. The length of Fermi arcs in T_d-$MoTe_2$ is tunable by temperature or by W-substitution [98, 99]. Based on ARPES measurements, the Weyl semimetal state has been reported in $Mo_{0.25}W_{0.75}Te_2$.

To fully understand the Weyl physics in $Mo_{1-x}W_xTe_2$, it is necessary to understand the structural phase diagram. However, previous studies on $Mo_{1-x}W_xTe_2$ show that the effect of W-substitution on the T_d-1T' transition has only been investigated via transport measurements or Raman spectroscopy up to x = 0.57 and 400 K [39, 54, 100], and the high temperature structures of $Mo_{1-x}W_xTe_2$ were inferred from room-temperature measurements throughout the phase diagram. Using additional methods such as elastic neutron scattering could elucidate the structures of $Mo_{1-x}W_xTe_2$ that were not studied at higher temperatures (for $x \geqslant 0.05$) and help fully control and utilize phase transitions in $MoTe_2$ through W-substitution [79].

In addition, novel structures can still be found in $Mo_{1-x}W_xTe_2$. In $MoTe_2$, The T_d-1T' transition is accompanied by the appearance of a centrosymmetric T_d* phase across the phase boundary [80]. The T_d* phase suggests that the transition from the Weyl semimetal phase to a topological trivial phase on warming in $MoTe_2$ is between T_d and T_d*, prior to the 1T' phase. Past studies of the Mo_{1-}

$_xW_xTe_2$ phase diagram did not observe the unit cell doubling [39, 54, 100], so a closer investigation of the phase diagram of $Mo_{1-x}W_xTe_2$ may still yield new phases with unique properties.

Neutron scattering is uniquely useful for measuring the structural properties of the entire crystal. Given the complex transition behaviors observed in $MoTe_2$, it is important to investigate and understand how the T_d-1T' transition proceeds in $Mo_{1-x}W_xTe_2$ with different levels of W, which is the focus of this chapter. Specifically, how the T_d* phase and V-shaped diffuse scattering evolve with W-substitution are investigated, and the trends of the δ parameter, the A/B stacking sequence, and the lattice parameters change as a function of W fraction are looked at [49].

6.2 Neutron scattering on $Mo_{1-x}W_xTe_2$

Elastic neutron scattering measurements were performed on several $Mo_{1-x}W_xTe_2$ single crystals on the triple axis spectrometers HB1, CG4C and HB1A at HFIR of ORNL, and also on the SPINS instrument at the NIST Center for Neutron Research of the NIST. For convenience, these crystals are labeled as 'MWT1' through 'MWT7' with increasing W substitutions, and their nominal and actual W fractions are shown earlier in Table I. Similar to $MoTe_2$, scans along (2, 0, L) were performed as a function of temperature. Shown in Fig. 6.1 are the elastic neutron scattering intensities as a function of temperature for seven $Mo_{1-x}W_xTe_2$ crystals.

For the lowest W-doped MWT1 crystal with $x \approx 0.09$, the transition behavior is very similar to that of $MoTe_2$ [80]. One difference is that the onset temperature to the T_d* phase on warming from the T_d phase now increases to ~280 K, instead of ~260 K for $MoTe_2$. With increasing W-fraction, there is a gradual transformation of the transition from a complex behavior with T_d* and V-shaped diffuse scattering, to a simpler phase-coexistence behavior between T_d and 1T'. For $MoTe_2$ and lower W-substituted $Mo_{1-x}W_xTe_2$ crystals, such as MWT1 and MWT2 ($x \approx 0.17$), the T_d* peak at

L=2.5 is observed only on warming. Meanwhile, the V-shaped diffuse scattering on cooling is much more subtle for MWT2 than MWT1. Similar behavior is also seen in MWT3 with x ≈ 0.21. By increasing the W-fraction to ~0.34, the T_d* peak is no longer seen in the MWT4 crystal, though there is a subtle increase in intensity near L=2.5. By MWT5 (x ≈ 0.42) and MWT7 (x ≈ 0.54), only phase-coexistence-like behavior between T_d and 1T' is seen. Therefore, the T_d* phase appears to be extinguished in $Mo_{1-x}W_xTe_2$ in the vicinity of x ≈ 0.21 to 0.34.

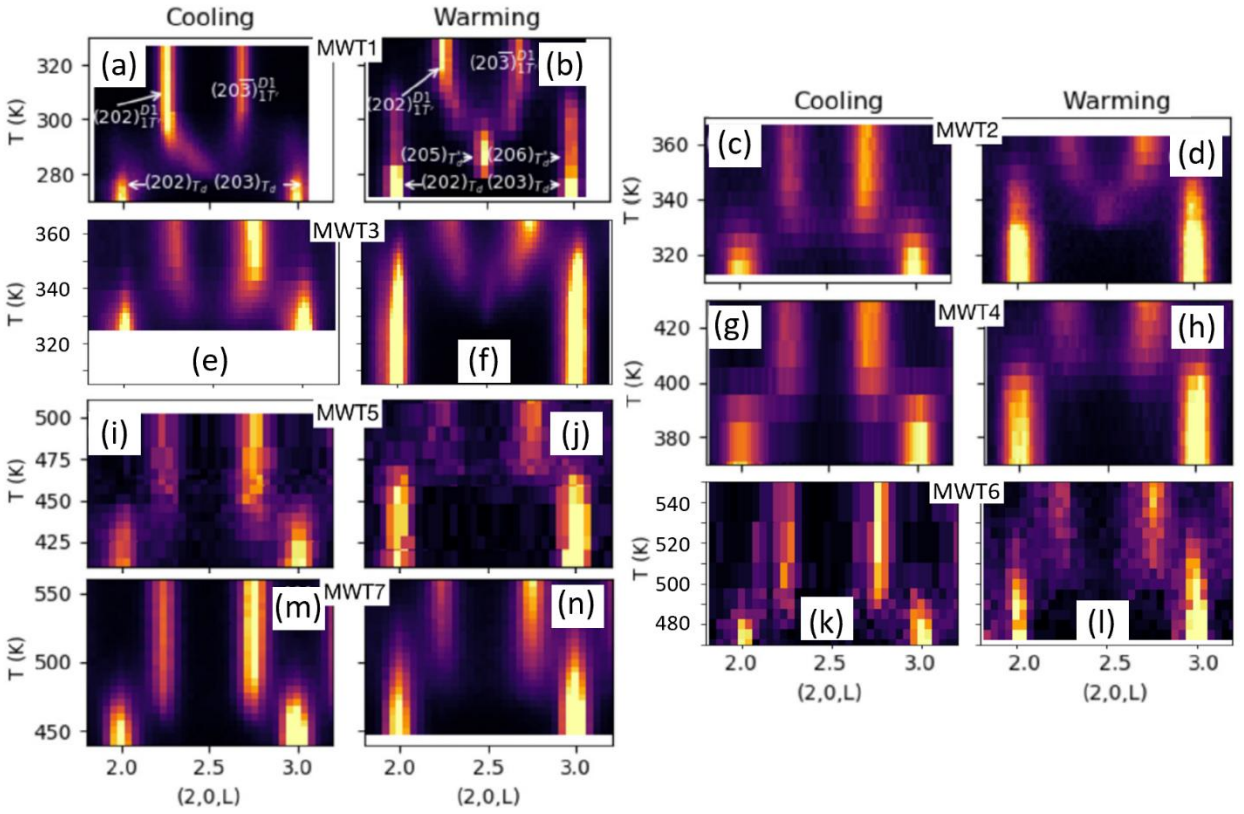

Fig. 6.1 Elastic neutron scattering scans along (2, 0, L), measured on seven $Mo_{1-x}W_xTe_2$ crystals with different W fractions, as a function of temperature on cooling (left) and warming (right) through the hysteresis. The plots are shown in order of increasing x. Data was collected at CG4C for MWT1, and at HB1A for the other crystals. For MWT1, Bragg peaks are labeled. D1 and D2 refer to the two 1T' twins.

6.3 Diffuse scattering simulation

The diffuse scattering observed across the phase boundaries in $Mo_{1-x}W_xTe_2$, and the associated disordered layer stacking are discussed in this section. As shown in Fig. 6.1, two types of transition behaviors are present in $Mo_{1-x}W_xTe_2$ with changes in W-fraction. The complex transition is accompanied by the V-shaped diffuse scattering seen on warming from the T_d* phase to the 1T' phase, and on cooling from the 1T' phase to the frustrated T_d* region. Meanwhile, the phase coexistence mainly involves a direct transition between T_d and 1T'. It is shown from simulation (performed by Dr. John Schneeloch) that the V-shaped diffuse scattering can be explained by having T_d*-like regions present within an overall 1T' phase, and the phase coexistence results from separated domains of T_d and 1T'.

Simulated elastic neutron scattering intensities along (2, 0, L) for two different models of stacking disorder that might occur on cooling from 1T' are shown in Fig. 6.2. For each of these models, the diffuse scattering along (2, 0, L) was computed by calculating the structure factor of points along this line for a supercell of 16000 $MoTe_2$ layers with different A/B stacking. Within a single layer, the intralayer atomic positions from Ref. [28] for the T_d phase were used.

Model #1 simulates the V-shaped diffuse scattering. Starting from a 50%/50% mixture of the two 1T' twins ('ABAB' and 'BABA'), a 'p' parameter is defined, which is the probability of flipping a pair of neighboring stacking from either 'AB' to 'BA', or 'BA' to 'AB', so that local T_d* regions are created. For example, in a block of B**AB**A of 1T', the AB-BA flip transforms this block into B**BA**A of T_d* (A**BA**B-A**AB**B for the other 1T' twin). In the 16000-layer supercell, the locations of the ABAB or BABA blocks were chosen at random, and the flipping was continued until a fraction p x16000 of flips occur. From Fig. 6.2 (a), with p increased to up to 0.2, Bragg peak

intensity decreases and diffuse scattering intensity increases, and the 1T' Bragg peaks near L = 2.3 and L = 2.7 shift towards L = 2.5 where the T_d* phase locates.

Model #2 represents the phase coexistence. Starting from the ABAB stacking of 1T', each B-type interlayer boundary has a probability p of flipping from B to A, thus bringing 1T' closer to T_d as p increases. For example, one such flip would bring AB**AB**AB... to AB**AA**AB.... It can be seen from Fig. 6.2 (b) that the intensity moves away from L = 2.5 and towards the T_d Bragg peak locations of L = 2 and L = 3, as these AAA...or BBB... regions were expanded by increasing p. This is opposite to model #1. Therefore, movement of the 1T' Bragg peaks toward L = 2.5 on cooling suggest the presence of coordinated AB-to-BA type shifts bringing 1T' closer to T_d*, rather than individual A-B shifts that would be a more direct path from 1T' to T_d.

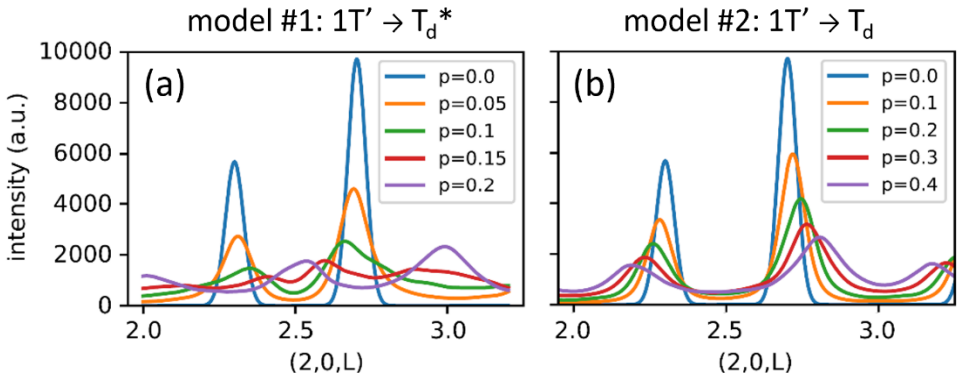

Fig. 6.2 Calculated elastic neutron scattering intensities along (2, 0, L), that simulate (a) the V-shaped diffuse scattering seen in lower W-doped $Mo_{1-x}W_xTe_2$ crystals, and (b) the phase-coexistence-like transition behavior seen in higher W-doped $Mo_{1-x}W_xTe_2$ crystals. For model #1, 'p' represents a probability of flipping in pair of 'AB' from the ABAB... stacking into 'BA', thus creating local T_d* stacking. For model #2, 'p' represents a probability of changing a B-type interlayer boundary from the ABAB... stacking to A-type interlayer boundary, thus introducing local T_d domains in 1T'.

6.4 Negative thermal expansion in $Mo_{1-x}W_xTe_2$

Thermal contraction is an unusual property. In $MoTe_2$, the c-axis is known to expand with decreasing temperature while a and b decrease slightly [101]. To further explore the structural differences as a function of W-fraction, the temperature dependence of the c lattice constant for the many $Mo_{1-x}W_xTe_2$ crystals studied by neutron scattering are plotted as a function of temperature, which is shown in Fig. 6.3 (a). The values of c were determined from the position of the (004) peak in longitudinal neutron scattering scans. For the three $MoTe_2$ single crystals, MT1, MT2 and MT3, a 0.4% decrease in the c-axis from 200 to 300 K was observed. With increased W-fraction, the thermal contraction on warming from MWT1 to MWT7 becomes less apparent. The curve for MWT7 is almost flat, suggesting that the c-axis has no temperature dependence for $Mo_{1-x}W_xTe_2$ when the W-doping level is around 54%. In some data, kinks are observed in the temperature dependence of c at temperatures that correspond to the T_d-1T' structural transition, which is likely due to a slight misalignment occurring during the transition. For example, in MWT1, the (004) peak was observed to move slightly in the angular direction during the transition. Combined with the anisotropy of the neutron scattering resolution function, this misalignment could be responsible for the apparent shift of the (004) position and thus c.

In addition, some powder neutron diffraction data was collected on the NOMAD instrument at the SNS of ORNL by Dr. John Schneeloch on powders of $MoTe_2$, $Mo_{0.8}W_{0.2}Te_2$, and WTe_2. In order to obtain the lattice constants from these powder samples, Rietveld refinements were performed in the T_d phase for all temperatures of WTe_2 and $Mo_{0.8}W_{0.2}Te_2$, and for the lower temperatures (10, 100 and 180 K) of $MoTe_2$. For $MoTe_2$ at 260 and 300 K, data were better fit with a mixture of the T_d and 1T' phases. The refined a, b, and c lattice constants as a function of temperature for both phases are shown in Fig. 6.3 (c-e). While the a- and b-axis lattice constants both increase with

temperature for all three compounds. The c-axis lattice constant changes oppositely for $MoTe_2$ and WTe_2, with a gradual change from negative to positive c-axis thermal expansion with increased W substitution.

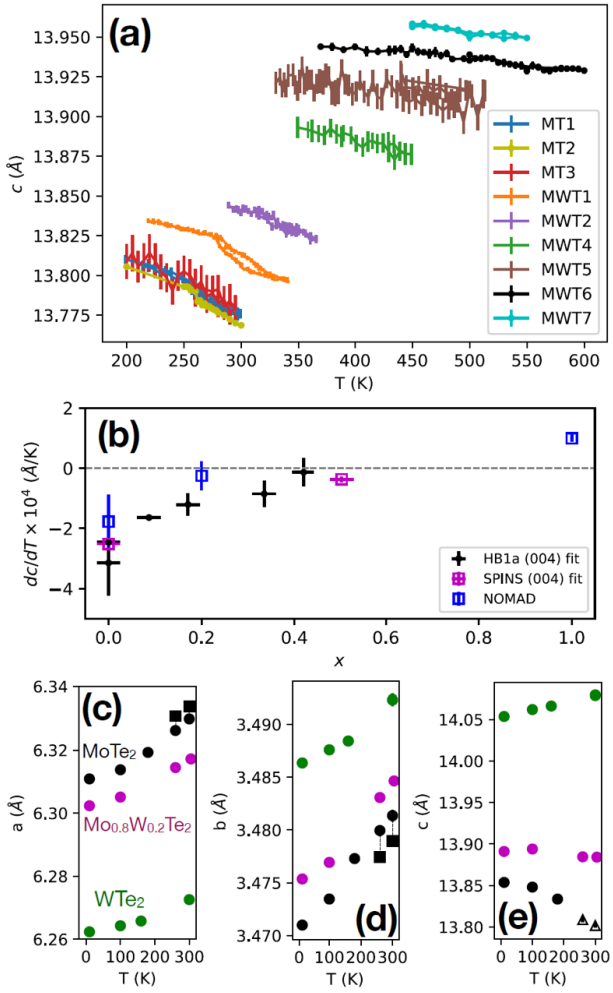

Fig. 6.3 (a) Temperature dependence of the c lattice constant of the $Mo_{1-x}W_xTe_2$ crystals studied by neutron scattering, data taken on HB1A and SPINS. (b) Estimated dc/dT at 300 K as a function of x, the values were obtained by linear fits through the data in (a). (c-e) Lattice constants a, b, c of $MoTe_2$, $Mo_{0.8}W_{0.2}Te_2$ and WTe_2 as a function of temperature from Rietveld refinements of powder neutron diffraction data taken on NOMAD. Circles and squares denote T_d and 1T' phases, respectively. Triangles denote c obtained from fits to the (002) peak.

From both the single crystal and powder neutron scattering data on $Mo_{1-x}W_xTe_2$, linear fits were performed through the temperature-dependent c lattice constant data points in the T_d phase closest to 300 K to obtain their slopes, dc/dT, as a function of W-fraction. The change in dc/dT from the c-axis thermal contraction of $MoTe_2$ to the more conventional c-axis thermal expansion of WTe_2 can be clearly seen in Fig. 6.3 (b).

6.5 Temperature dependence of β and δ parameters

Both T_d and 1T' phases can be specified by two parameters: the A/B type of stacking sequences and δ. The δ parameter not only characterizes the amount of displacement along the a-axis between neighboring layers, but also gives information about the interlayer potential energy landscape. For $MoTe_2$, the calculated total energy has two minima with respect to layer displacement along the a-direction [93], corresponding to T_d and 1T', with a separation called ϵ, ϵ was defined previously in Fig. 2.1 that characterizes the layer shift along the a-axis for B-type of stacking in fractional unit. The displacement along the a-axis for a B-type stacking can then be expressed as ϵ*a, where a is the 1T' lattice parameter. In the 1T' phase of $MoTe_2$, $\epsilon \approx \pm 0.15$ for each twin. The δ parameter is related to ϵ via $1 + \epsilon = 2\delta$. In the 1T' phase, such layer displacements result in two sets of nuclear Bragg peaks in the H0L plane that correspond to each of the two twins. The ϵ parameter can be measured from the distance s along (2, 0, L) separating neighboring Bragg peaks of opposite 1T' twins, when these twin peaks are centered about an integer L location. For example, if (202) Bragg peak is located at L = 2.3 and (20-2) Bragg peak is located at L = 1.7, then the peak separation s is 0.6. s was previously shown in Fig. 5.1. The relation between s and ϵ is given by the equation $s = 2H\epsilon$. The ϵ parameter is also related to the 1T' monoclinic β angle via the equation $\tan(\beta - 90°) = \epsilon * a/c$, where a and c refer to the 1T' lattice parameters.

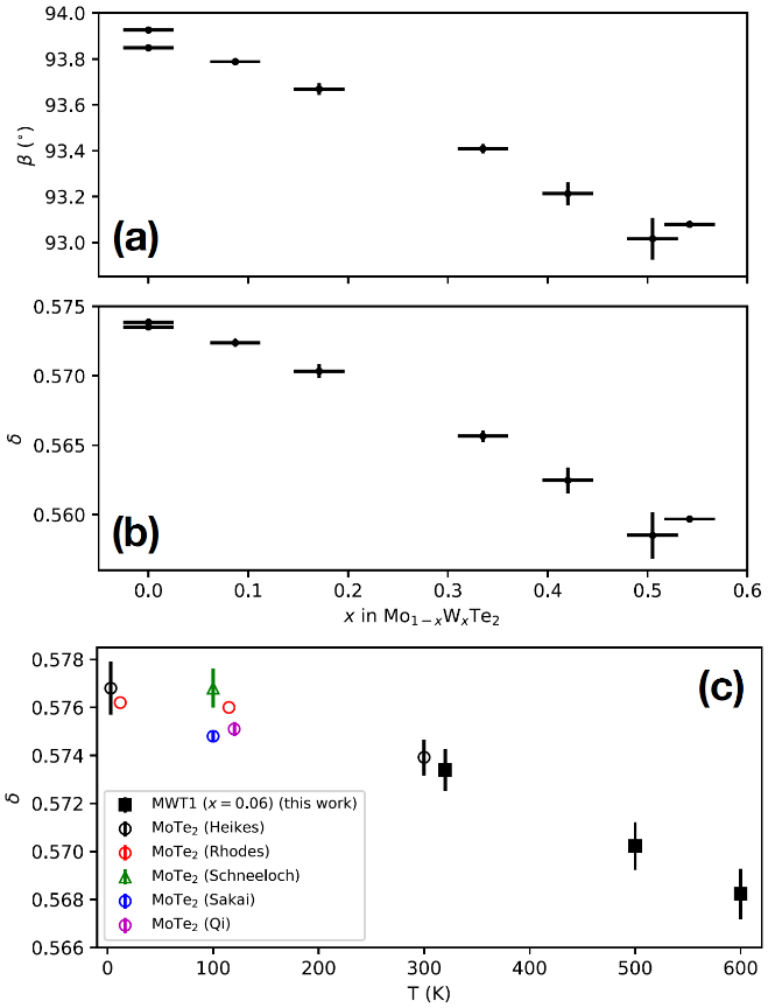

Fig. 6.4 (a, b) Changes of the monoclinic β angle in the 1T' phase and the interlayer displacement parameter δ of $Mo_{1-x}W_xTe_2$ as a function of W-fraction. (c) The δ parameter of the MWT1 crystal plotted as a function of temperature. The β and the δ values were extracted from the separation of the 1T' Bragg peaks along (2, 0, L) from the single crystal neutron scattering data.

Changes of the monoclinic β angle and the δ parameter as a function of W-fraction are shown in Fig. 6.4 (a, b). Decreases in both β and δ with W-substitution were observed [100]. The δ parameter appears to also have a temperature-dependence, that decreases with increasing temperature as shown in Fig. 6.4 (c), where δ values for the MWT1 crystal between 320 and 600

K are plotted. Since the MWT1 crystal is slightly doped with W (9%), which is close to stoichiometric $MoTe_2$, δ's for $MoTe_2$ calculated from reported atomic coordinates of the T_d and 1T' phases in literature are also included [28, 58, 93, 102, 103] and those values are consistent with the overall trend implied by our MWT1 δ values. Judging from the fact that the decrease in δ from 320 to 600 K in MWT1 is only a fraction of the decrease in δ from x = 0 to x = 0.5. The decrease in δ is likely a combined effect of W-substitution and temperature.

The strong anharmonicity in vibrations involving layer displacement along the a-direction [93] provides an explanation for the decrease in δ with temperature. If two layers oscillate relative to each other within a double-well potential (with each minimum corresponding to A- or B-type stacking), and the potential slope is less steep in directions toward the midpoint between the minima, then larger vibrations would be expected to shift the average interlayer position closer together, which corresponds to smaller ϵ and δ. In principle, the data suggest a trend where, at a sufficiently high temperature, δ would approach 0.5 and ϵ would approach 0, and a higher symmetry structure would result (T_0 structure which is calculated to be unstable in Ref. [104]). However, the rate of change of δ (~0.006 from 320 to 600 K) is too low for such a phase to be reached before thermal decomposition.

6.6 Unusual broad transitions in $MoTe_2$

Two $MoTe_2$ crystals, labeled as 'MT4' and 'MT5', show some unusual broad transition behaviors, which are shown in Fig. 6.5. The transition from the T_d phase to the 1T' phase occurs over a much broader temperature range, as compared with those from other $MoTe_2$ or $Mo_{1-x}W_xTe_2$ crystals (within 40 K). For the MT4 crystal, the elastic neutron scattering intensities along (1, 1, L) on both cooling and warming are shown in Fig. 6.5 (a, b). The $(11\bar{2})$ and (112) Bragg peaks from the 1T'

phase at high temperatures, and the $(11\bar{2})$ Bragg peak from the T_d phase at lower temperatures were observed. From Fig. 6.5 (a, b), it can be estimated that the hysteresis of the transition in MT4 is ~100 K. To better characterize the transition, intensities from individual scans along (1, 1, L) were fit with two Gaussian peaks with equal widths and an equal distance about L = -2. Shown in Fig. 6.5 (c) is change of the peak separation along L as a function of temperature. Upon cooling, the onset temperature of the transition into T_d is around 250 K, and the separation continues to decrease gradually down to at least 200 K. Meanwhile, the transition on warming starts at 200 K, and does not complete at 400 K.

For the MT5 crystal, the elastic neutron scattering intensities along (2, 0, L) combined at many temperatures are plotted in Fig. 6.5 (d, e), and the integrated intensity near L = 3 as a function of temperature is shown in Fig. 6.5 (f). The onset temperature of the transition on cooling into T_d is below ~240 K, as compared with ~280 K for MT1 or MT2. In addition, phase coexistence was observed by further cooling to even 200 K. On warming, a slight decrease in intensity near L = 3 is seen, followed by a steeper descent starting around 260 K, suggesting the onset of the transition into 1T'. The transition back to 1T' does not complete even up to 350 K. Interestingly, on subsequent measurements taken on cooling from 350 K to below ~100 K, as shown in Fig. 6.5 (g), the 1T' peaks near L = 2.3 and L = 2.7 are still visible.

A possible explanation for the broader transition observed in MT4 and MT5 is Te vacancies, which have been reported to broaden the transition in nominal $MoTe_2$ [105]. From EDS measurements, it shows vacancies in MT4 but not MT5, with Mo:Te ratios of 1:1.88(5) and 1:1.98(3), respectively. However, EDS is inconclusive as it only estimates the chemical composition from the surface of crystals. For MT4 and MT5, Te vacancies might be introduced during the post-annealing process to remove the Te flux, when the ampoule was inserted into the tube furnace for too long. Other

possible explanations for the broadened transition include oxygen or moisture, that might stabilize the 1T' phase in thin $MoTe_2$ crystals [106]. Thickness of the crystal might also play a role as sufficiently thin crystals of $MoTe_2$ have been reported to have a broadened transition [96].

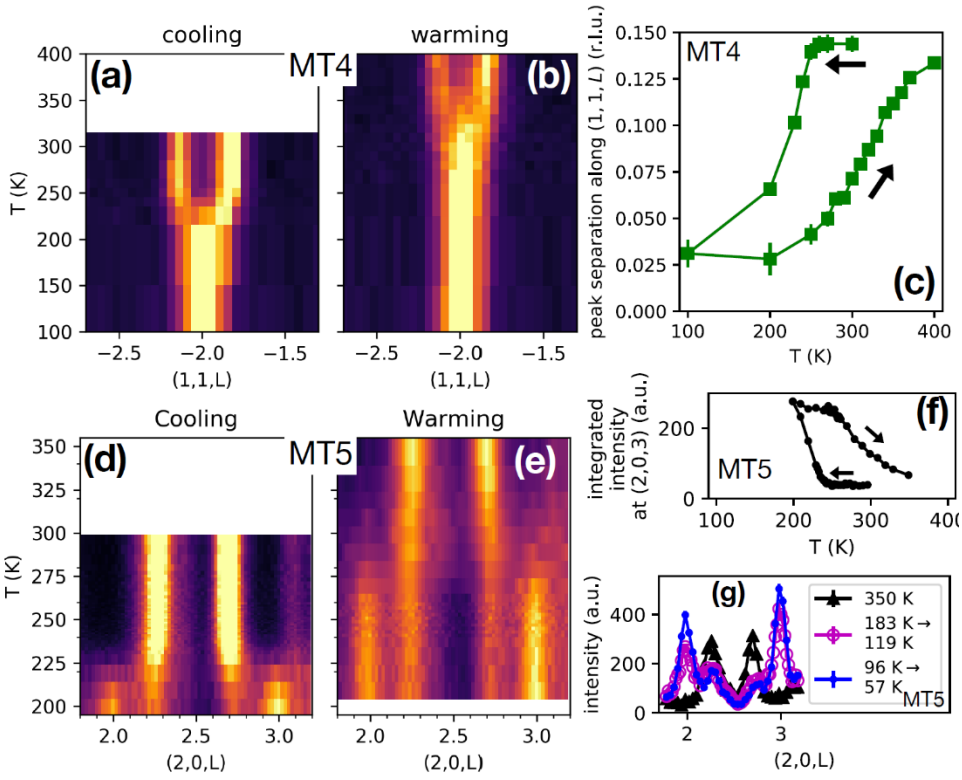

Fig. 6.5 (a, b) Elastic neutron scattering intensity along (1, 1, L) as a function of temperature measured on a nominal $MoTe_2$ crystal, MT4, at SPINS at the NCNR. (c) Fitted peak separation as a function of temperature from fits of neutron scattering scans in (a, b). (d, e) Elastic neutron scattering intensity along (2, 0, L) as a function of temperature measured on another nominal $MoTe_2$ crystal, MT5, at HB1 at HFIR. (f) Integrated intensity around the (203) T_d peak on cooling and warming from the neutron scattering scans in (d, e). (g) Individual scans along (2, 0, L) taken on MT5, first at 350 K, and then on cooling down to 57 K. Due to a heater malfunctioning, this cooling was uncontrolled, during which points were measured in order of increasing L within the ranges shown in the legend.

6.7 Structural phase diagram of $Mo_{1-x}W_xTe_2$

In Fig. 6.6 (a, b), the intensity of the (203) T_d peak as a function of temperature was plotted. At low temperatures in the T_d phase, the peak intensity is at maximum. At high temperatures in the 1T' phase, since there is no Bragg peak at L= 3, the intensity is at minimum. In between the extremes, two types of behaviors can be seen, depending on whether the transition is complex (which involves the T_d* phase and V-shaped diffuse scattering) or phase-coexistence-like (between T_d and 1T'). For crystals with lower W-fraction, two onset temperatures can be observed clearly on both warming and cooling. For example, for MWT1 on warming from T_d, the peak intensity drops abruptly at the onset to T_d* at 280 K. The intensity then plateaus, and near 305 K a second onset temperature is passed, beyond which the gradual transition into 1T' starts. On the other hand, the peak intensity changes differently on cooling from 1T'. a first kink is seen at the onset into the frustrated T_d* region near 305 K, and a second kink is seen at the onset into T_d near 280 K. There is no plateau on cooling that indicates the ordered T_d* phase. Nevertheless, each onset temperature is close together on warming vs. cooling, despite the crystal entering and leaving different structures. In contrast, for the higher W-substituted crystals, the onset to the transition is less sharply defined, and no intermediate onset temperatures are evident on warming or cooling.

The upper and lower boundaries of the T_d-1T' transition temperature range can be defined as the temperatures at which the (203) T_d Bragg peak intensity drops to 20% or 80% of its maximum value, seen as the dashed line in Fig. 6.6 (a, b). The phase diagrams of the T_d-1T' transition as a function of the W-fraction are shown in Fig. 6.6 (c, d), which contains three useful information. First, the transition temperature increases roughly linearly with x up to ~0.5. Second, the T_d* phase is only seen on warming up to x = 0.21. Third, the temperature range of the transition does not change substantially up to x~0.5, and the transition usually takes place over a 30 K range.

Interestingly, the transition under pressure tends to become broader [50]. It is noted that a peak appears near 0.5, which is likely due to the estimated W fraction from room-temperature layer spacing being slightly off, mis-ordering the true W fractions for the two x ~0.5 crystals.

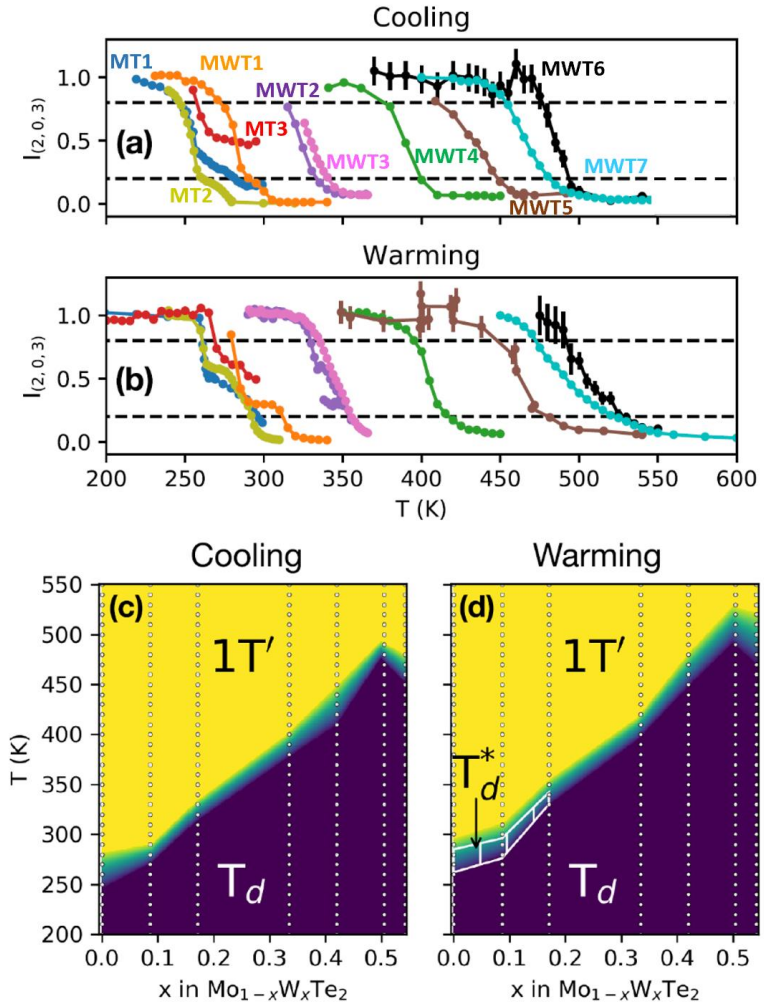

Fig. 6.6 (a, b) Neutron scattering intensity near (2,0,3), averaged over 2.95 ≤ L ≤ 3.05, on cooling and warming for all the $MoTe_2$ and $Mo_{1-x}W_xTe_2$ crystals measured with neutron scattering. The intensities were normalized to the low-temperature value for the T_d phase. The horizontal dashed lines show where the intensities decrease to 20% or 80% of the maximum, which are used to define the phase boundaries. (c, d) Phase diagram of $Mo_{1-x}W_xTe_2$ as a function of temperature and W-fraction on warming and cooling. Dots denote where data were taken.

6.8 Discussion

The nearly linear increase in the c-axis lattice constant as a function of temperature for WTe_2 in Fig. 6.3 (e) is striking different from the c-axis thermal contraction for $MoTe_2$ in Fig. 6.3 (a). Transport properties differ similarly. Shown in Fig. 6.7 is the temperature dependence of the electrical resistance for $MoTe_2$ and WTe_2. While the resistance curve is nearly linear as a function of temperature for WTe_2, it shows a downward curvature for $MoTe_2$. In addition, the Hall coefficient is reported to be nearly flat above 50 K for WTe_2 [107, 108], but continually changing for $MoTe_2$ [92, 103, 105]. The chemical potential μ(T) also appears to behave differently, moving in opposite directions for WTe_2 and $MoTe_2$ (as deduced from the Lifshitz transition in WTe_2 [107, 108] and optical conductivity measurements in MoTe2 [109]). Further research should clarify possible connections between the divergence in structural and electronic properties between WTe_2 and $MoTe_2$.

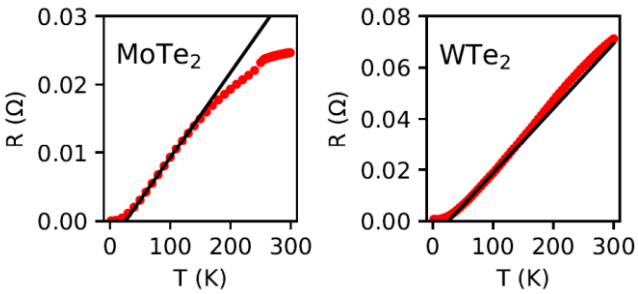

Fig. 6.7 Electrical resistance of $MoTe_2$ and WTe_2 collected on cooling from 300 K, with the current applied along the b-axis. The black lines represent linear fits to data between 50 and 100 K.

6.9 Summary

The T_d-1T' structural phase transition in single crystals of $Mo_{1-x}W_xTe_2$ up to x = 0.54 was investigated using elastic neutron scattering. Changes in the structure across the phase boundary

were characterized as a function of W substitution and temperature. With increasing W-fraction, the overall transition temperature increases, and there is a gradual transformation of the transition behavior from a complex transition that involves the T_d* phase and V-shaped diffuse scattering, seen in $MoTe_2$ and some of the lower W-doped crystals, to a direct transition from T_d to 1T'. The T_d* phase persists in $Mo_{1-x}W_xTe_2$ up to at least x = 0.21. The interlayer displacement parameter δ decreases with both temperature and W-substitution, along with the monoclinic tilting angle β. Increasing W-substitution does not substantially change the transition temperature range up to x ≈ 0.54, in contrast to the broadening seen under pressure. A phase diagram is created for $Mo_{1-x}W_xTe_2$ along hysteresis loops between T_d and 1T'.

Chapter 7

T_d-1T' transition in WTe_2

7.1 Introduction

WTe_2 belongs to the TMD family, which is best known as a type-II Weyl semimetal with a non-saturating XMR [90]. Both the Weyl fermions and XMR in WTe_2 are closely related to the crystal structure. While the former requires inversion symmetry breaking, as is for the T_d phase of WTe_2, the latter shows highly anisotropic behavior that is associated with the formation of Te-W-Te chains within the distorted 1T' layer. The XMR in WTe_2 reaches to 2,500,000% at 45 T and 4.5 K but is only achieved when the current is applied along the b-axis (W-chain direction) and magnetic field is parallel to c-axis (perpendicular to the layers) [29]. The XMR effect can drop by more than 90% when the magnetic field is applied along the a- or b-axis. Such XMR in WTe_2 has been explained by the nearly perfect balanced electron-hole populations along the b-axis in the T_d-phase, which suggests that the zig-zag W-chains impose an additional 1D structural characteristic on WTe_2 apart from the layered geometry.

What is also unique about WTe_2 is that the Fermi surface topology is sensitive to temperature. There is a temperature induced Lifshitz transition at around 160 K, which is associated with the complete disappearance of the hole pockets. This change of Fermi surface topology in the absence of a structure or magnetic phase transition is extremely rare [107]. As shown in the reported phase diagram of $Mo_{1-x}W_xTe_2$ in Fig. 2.4, WTe_2 is in the T_d phase at all temperatures. A 1T' phase of WTe_2 is not known so far and has been theoretically predicted to be absent up to at least 500 K. However, the crystal structure of WTe_2 has only been experimentally investigated up to 400 K via transport measurements under ambient pressure [45].

Nevertheless, whether a T_d-1T' transition occurs at ambient pressure in WTe_2 still needs to be investigated. Since the T_d-1T' transition temperature increases with W fraction in $Mo_{1-x}W_xTe_2$ up to x = 0.57 [39, 54, 79, 100], and a pressure-driven T_d-1T' structural transition in WTe_2 has been reported to appear at 4-5 GPa [110], at 8 GPa [46], and in a broad range from 6.0 to 18.2 GPa [47], there is a possibility of an ambient-pressure transition at a higher temperature that has never been accessed. A first study of the crystal structures of WTe_2 using elastic neutron scattering and XRD is presented in this chapter, where a T_d-1T' transition is observed at near 565 K in a single crystal of WTe_2. In contrast, the transition becomes much broader in powder WTe_2 [81].

7.2 Neutron scattering on single crystal WTe_2

Elastic neutron scattering measurements were performed on a single crystal WTe_2 on the triple-axis spectrometer HB1A at HFIR of ORNL. Fig. 7.1 (a, b) show the elastic neutron scattering intensity maps along (2, 0, L) as a function of temperature between 540 and 580 K. The data was collected first on warming, then on cooling.

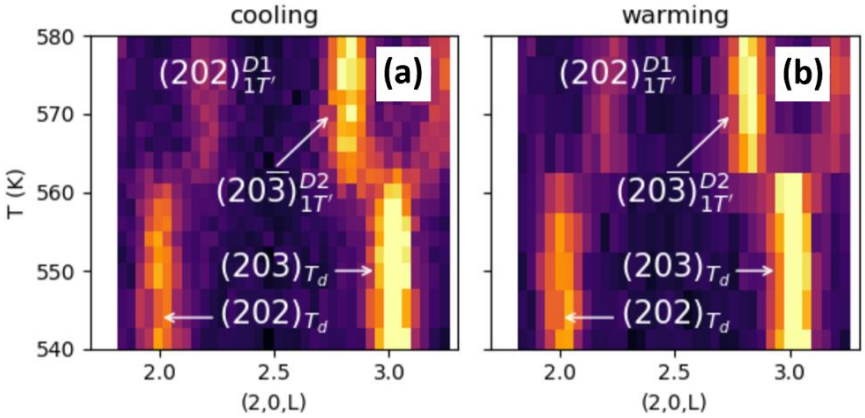

Fig. 7.1 Scans of neutron scattering intensity along (2, 0, L) collected on a single crystal of WTe_2 on (a) cooling and (b) warming. The Bragg peaks labeled D1 and D2 refer to the two 1T' twins.

At low temperatures, the (202) and (203) T_d Bragg peaks are observed at L = 2.0 and L = 3.0. On warming to around 565 K, a clear T_d-1T' transition can be seen from changes in the Bragg peaks. The (202) and (20$\bar{3}$) 1T' Bragg peaks appear near L = 2.2 and 2.8 on further warming. D1 and D2 labels refer to the two 1T' twins, with calculated volume fractions of around 48 % and 52 %.

Compared with $MoTe_2$, the structural phase transition in WTe_2 proceeds quite differently. Unlike the T_d* phase observed in $MoTe_2$, there is no intermediate phase present across the T_d-1T' phase boundary in WTe_2. The T_d-1T' transition in WTe_2 also occurs without the diffuse scattering seen in $MoTe_2$ [80]. Shown in Fig. 7.2 is the integrated intensity of the (203) T_d and (20$\bar{3}$) 1T' peaks from the neutron scattering measurements as a function of temperature through the hysteresis. The transition in WTe_2 is much sharper (mostly complete within ~10 K) than $MoTe_2$, as seen from the overlap of the warming and cooling curves. In contrast, the transition in $MoTe_2$ usually persists over tens of Kelvin, with a hysteresis in the resistivity observed at hundreds of kelvins away from the transition region [80].

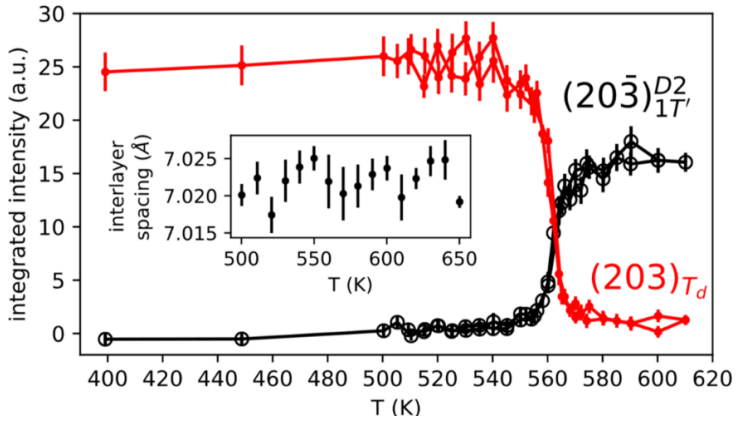

Fig. 7.2 Integrated intensity of the (203) T_d and the (20-3) 1T' Bragg peaks as a function of temperature, obtained from fits of neutron scattering scans along (2, 0, L). Inset: Temperature dependence of the interlayer spacing, obtained from fits to longitudinal scans along (004).

Structural phase transitions are often accompanied by abrupt changes in the lattice constants. In $MoTe_2$, negative thermal expansion of the c lattice constant was reported in both the monolayer and bulk compounds [111]. However, no change in the interlayer spacing was observed in WTe_2, evidenced by the inset of Fig. 7.2 that shows the interlayer spacing, obtained from fits to scans of the (004) Bragg peak, across the T_d-1T' transition boundary between 500 to 650 K. This is also different from the abrupt changes of lattice constant in WTe_2 seen under pressure [47]. The a-axis lattice constant did not change drastically either, given the similar intensity of the (2, 0, L) scans which was performed across the transition without realignment.

7.3 X-ray diffraction on powder WTe_2

In contrast to the sharp and clean transition observed in single crystals, the T_d-1T' transition is much broader in powder WTe_2, which persists on warming to at least 700 K. Powder XRD measurements were performed on a powder sample of WTe_2 on a laboratory X-ray diffractometer as a function of temperature between 300 and 700 K. The Rietveld refinements of the XRD patterns are shown in Fig. 7.3 (a-f). At 300 K, Bragg peaks of the T_d phase are observed, together with an impurity phase of WO_2 with a weight percentage of 5.1(1)%, which does not change over temperature. At 700 K, the XRD pattern is better fit with a combination of T_d and 1T' phases. In addition to the WO_2 phase, peaks corresponding to pure Te started to appear at 600 K, the intensity of which steadily increases on warming. The Te phase reaches a weight percentage of 8.13(17)% at 700 K. This Te phase suggests the decomposition of the WTe_2 powder at high temperatures and the possible presence of Te vacancies.

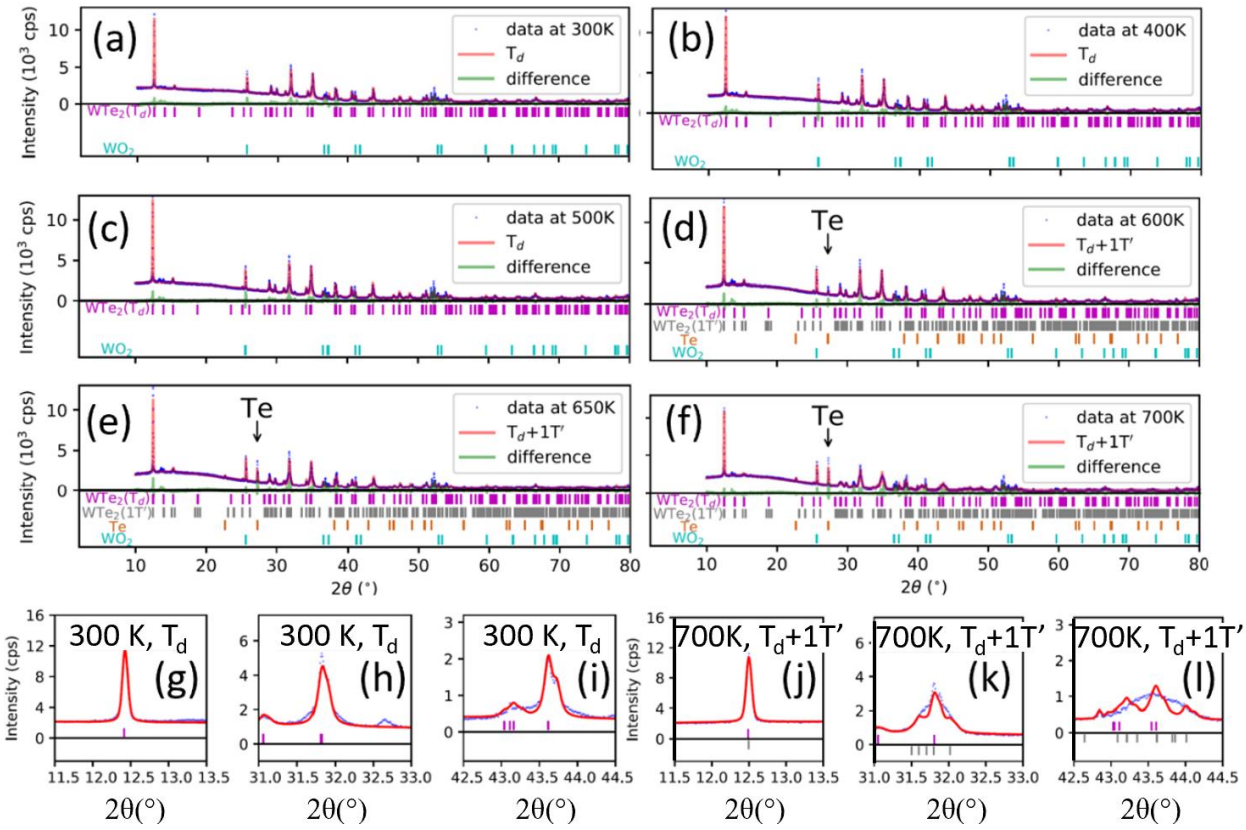

Fig. 7.3 (a-f) XRD patterns measured on a WTe_2 powder sample, data collected between 300 and 700 K on warming, the data were refined using T_d at 300, 400 and 500 K, and T_d and 1T' at 600, 650 and 700 K. Pure Te Bragg peaks are observed at 600 K and above. (g-l) XRD data plotted in zoomed-in regions (blue dashed lines) for 300 K (g)–(i) and 700 K (j)–(l) for the (0, 0, 2) peak (g), (j) and two other peaks. The red curves correspond to the refinements using the T_d phase or a T_d-1T' phase coexistence, respectively.

To better understand the T_d and 1T' phase coexistence at 700 K, a comparison of the diffraction data at 300 and 700 K is shown in Fig. 7.3 (g-l). At 700 K, the changes in intensity are roughly consistent with that expected from the model of a mixture of T_d and 1T' phases. (To refine the 1T' phase, the β angle was set manually so that the δ parameter corresponds to the δ parameter derived from the coordinates of the T_d phase portion at 700 K). While the model produces distinct Bragg

peaks, the data shows one broad peak. If such broad peak is due to the spread of lattice constants induced by powder decomposition, the (002) peak in panels (g, j) should also be broadened, which is not observed. The only explanation to the broadness seen in panels (k, l) would be disordered stacking, since the (00L) peak intensities only depend on atomic position along the c-axis.

Shown in Fig. 7.4 are the refined volume fractions of the T_d and 1T' phases as a function of temperature from the XRD data in Fig. 7.3. The transition in powder appears to be much broader than that in the single crystal, beginning at a temperature between 500 and 600 K, and was not fully completed even at 700 K. At 700 K, the T_d and 1T' phases coexist with relative volume fractions of 51 % to 49 %.

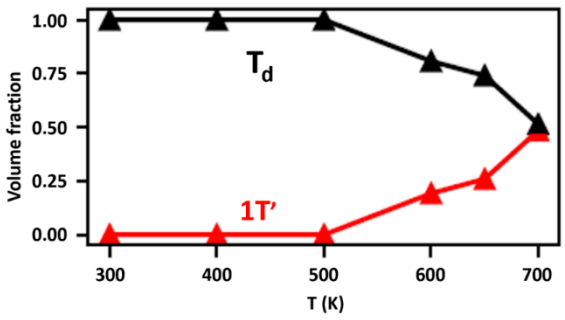

Fig. 7.4 The volume fractions of the T_d and 1T' phases as a function of temperature from refinements of the XRD patterns.

7.4 Stacking disorder in powder WTe_2

To illustrate how disordered stacking could contribute to the broadness of some diffraction peaks at 700 K, simulated XRD patterns from disordered stacking sequences progressing from T_d to 1T' are shown in Fig. 7.5 (a). The simulations were performed by Dr. John Schneeloch. Starting from the stacking model of 'AAAA…' of the T_d phase, every other interlayer boundary was swapped

from ‘A’ to ‘B’ with a probability ‘p’ [56]. A p value of 0 or 1 corresponds to the stacking of ‘AAAA…’ (T_d), or the stacking of ‘ABAB…’ (1T’). The diffuse scattering at different p values was calculated from the structure factor of the Bragg peaks using a constructed 1000-layer supercell. Increasing p from 0 to 1 result in an intensity shift from T_d peak location to 1T’ peak locations on each side, which explains the unfitted parts in Fig. 7.3 (k, l). It is noted that even though intermediate p values also produce distinct Bragg peaks, the broader intensity seen in the data could be due to inhomogeneity in the powder sample that has different values of p.

In order to highlight changes in the Bragg peaks on warming from 300 to 700 K, in Fig. 7.5 (b, c) the powder XRD data over two narrow regions are plotted, which are near 32° and 43.5°. The T_d peak intensity at 300 K decreases on warming and a broader intensity distribution becomes prominent by 700 K, indicating the shift of intensity towards the 1T’ peaks on both sides of T_d. The changes in the Bragg peak intensity on warming from 300 to 700 K in the XRD data is consistent with the changes of the simulated intensity by increasing p from 0 to 1.

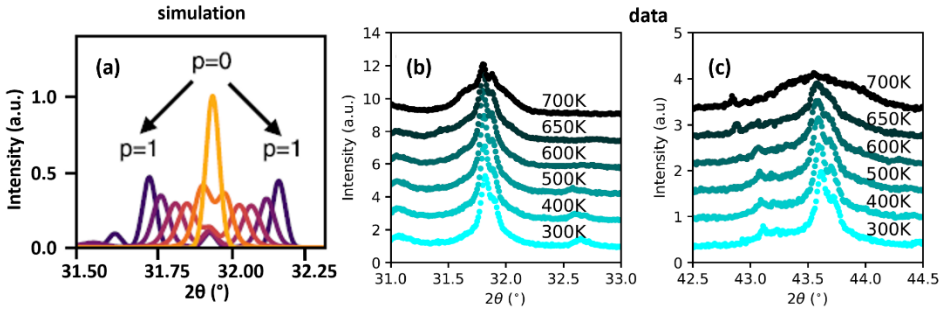

Fig. 7.5 (a) Simulated XRD intensities for T_d (p = 0), 1T’ (p = 1), and disordered stacking (0 < p < 1), intermediate between T_d and 1T’. p is the probability of a random swap of “A” with “B”-type stacking for every other interlayer boundary in the T_d AAAA... stacking. The simulated intensities are compared with the (b, c) XRD data over two narrow regions between 300 and 700 K.

7.5 Temperature dependence of lattice parameters

The δ parameter of WTe_2 from the XRD measurements was extracted from the refined atomic coordinates of the T_d phase and is plotted as a function of temperature as shown in Fig. 7.6 (a). δ from the HB1A data is also included, which is 0.5482(3) at 610 K obtained from the 1T' phase. The δ parameter decreases by ~0.007 from 300 to 600 K, which is very similar to the magnitude of decrease observed in MWT1. The refined T_d phase lattice parameters are shown in Fig. 7.6 (b-d). The expected thermal expansions for a, b, and c are observed except a possible anomaly near 700 K, which may be related to the decomposition that results in the Te phase, or to the difficulty in getting uniquely fitted lattice constants in the presence of stacking disorder. From the neutron data, a β angle of 92.456(17)° was also extracted.

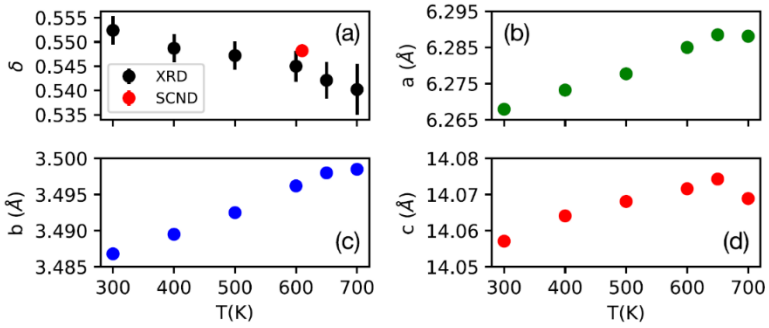

Fig. 7.6 (a) Temperature dependence of the δ parameter of WTe_2 from powder XRD (black) and single crystal neutron diffraction (red) measured on HB1A. (b-d) The temperature dependence of the lattice constants a, b, and c for T_d-WTe_2. The error bars for the points in (a-d) are smaller than the symbols except for the XRD δ points in (a).

The lattice constants for both T_d- and 1T'-WTe_2 as a function of temperature from Rietveld refinements of the powder XRD patterns are shown in Table III. For Rietveld refinements on data collected above 600 K, the monoclinic 1T' angle is fixed in the fitting at a value corresponding to

the parameter derived from the refined T_d phase atomic coordinates, where the δ value was calculated first then propagate to get β.

Table III: Temperature dependence of the lattice constants of the T_d and 1T' phases of powder WTe_2.

Temperature	T_d-WTe_2	1T′-WTe_2
300 K	a=6.2679 Å b=3.4868 Å c=14.0571 Å	N.A.
400 K	a=6.2732 Å b=3.4895 Å c=14.0641 Å	N.A.
500 K	a=6.2777 Å b=3.4925 Å c=14.0681 Å	N.A.
600 K	a=6.2850 Å b=3.4962 Å c=14.0716 Å	a=6.2875 Å b=3.4882 Å c=14.1130 Å $\beta = 92.302°$
650 K	a=6.2885 Å b=3.4980 Å c=14.0743 Å	a=6.2898 Å b=3.4902 Å c=14.1157 Å $\beta = 92.115°$
700 K	a=6.2881 Å b=3.4985 Å c=14.0689 Å	a=6.2859 Å b=3.4996 Å c=14.0728 Å $\beta = 92.058°$

7.6 Discussion

The T_d-1T' transition in WTe_2 single crystals is very sharp while the transition becomes much broader in powder WTe_2. There are several possible explanations for the broadness of the transition in powder. The first explanation is Te vacancies. Te vacancies have been proposed to broaden the transition in $MoTe_{2-z}$ crystals [105]. From the XRD data shown in Fig. 7.3, pure Te started to appear at 600 K and reached a weight percentage of 8.13% at 700 K. It is expected that powder

would have more decomposition than a single crystal due to a greater surface area to volume ratio. The second explanation is that the transition is broadened in the small crystallites of a powder sample. In thin $MoTe_2$ crystals (hundreds of nm or less) the transition is known to be broadened or suppressed completely [95-97]. In addition, there could be more defects in powder WTe_2 induced during sintering or grinding. Defects may frustrate layer sliding, and the presence of grain boundaries would frustrate the shape change expected in each grain's T_d-to-1T' transition.

7.7 Summary

Using elastic neutron scattering on a single crystal and XRD on a powder sample of WTe_2, a T_d-1T' structural phase transition was observed in the Weyl semimetal WTe_2 at ambient pressure. In the crystal, the transition is very sharp, occurs at ~565 K, and proceeds without hysteresis. No intermediate phase was observed across the phase boundary, in contrast to the T_d* phase seen in $MoTe_2$. Meanwhile in the powder, the transition is broadened and incomplete up to 700 K, with phase coexistence across a wide temperature range.

Chapter 8

T_d-1T' transition under pressure

8.1 Introduction

Due to the weak interlayer interaction, both $MoTe_2$ and WTe_2 are relatively easy to be compressed under external strain or pressure, and their physical properties can thus be changed. For example, the band structure of $MoTe_2$ is quite sensitive to external strain. Density functional theory (DFT) calculations showed that only two pairs of Weyl points exist rather than four pairs under ambient condition, whereas the other two pairs were annihilated by merging at the Γ-X line [87]. With external hydrostatic pressure, the critical temperature for superconductivity in $MoTe_2$ dramatically increases from 0.1 K to 8.2 K at 11.7 GPa [28].

The T_d-1T' structural phase transition in $Mo_{1-x}W_xTe_2$ can also be tuned by applying strain to the crystal. In WTe_2, pressure converts the T_d phase to 1T', at relatively high pressure ranging from 6 GPa to 15.5 GPa [46, 47]. In $MoTe_2$, pressure suppresses the temperature of the T_d-1T' transition, and the T_d phase is no longer observed by ~1.2 GPa [28, 50, 93]. Tensile strain along the a- or b-axes, on the other hand, has been reported to decrease and increase the transition temperature in $MoTe_2$, respectively [112]. However, the effect of hydrostatic stresses on $Mo_{1-x}W_xTe_2$ has not been studied with diffraction techniques, and the question remains of how hydrostatic pressure would affect structural properties, such as the novel T_d* structure, that has been found in $Mo_{1-x}W_xTe_2$ ($x \leqslant 0.21$). It is expected that changes with hydrostatic pressure might be relevant to the interlayer interactions that give rise to the transition between 1T' and T_d. Given that W-substitution and hydrostatic pressure have opposing effects on transition temperatures, the effects of simultaneous

pressure and W-substitution were investigated by performing neutron scattering measurements on a crystal with nominal composition $Mo_{0.8}W_{0.2}Te_2$.

8.2 Neutron scattering on $Mo_{0.8}W_{0.2}Te_2$

The high-pressure elastic neutron scattering measurements were performed on HB1 by Dr. Sachith Dissanayake. The pressure cell was a CuBe self-clamped piston cylinder cell. Daphne 7373 oil was used as the pressure transmitting medium. The pressure was calibrated using lattice constant measurements from an attached NaCl crystal. At each pressure (0.53, 0.88, 1.20 and 1.40 GPa), a series of scans of intensity along (2, 0, L) were taken on cooling and warming from 300 K to ~5 K and back to 300 K. Data under pressure are shown in Fig. 8.1.

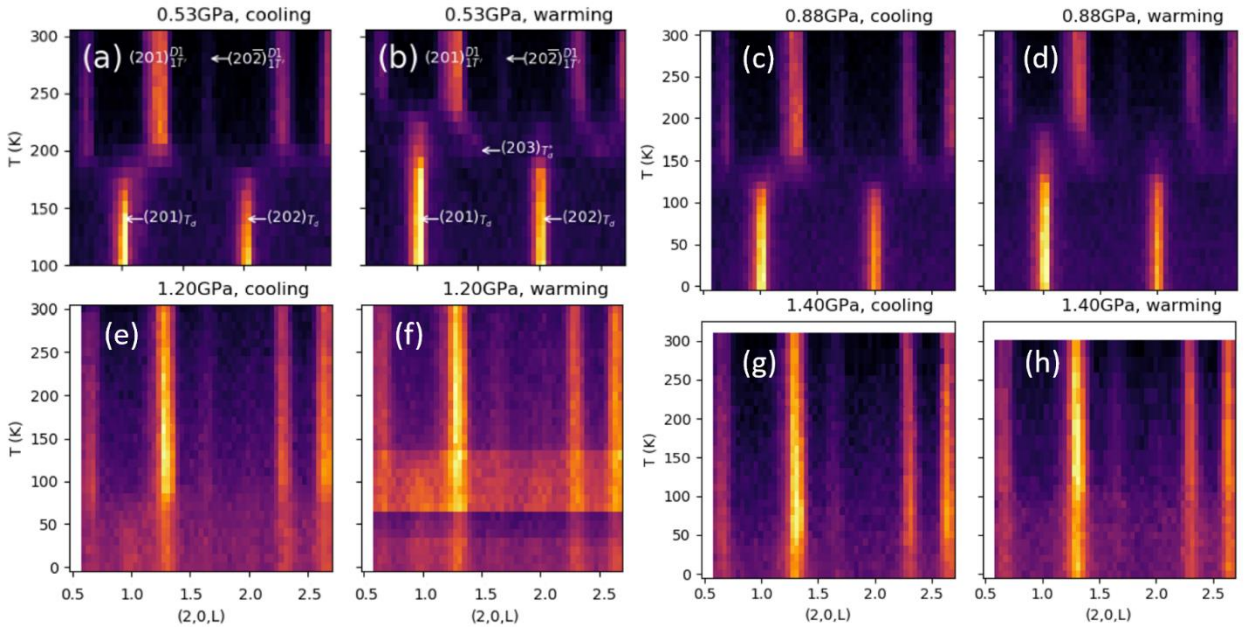

Fig. 8.1 Combined scans of neutron scattering intensity along (2, 0, L) for the $Mo_{0.8}W_{0.2}Te_2$ crystal collected under 0.53, 0.88, 1.20 and 1.40 GPa. It is noted that there is a glitch in the 1.20 GPa data on warming, which was caused by a temporary loss of the signal, and the data between 70 and 140 K were taken on a second warming and overplotted with the data collected on a first warming.

At 0.53 GPa, the transition in $Mo_{0.8}W_{0.2}Te_2$ shows similar features as for lower W-fraction crystals measured at ambient pressure. On warming (Fig. 8.1 (b)), the T_d* phase is indicated by the presence of a Bragg peak at (2,0,1.5) near 200 K. Further warming results in V-shaped diffuse scattering, then the 1T' phase. On cooling, V-shaped diffuse scattering was observed, followed by a transition into T_d. Similar behavior can be seen at 0.88 GPa, with some broadening of the transition temperature range. By 1.20 GPa, however, the T_d* phase is absent, replaced by phase coexistence between a small fraction of T_d (as seen from the intensity near (2,0,1) on cooling) and the dominant 1T' phase at the lowest temperatures. At 1.40 GPa, only the 1T' phase remains. As with pure $MoTe_2$ measured under pressure [50], the temperature range of the transition tends to be broader on warming than on cooling.

8.3 Pressure-temperature phase diagram

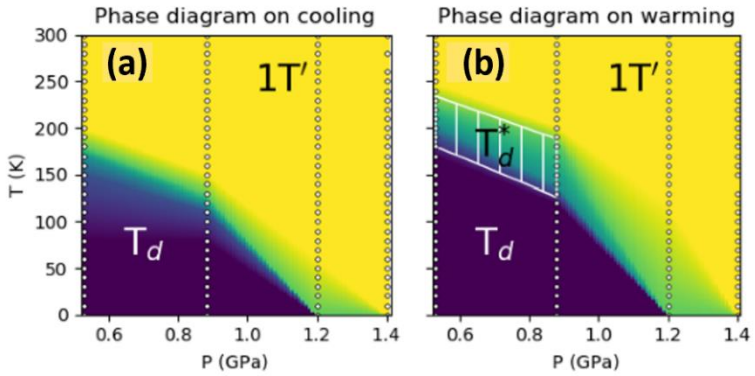

Fig. 8.2 Pressure-temperature phase diagrams of $Mo_{0.8}W_{0.2}Te_2$, where T_d* region is indicated by the white quadrilateral. The white circles indicate temperatures and pressures where measurements were taken.

Pressure-temperature phase diagrams deduced from scans along (2, 0, L) are shown in Fig. 8.2. The phase diagrams contain three useful information. First, the T_d-1T' transition temperature decreases roughly uniformly with pressure and the T_d phase disappears by 1.4 GPa. Second, the T_d* phase is only seen on warming up to 0.88 GPa and disappears with pressure between 0.88 and 1.20 GPa. No T_d* phase is present on cooling. Third, the temperature range of the transition is broadened with pressure, in contrast to the roughly constant transition temperature range with increased W-doping at ambient pressure.

8.4 β and δ parameters under pressure

In Fig. 8.3 (a, b) the β and the δ parameters extracted from elastic neutron scattering measurements on the $Mo_{0.8}W_{0.2}Te_2$ single crystal under pressure, and on multiple $Mo_{1-x}W_xTe_2$ single crystals at ambient pressure discussed in chapters 6 are plotted as a function of c_{300K}, which is the c lattice constant at 300 K. Elastic neutron scattering measurements on MT3 under pressure are also included, the values of β and δ for MT3 under pressure were extracted from the data reported in Ref. [50]. The values of c_{300K} for the ambient pressure data were obtained from longitudinal neutron scattering scans along the (002) or (004) Bragg peak; for data taken under pressure, c_{300K} was obtained from sample alignment at 300 K. As shown in Fig. 8.3, W-substitution and pressure have opposite effects on β and δ. β and δ decrease with increasing c_{300K}, whether the increases in c_{300K} are due to decreased pressure or increased W-substitution. These trends are also consistent with those reported in the literature for W-substitution [100] and pressure [28, 93]. The W-substitution of $Mo_{0.8}W_{0.2}Te_2$ decreases the measured β and δ parameters when comparing points at similar pressures (i.e., 0.60 GPa for MT3 vs. 0.55 GPa for $Mo_{0.8}W_{0.2}Te_2$), as expected.

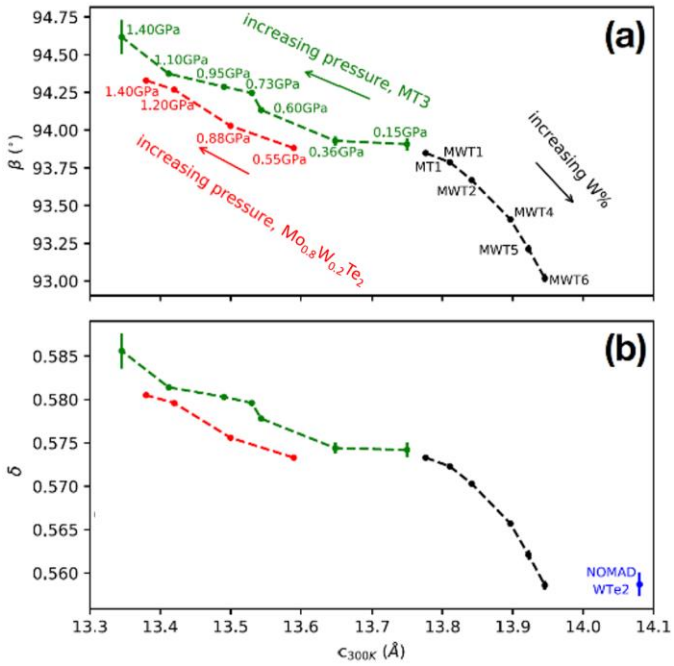

Fig. 8.3 Changes in (a) monoclinic angle β for 1T' and (b) stacking parameter δ plotted against c_{300K} from elastic neutron scattering measurements at ambient pressure on $Mo_{1-x}W_xTe_2$, under pressure for MT3 and $Mo_{0.8}W_{0.2}Te_2$. These data were taken on SPINS (MWT6), HB1A (other ambient-pressure data), or HB1 (pressure-dependence data).

8.5 Discussion

W-substitution and pressure have opposite effects on the T_d-1T' transition temperature in $Mo_{1-x}W_xTe_2$. The transition temperature increases with W-substitution and decrease with pressure. This is because W has a larger atomic size than Mo, doping $MoTe_2$ with W is equivalent to applying a negative chemical pressure to the lattice, which increases the size of the unit cell. In addition, changes in the transition behavior with pressure also provide insight into changes in interactions beyond nearest neighboring layers. While the temperature range of the transition is roughly constant as a function of W-fraction at ambient pressure, this range increases with pressure. Beyond a certain critical pressure, the T_d* phase is no longer present, and a phase-coexistence-like

behavior takes over. Some of these trends have theoretical confirmation. Enthalpy calculations show that the 1T' phase is favored at high pressure [93]. However, no theoretical explanation for how the transition unfolds under pressure, including the hysteresis, stacking disorder, or presence of a T_d* phase, has been reported.

8.6 Summary

The structural phase transition in a single crystal of $Mo_{0.8}W_{0.2}Te_2$ between the T_d, T_d* and 1T' phases as a function of pressure was investigated. With increasing pressure, the T_d-1T' transition temperature decreases and β and δ parameters increase. The T_d phase is suppressed with pressure and is no longer visible by 1.4 GPa. The T_d-1T' transition in $Mo_{0.8}W_{0.2}Te_2$ is accompanied with the T_d* phase on warming under relatively low pressure (up to 0.88 GPa) and T_d* disappears at pressure between 0.88 and 1.20 GPa. Increasing pressure leads to a change between one type of transition, with a T_d* phase and V-shaped diffuse scattering, to another type of transition with phase coexistence between T_d and 1T'. The transition temperature range also broadens with pressure.

Chapter 9

Discussion

9.1 Evolution of T_d* with W-substitution

In the $Mo_{1-x}W_xTe_2$ system, despite the symmetry equivalence of the positioning of neighboring layers (either A- or B-type of stacking), certain types of stacking sequences are clearly favorable over others, depending on the temperature and thermal history. For $MoTe_2$, two onset transition temperatures can be defined, T_1 and T_2. T_1 is the onset temperature from T_d to T_d* on warming, and from frustrated T_d* region to T_d on cooling. T_2 is the onset temperature from T_d* to V-shaped diffuse scattering on warming, and from 1T' to V-shaped diffuse scattering on cooling. In Fig. 9.1, a schematic diagram of the transitions as a function of increasing W-fraction from $MoTe_2$ to WTe_2 is provided. For crystals with low W fractions that include $MoTe_2$, phase boundaries are marked by the T_1 and T_2, as shown in Fig. 9.1 (a, b). Both temperatures are assumed to be the same on cooling vs. warming for simplicity (though there is a ~5 K hysteresis for the onset to or from T_d [80]). T_1 and T_2 determine the boundaries for temperature ranges where certain types of short-range stacking are preferred. For $T > T_2$, ABABAB... stacking is preferred. For $T < T_1$, AAAAAA... stacking is preferred. For $T_1 < T < T_2$, AABBAABB... stacking is preferred. However, T_d* is often frustrated on cooling.

With W substitution, T_1 and T_2 onset temperatures move closer together, as seen in Fig. 9.1 (c, d), for $Mo_{1-x}W_xTe_2$ with small x. On warming, the T_d* temperature range appears to shrink, which explains the disappearance of T_d* beyond x = 0.21. On cooling, the V-shaped diffuse scattering becomes abbreviated, and the 1T' intensities only slightly shift toward L = 2.5. Eventually, T_1 and T_2 merge, as shown in Fig. 9.1 (e, f), and the transition behavior becomes more phase-coexistence-

like, which is seen in $Mo_{1-x}W_xTe_2$ crystals with intermediate x and also WTe_2. In this way, W substitution would not just increase the overall temperature of the transition, but also change each onset temperature separately in ways that control which types of stacking are favorable.

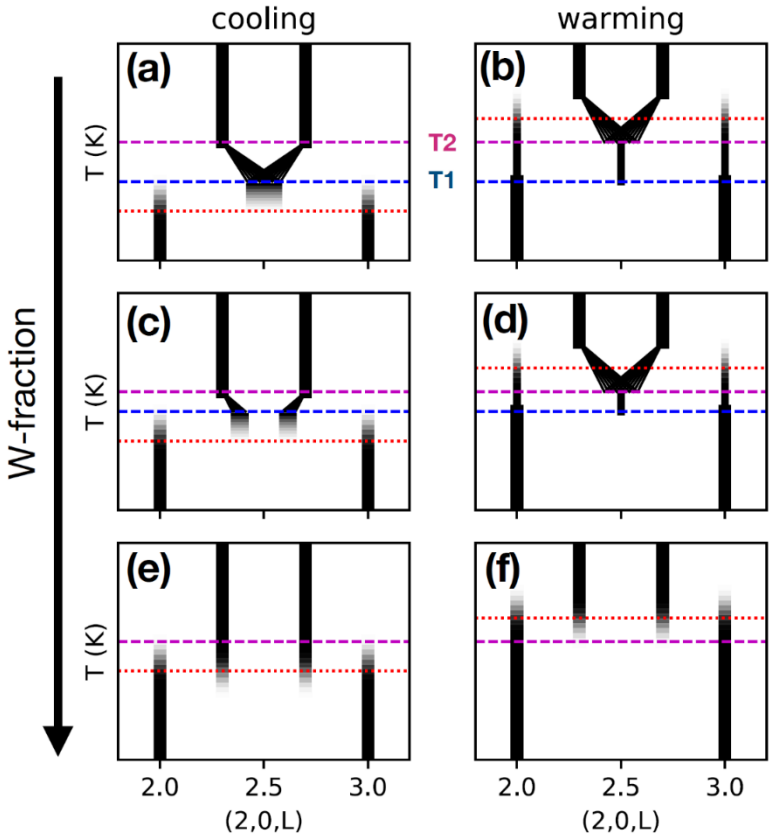

Fig. 9.1 Schematic diagrams showing the transition pictures on cooling and warming in $Mo_{1-x}W_xTe_2$ for three levels of W-substitution: (a, b) x = 0 as in $MoTe_2$, (c, d) x ~ 0.2, where T_d* is about to distinguish, and (e, f) $0.4 \leq x \leq 1.0$, where WTe_2 is included.

9.2 Phase diagram from $MoTe_2$ to WTe_2

The T_d-1T' transition in WTe_2 is added to the phase diagram shown earlier in Fig. 6.6 (c, d) and completed phase diagrams of $Mo_{1-x}W_xTe_2$ as a function of W fraction and temperature are shown in Fig. 9.2. The transition temperature overall increases continuously as a function of composition

from $MoTe_2$ to WTe_2. The narrowness of the WTe_2 transition is striking relative to the broadness of the transition near x ~0.5. Clearly, more research is needed from $0.5 < x < 1$ to clarify how the narrow transition of WTe_2 connects with the broader, hysteretic transition near x ~0.5.

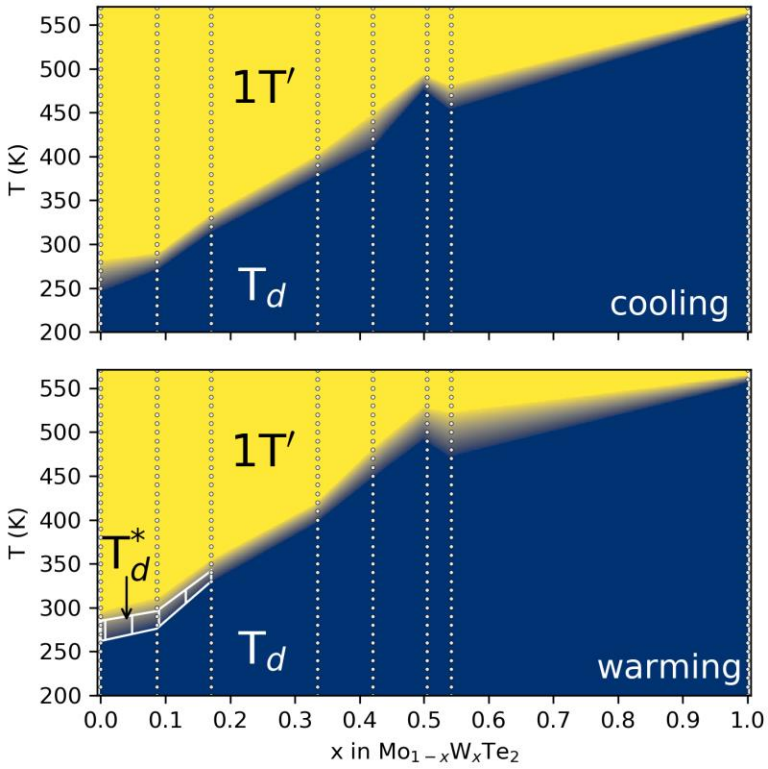

Fig. 9.2 Phase diagram of $Mo_{1-x}W_xTe_2$ as a function of temperature and W-fraction on warming and cooling. Dots denote where data were taken.

Chapter 10

Conclusion

Topological Weyl semimetals are a class of novel quantum materials that exhibit bulk Weyl fermions connected by topological surface Fermi arcs. Among these materials, the TMDs $MoTe_2$ and WTe_2 are unique since their 2D layered structure shows great potential for applications. With high electron mobility and large MR, $MoTe_2$ and WTe_2 can be employed in high-speed electronics and spintronics. In order to better understand the Weyl physics present in $MoTe_2$ and WTe_2, their crystal structures must be understood as the breaking of the inversion symmetry is a prerequisite for Weyl fermions to emerge.

The structural phase transition in $Mo_{1-x}W_xTe_2$ was investigated using neutron and X-ray scattering to reveal a layer sliding mechanism during the T_d-1T' transition that is accompanied by stacking disorder. In $MoTe_2$, upon warming from the orthorhombic T_d phase, a cell doubling structure T_d* was observed. The T_d* structure is pseudo-orthorhombic with a centrosymmetric space group, indicating that it is topologically trivial. In contrast, on cooling from 1T' to T_d, only diffuse scattering was observed across the phase boundary, the intensity of which suggests a frustrated tendency toward T_d*. Therefore, the transitions from T_d to T_d* on warming, and from the frustrated T_d* region to T_d on cooling, are coupled with Weyl node creation or annihilation.

Doping $MoTe_2$ or applying external strain are two effective approaches to engineer the electronic band structure and controlled transitions between T_d and 1T'. Given the complexity of the temperature dependence of the structures of $MoTe_2$, the structural phase diagram of $Mo_{1-x}W_xTe_2$ for x up to 0.54 was explored. With increased W substitution, the T_d-1T' transition temperature increases. The complex transition behavior that involves T_d* and substantial diffuse scattering

transforms into a phase coexistence behavior between T_d and 1T', and the T_d* phase disappears by $x \approx 0.34$. Meanwhile, hydrostatic pressure decreases the T_d-1T' transition temperature in $Mo_{0.8}W_{0.2}Te_2$. The T_d* phase is no longer visible with pressure between 0.88 and 1.20 GPa. These results suggest that the inversion symmetry breaking mechanism for intermediate W-doped $Mo_{1-x}W_xTe_2$ at ambient pressure, and for $Mo_{0.8}W_{0.2}Te_2$ at pressure near 1.20 GPa, is different from that of $MoTe_2$, which proceeds in a more direct way between 1T' and T_d without intermediate phases.

Surprisingly, in the Weyl semimetal WTe_2, where a structural phase transition has been proposed to be absent, a T_d-1T' structural phase transition was observed at ambient pressure. In single crystal, the transition occurs at 565 K without hysteresis, but in powder, the transition is broadened and incomplete up to 700 K. The different transitions in powders and single crystals highlights the importance of sample-dependent factors. It is possible that Te vacancies from evaporation play a role. A better understanding of sample-dependent factors that influence the sliding layer transition may help realize the potential of stacking changes to influence properties in quasi-two-dimensional materials.

In light of the observation a T_d* phase in $MoTe_2$ and a T_d-1T' transition in WTe_2, this work changes the current interpretation on the experimental data of $Mo_{1-x}W_xTe_2$ and requires further theoretical explanations on the structural behavior in $Mo_{1-x}W_xTe_2$. For instance, evidence of the T_d* phase is also seen from reported resistivity data on $MoTe_2$. The hysteresis loop in resistivity (first reported in Ref. [113]) has been interpreted as indicating the transition between T_d and 1T', but in view of the current data, most of the change in the resistance occurs between T_d and T_d* on warming. Thus, the T_d-1T' transition in $MoTe_2$ has complex structural behavior and deserves further study.

This work might also provide ideas to help explain other properties seen in $Mo_xW_{1-x}Te_2$ that are still debatable. For instance, there are several explanations for the origin of the XMR in WTe_2 observed at low temperatures [38, 103, 114], the number and location of Weyl points in the T_d phase [115], and the topological nature of the observed surface Fermi arcs that are a necessary but not sufficient condition for a Weyl semimetal [116] for $MoTe_2$. In addition, ARPES measurements could also be performed in the T_d* phase will provide useful insight into how Weyl nodes disappear across the phase boundary. This work may also inform proposed applications, such as the photoinduced ultrafast topological switch discussed in Ref. [117]. Since the $T_d \rightarrow T_d^* \rightarrow T_d$ transition occurs without disorder and with only a ~5 K hysteresis, and since T_d* appears to be centrosymmetric, a topological switch may more efficiently use T_d* rather than 1T'.

Though current theories on the structural phase transitions in $Mo_{1-x}W_xTe_2$ lack predictions of an intermediate T_d* phase, and a T_d-1T' transition in WTe_2, they still provide useful information that help understand the different hysteresis observed across the structural phase transitions in $MoTe_2$ and WTe_2. For $MoTe_2$, DFT calculations indicate the relative stability of 1T' over T_d at higher temperatures [45, 93], which is attributed to the phonon entropy contribution (with a lack of soft mode behavior noted) [93]. Meanwhile, WTe_2 is predicted not to have a transition up to at least 500 K, and likely much higher. However, the calculations for WTe_2 show a lack of an energy barrier between 1T' and T_d, in contrast to $MoTe_2$, which may be related to the lack of hysteresis in WTe_2, but not in $MoTe_2$ [45]. It is possible that if a more accurate calculation is performed with phonon anharmonicity accounted, similar to Ref. [93], the results may suggest a similar reason for the existence of 1T' in WTe_2 at higher temperatures.

As for the microscopic origin of the layer shifts between different phase of $Mo_{1-x}W_xTe_2$, unfortunately, little theoretical analysis has been attempted beyond calculating the free energy of

T_d and 1T' [45, 93]. Assuming the sequence of stacking changes on warming and cooling occur due to becoming energetically preferable, it would be interesting to know how the free energy changes for structures with arbitrary stacking patterns, including for disordered stacking, which might provide insights as why different diffuse scattering patterns are seen in $Mo_{1-x}W_xTe_2$ with different W-levels, and why the transition behavior is different on warming vs. cooling for $MoTe_2$. However, it is noted that there is the inherent difficulty in calculating the very small free-energy differences between structures which differ only in the stacking of weakly interacting layers.

More generally, it would also be good to know what the dominant drivers of stacking changes are, whether changes in crystal vibrations or band structure is more important. Whatever the source of the effective interlayer interaction, it should be long-range enough to account for the gradual reduction in stacking defects (likely due to annihilating twin boundaries) on cooling into T_d or warming into 1T' [49]. In fact, such gradual decrease in diffuse scattering that was observed from neutron scattering is also supported by some hysteresis effects that extend far beyond the transition region seen in resistivity measurements [92]. However, these effects have been largely ignored, though one of the surface Fermi arcs was noted to persist to ~90 K above the transition temperature and to have a history-dependent appearance [115].

One possible future direction to further investigate the structural phase transitions in $Mo_{1-x}W_xTe_2$ is to look at changes of the disordered stacking over time. For example, if temperature is fixed at which the $MoTe_2$ crystal is in the V-shaped diffuse scattering region seen on cooling, it would be interesting to know whether the crystal will eventually transform into an ordered phase of T_d*, T_d or 1T'. This is because at 270 K on warming, the ordered T_d* phase was observed with no changes in the stacking over a time period of several days (typical duration for a neutron scattering measurement), which suggests that T_d* is energetically favorable at this temperature. Then, a

disorder-order transition might be expected from the V-shaped diffuse scattering region over a longer time.

Another interesting idea is to look at uniaxial pressure (along the c-axis) induced structural phase transition in $MoTe_2$. While hydrostatic pressure has been shown to decrease the transition temperature [28]. Tensile strain along the a- or b-axes has been reported to, respectively, decrease and increase the transition temperature [112]. The effect of non-hydrostatic stresses on $MoTe_2$, however, has not been studied with diffraction techniques, and the question remains of how a uniaxial stress along the c-axis would affect structural properties. $MoTe_2$ is much more compressible along the c-axis than along the a- or b-axes, so it is expected that changes with uniaxial pressure along the c-axis may have more effects on the interlayer interactions that give rise to the transition between 1T' and T_d.

In addition, some other materials with reversible temperature-induced sliding layer transitions that have been reported include $CrCl_3$ [118], α-$RuCl_3$ [56], Bi_4I_4 [57], Ta_2NiSe_5 [119] and In_2Se_3 [120, 121]. A better understanding of these types of transitions in $Mo_{1-x}W_xTe_2$ might also lead to the discovery of new phases in other materials.

Bibliography

[1] K. S. Novoselov, A. K. Geim, S. V. Morozov, D. Jiang, Y. Zhang, S. V. Dubonos, I. V. Grigorieva, and A. A. Firsov, Electric Field Effect in Atomically Thin Carbon Films, Science 306, 666 (2004).

[2] D. Akinwande, C. Huyghebaert, C.-H. Wang, M. I. Serna, S. Goossens, L.-J. Li, H.-S. P. Wong, and F. H. L. Koppens, Graphene and Two-Dimensional Materials for Silicon Technology, Nature 573, 7775 (2019).

[3] Z. Niu, L. Zhang, L. Liu, B. Zhu, H. Dong, and X. Chen, All-Solid-State Flexible Ultrathin Micro-Supercapacitors Based on Graphene, Advanced Materials 25, 4035 (2013).

[4] A. K. Geim and K. S. Novoselov, The Rise of Graphene, Nature Mater 6, 3 (2007).

[5] A. H. Castro Neto, F. Guinea, N. M. R. Peres, K. S. Novoselov, and A. K. Geim, The Electronic Properties of Graphene, Rev. Mod. Phys. 81, 109 (2009).

[6] Press release. NobelPrize.org. https://www.nobelprize.org/prizes/physics/2010/press-release/

[7] Y. Zhang, Y.-W. Tan, H. L. Stormer, and P. Kim, Experimental Observation of the Quantum Hall Effect and Berry's Phase in Graphene, Nature 438, 7065 (2005).

[8] Y. Cao, V. Fatemi, S. Fang, K. Watanabe, T. Taniguchi, E. Kaxiras, and P. Jarillo-Herrero, Unconventional Superconductivity in Magic-Angle Graphene Superlattices, Nature 556, 7699 (2018).

[9] J. A. Wilson and A. D. Yoffe, The Transition Metal Dichalcogenides Discussion and Interpretation of the Observed Optical, Electrical and Structural Properties, Advances in Physics 18, 193 (1969).

[10] S. Z. Butler et al., Progress, Challenges, and Opportunities in Two-Dimensional Materials Beyond Graphene, ACS Nano 7, 2898 (2013).

[11] S. Manzeli, D. Ovchinnikov, D. Pasquier, O. V. Yazyev, and A. Kis, 2D Transition Metal Dichalcogenides, Nat Rev Mater 2, 8 (2017).

[12] P. Avouris, Graphene: Electronic and Photonic Properties and Devices, Nano Lett. 10, 4285 (2010).

[13] Q. H. Wang, K. Kalantar-Zadeh, A. Kis, J. N. Coleman, and M. S. Strano, Electronics and Optoelectronics of Two-Dimensional Transition Metal Dichalcogenides, Nature Nanotech 7, 11 (2012).

[14] National Center for Biotechnology Information. "PubChem Periodic Table of Elements" PubChem, https://pubchem.ncbi.nlm.nih.gov/periodic-table/.

[15] M. Pumera, Z. Sofer, and A. Ambrosi, Layered Transition Metal Dichalcogenides for Electrochemical Energy Generation and Storage, J. Mater. Chem. A 2, 8981 (2014).

[16] A. Ramasubramaniam, D. Naveh, and E. Towe, Tunable Band Gaps in Bilayer Transition-Metal Dichalcogenides, Phys. Rev. B 84, 205325 (2011).

[17] M. Chhowalla, D. Jena, and H. Zhang, Two-Dimensional Semiconductors for Transistors, Nat Rev Mater 1, 11 (2016).

[18] W. Choi, N. Choudhary, G. H. Han, J. Park, D. Akinwande, and Y. H. Lee, Recent Development of Two-Dimensional Transition Metal Dichalcogenides and Their Applications, Materials Today 20, 116 (2017).

[19] M. Chhowalla, H. S. Shin, G. Eda, L.-J. Li, K. P. Loh, and H. Zhang, The Chemistry of Two-Dimensional Layered Transition Metal Dichalcogenide Nanosheets, Nature Chem 5, 4 (2013).

[20] D. Voiry, A. Mohite, and M. Chhowalla, Phase Engineering of Transition Metal Dichalcogenides, Chemical Society Reviews 44, 2702 (2015).

[21] Y. Li, K.-A. N. Duerloo, K. Wauson, and E. J. Reed, Structural Semiconductor-to-Semimetal Phase Transition in Two-Dimensional Materials Induced by Electrostatic Gating, Nat Commun 7, 1 (2016).

[22] W. Zhao, Z. Ghorannevis, L. Chu, M. Toh, C. Kloc, P.-H. Tan, and G. Eda, Evolution of Electronic Structure in Atomically Thin Sheets of WS2 and WSe2, ACS Nano 7, 791 (2013).

[23] Y. Li, H. Wang, L. Xie, Y. Liang, G. Hong, and H. Dai, MoS2 Nanoparticles Grown on Graphene: An Advanced Catalyst for the Hydrogen Evolution Reaction, J. Am. Chem. Soc. 133, 7296 (2011).

[24] Y. Sun, S.-C. Wu, M. N. Ali, C. Felser, and B. Yan, Prediction of Weyl Semimetal in Orthorhombic MoTe2, Phys. Rev. B 92, 161107 (2015).

[25] K. Deng et al., Experimental Observation of Topological Fermi Arcs in Type-II Weyl Semimetal MoTe2, Nature Phys 12, 12 (2016).

[26] L. Huang et al., Spectroscopic Evidence for a Type II Weyl Semimetallic State in MoTe2, Nature Mater 15, 11 (2016).

[27] P. Li, Y. Wen, X. He, Q. Zhang, C. Xia, Z.-M. Yu, S. A. Yang, Z. Zhu, H. N. Alshareef, and X.-X. Zhang, Evidence for Topological Type-II Weyl Semimetal WTe2, Nat Commun 8, 1 (2017).

[28] Y. Qi et al., Superconductivity in Weyl Semimetal Candidate MoTe2, Nat Commun 7, 1 (2016).

[29] M. N. Ali et al., Large, Non-Saturating Magnetoresistance in WTe2, Nature 514, 7521 (2014).

[30] F. C. Chen, H. Y. Lv, X. Luo, W. J. Lu, Q. L. Pei, G. T. Lin, Y. Y. Han, X. B. Zhu, W. H. Song, and Y. P. Sun, Extremely Large Magnetoresistance in the Type-II Weyl Semimetal MoTe2, Phys. Rev. B 94, 235154 (2016).

[31] B. Yan and C. Felser, Topological Materials: Weyl Semimetals, Annual Review of Condensed Matter Physics 8, 337 (2017).

[32] A. A. Soluyanov, D. Gresch, Z. Wang, Q. Wu, M. Troyer, X. Dai, and B. A. Bernevig, Type-II Weyl Semimetals, Nature 527, 7579 (2015).

[33] N. P. Armitage, E. J. Mele, and A. Vishwanath, Weyl and Dirac Semimetals in Three-Dimensional Solids, Rev. Mod. Phys. 90, 015001 (2018).

[34] T. Ojanen, Helical Fermi Arcs and Surface States in Time-Reversal Invariant Weyl Semimetals, Phys. Rev. B 87, 245112 (2013).

[35] Y. Wu, D. Mou, N. H. Jo, K. Sun, L. Huang, S. L. Bud'ko, P. C. Canfield, and A. Kaminski, Observation of Fermi Arcs in the Type-II Weyl Semimetal Candidate WTe2, Phys. Rev. B 94, 121113 (2016).

[36] I. Belopolski et al., Fermi Arc Electronic Structure and Chern Numbers in the Type-II Weyl Semimetal Candidate MoxW1-xTe2, Phys. Rev. B 94, 085127 (2016).

[37] J. Augustin, V. Eyert, Th. Böker, W. Frentrup, H. Dwelk, C. Janowitz, and R. Manzke, Electronic Band Structure of the Layered Compound Td-WTe2, Phys. Rev. B 62, 10812 (2000).

[38] Q. Zhou, D. Rhodes, Q. R. Zhang, S. Tang, R. Schönemann, and L. Balicas, Hall Effect within the Colossal Magnetoresistive Semimetallic State of MoTe2, Phys. Rev. B 94, 121101 (2016).

[39] Y.-Y. Lv et al., Composition and Temperature-Dependent Phase Transition in Miscible Mo1-xWxTe2 Single Crystals, Sci Rep 7, 1 (2017).

[40] S. J. Zelewski and R. Kudrawiec, Photoacoustic and Modulated Reflectance Studies of Indirect and Direct Band Gap in van Der Waals Crystals, Sci Rep 7, 1 (2017).

[41] D. H. Keum et al., Bandgap Opening in Few-Layered Monoclinic MoTe2, Nature Phys 11, 6 (2015).

[42] I. G. Lezama, A. Arora, A. Ubaldini, C. Barreteau, E. Giannini, M. Potemski, and A. F. Morpurgo, Indirect-to-Direct Band Gap Crossover in Few-Layer MoTe2, Nano Lett. 15, 2336 (2015).

[43] R. Clarke, E. Marseglia, and H. P. Hughes, A Low-Temperature Structural Phase Transition in β-MoTe2, Philosophical Magazine B 38, 121 (1978).

[44] D. Kang et al., Superconductivity Emerging from a Suppressed Large Magnetoresistant State in Tungsten Ditelluride, Nat Commun 6, 1 (2015).

[45] H.-J. Kim, S.-H. Kang, I. Hamada, and Y.-W. Son, Origins of the Structural Phase Transitions in MoTe2 and WTe2, Phys. Rev. B 95, 180101 (2017).

[46] J. Xia, D.-F. Li, J.-D. Zhou, P. Yu, J.-H. Lin, J.-L. Kuo, H.-B. Li, Z. Liu, J.-X. Yan, and Z.-X. Shen, Pressure-Induced Phase Transition in Weyl Semimetallic WTe2, Small 13, 1701887 (2017).

[47] Y. Zhou et al., Pressure-Induced Td to 1T′ Structural Phase Transition in WTe2, AIP Advances 6, 075008 (2016).

[48] A. N. Berger et al., Temperature-Driven Topological Transition in 1T'-MoTe2, Npj Quant Mater 3, 1 (2018).

[49] J. A. Schneeloch, Y. Tao, C. Duan, M. Matsuda, A. A. Aczel, J. A. Fernandez-Baca, G. Xu, J. C. Neuefeind, J. Yang, and D. Louca, Evolution of the Structural Transition in Mo1-xWxTe2, Phys. Rev. B 102, 054105 (2020).

[50] S. Dissanayake, C. Duan, J. Yang, J. Liu, M. Matsuda, C. Yue, J. A. Schneeloch, J. C. Y. Teo, and D. Louca, Electronic Band Tuning under Pressure in MoTe2 Topological Semimetal, Npj Quantum Mater. 4, 1 (2019).

[51] Y. Wang et al., Structural Phase Transition in Monolayer MoTe2 Driven by Electrostatic Doping, Nature 550, 7677 (2017).

[52] S. Song, D. H. Keum, S. Cho, D. Perello, Y. Kim, and Y. H. Lee, Room Temperature Semiconductor–Metal Transition of MoTe2 Thin Films Engineered by Strain, Nano Lett. 16, 188 (2016).

[53] P. Li et al., Phase Transition and Superconductivity Enhancement in Se-Substituted MoTe2 Thin Films, Advanced Materials 31, 1904641 (2019).

[54] X.-J. Yan, Y.-Y. Lv, L. Li, X. Li, S.-H. Yao, Y.-B. Chen, X.-P. Liu, H. Lu, M.-H. Lu, and Y.-F. Chen, Composition Dependent Phase Transition and Its Induced Hysteretic Effect in the Thermal Conductivity of WxMo1−xTe2, Appl. Phys. Lett. 110, 211904 (2017).

[55] M. A. McGuire, Crystal and Magnetic Structures in Layered, Transition Metal Dihalides and Trihalides, Crystals 7, 5 (2017).

[56] A. Glamazda, P. Lemmens, S.-H. Do, Y. S. Kwon, and K.-Y. Choi, Relation between Kitaev Magnetism and Structure in α-RuCl3, Phys. Rev. B 95, 174429 (2017).

[57] R. Noguchi et al., A Weak Topological Insulator State in Quasi-One-Dimensional Bismuth Iodide, Nature 566, 7745 (2019).

[58] J. A. Schneeloch, C. Duan, J. Yang, J. Liu, X. Wang, and D. Louca, Emergence of Topologically Protected States in the MoTe2 Weyl Semimetal with Layer-Stacking Order, Phys. Rev. B 99, 161105 (2019).

[59] J. Chadwick, Possible Existence of a Neutron, Nature 129, 3252 (1932).

[60] S. W. Lovesey, Theory of Neutron Scattering from Condensed Matter (Clarendon Press, United Kingdom, 1984).

[61] Press release. NobelPrize.org. https://www.nobelprize.org/prizes/physics/1994/press-release/

[62] G. L. Squires, Introduction to the Theory of Thermal Neutron Scattering (Courier Corporation, 1996).

[63] J. Chadwick, The Neutron and Its Properties, BJR 6, 24 (1933).

[64] B. T. M. Willis and C. J. Carlile, Experimental Neutron Scattering (Oxford University Press, 2017).

[65] M. Yethiraj and J. A. Fernandez-Baca, Neutron Scattering at the High Flux Isotope Reactor at Oak Ridge National Laboratory, MRS Online Proceedings Library (OPL) 376, 59 (1994).

[66] J. S. Nico, M. Arif, M. S. Dewey, T. R. Gentile, D. M. Gilliam, P. R. Huffman, D. L. Jacobson, and A. K. Thompson, The Fundamental Neutron Physics Facilities at NIST, J Res Natl Inst Stand Technol 110, 137 (2005).

[67] T. E. Mason et al., The Spallation Neutron Source in Oak Ridge: A Powerful Tool for Materials Research, Physica B: Condensed Matter 385–386, 955 (2006).

[68] G. Shirane, S. M. Shapiro, and J. M. Tranquada, Neutron Scattering with a Triple-Axis Spectrometer: Basic Techniques (Cambridge University Press, 2002).

[69] E. Mamontov and K. W. Herwig, A Time-of-Flight Backscattering Spectrometer at the Spallation Neutron Source, BASIS, Review of Scientific Instruments 82, 085109 (2011).

[70] Z. Yamani, Z. Tun, and D. H. Ryan, Neutron Scattering Study of the Classical Antiferromagnet MnF2: A Perfect Hands-on Neutron Scattering Teaching Course Special Issue on Neutron Scattering in Canada., Can. J. Phys. 88, 771 (2010).

[71] G. Cicognani, H. Mutka, and F. Sacchetti, The Thermal Neutron Time-of-Flight Spectrometer IN4C, Physica B: Condensed Matter 276–278, 83 (2000).

[72] B. E. Warren, X-Ray Diffraction (Courier Corporation, 1990).

[73] M. Grimaldo, F. Roosen-Runge, F. Zhang, F. Schreiber, and T. Seydel, Dynamics of Proteins in Solution, Quarterly Reviews of Biophysics 52, e7 (2019).

[74] G. E. M. Jauncey, The Scattering of X-Rays and Bragg's Law, Proceedings of the National Academy of Sciences 10, 57 (1924).

[75] W. H. Bragg and S. W. L. Bragg, X Rays and Crystal Structure (G. Bell and Sons, Limited, 1915).

[76] W. H. McMaster, N. K. Del Grande, J. H. Mallett, and J. H. Hubbell, COMPILATION OF X-RAY CROSS SECTIONS., No. UCRL-50174(Sec.2)(Rev.1), California Univ., Livermore. Lawrence Radiation Lab., 1969.

[77] V. F. Sears, Neutron Scattering Lengths and Cross Sections, Neutron News 3, 26 (1992).

[78] Y. Ren and X. Zuo, Synchrotron X-Ray and Neutron Diffraction, Total Scattering, and Small-Angle Scattering Techniques for Rechargeable Battery Research, Small Methods 2, 1800064 (2018).

[79] D. Rhodes et al., Engineering the Structural and Electronic Phases of MoTe2 through W Substitution, Nano Lett. 17, 1616 (2017).

[80] Y. Tao, J. A. Schneeloch, C. Duan, M. Matsuda, S. E. Dissanayake, A. A. Aczel, J. A. Fernandez-Baca, F. Ye, and D. Louca, Appearance of a Td* Phase across the Td-1T' Phase Boundary in the Weyl Semimetal MoTe2, Phys. Rev. B 100, 100101 (2019).

[81] Y. Tao, J. A. Schneeloch, A. A. Aczel, and D. Louca, Td to 1T' Structural Phase Transition in the WTe2 Weyl Semimetal, Phys. Rev. B 102, 060103 (2020).

[82] H. M. Rietveld, A Profile Refinement Method for Nuclear and Magnetic Structures, J Appl Cryst 2, 2 (1969).

[83] B. H. Toby and R. B. Von Dreele, GSAS-II: The Genesis of a Modern Open-Source All Purpose Crystallography Software Package, J Appl Cryst 46, 2 (2013).

[84] J. Goldstein, Practical Scanning Electron Microscopy: Electron and Ion Microprobe Analysis (Springer Science & Business Media, 2012).

[85] Y.-Y. Lv et al., Dramatically Decreased Magnetoresistance in Non-Stoichiometric WTe2 Crystals, Sci Rep 6, 1 (2016).

[86] S.-Y. Xu et al., Discovery of a Weyl Fermion Semimetal and Topological Fermi Arcs, Science 349, 613 (2015).

[87] Z. Wang, D. Gresch, A. A. Soluyanov, W. Xie, S. Kushwaha, X. Dai, M. Troyer, R. J. Cava, and B. A. Bernevig, MoTe2: A Type-II Weyl Topological Metal, Phys. Rev. Lett. 117, 056805 (2016).

[88] B. Q. Lv et al., Experimental Discovery of Weyl Semimetal TaAs, Phys. Rev. X 5, 031013 (2015).

[89] L. X. Yang et al., Weyl Semimetal Phase in the Non-Centrosymmetric Compound TaAs, Nature Phys 11, 9 (2015).

[90] K. Zhang, C. Bao, Q. Gu, X. Ren, H. Zhang, K. Deng, Y. Wu, Y. Li, J. Feng, and S. Zhou, Raman Signatures of Inversion Symmetry Breaking and Structural Phase Transition in Type-II Weyl Semimetal MoTe2, Nat Commun 7, 1 (2016).

[91] F. Ye, Y. Liu, R. Whitfield, R. Osborn, and S. Rosenkranz, Implementation of Cross Correlation for Energy Discrimination on the Time-of-Flight Spectrometer CORELLI, J Appl Cryst 51, 2 (2018).

[92] T. Zandt, H. Dwelk, C. Janowitz, and R. Manzke, Quadratic Temperature Dependence up to 50 K of the Resistivity of Metallic MoTe2, Journal of Alloys and Compounds 442, 216 (2007).

[93] C. Heikes et al., Mechanical Control of Crystal Symmetry and Superconductivity in Weyl Semimetal MoTe2, Phys. Rev. Materials 2, 074202 (2018).

[94] X.-J. Yan, Y.-Y. Lv, L. Li, X. Li, S.-H. Yao, Y.-B. Chen, X.-P. Liu, H. Lu, M.-H. Lu, and Y.-F. Chen, Investigation on the Phase-Transition-Induced Hysteresis in the Thermal Transport along the c-Axis of MoTe2, Npj Quant Mater 2, 1 (2017).

[95] R. He et al., Dimensionality-Driven Orthorhombic MoTe2 at Room Temperature, Phys. Rev. B 97, 041410 (2018).

[96] C. Cao, X. Liu, X. Ren, X. Zeng, K. Zhang, D. Sun, S. Zhou, Y. Wu, Y. Li, and J.-H. Chen, Barkhausen Effect in the First Order Structural Phase Transition in Type-II Weyl Semimetal MoTe2, 2D Mater. 5, 044003 (2018).

[97] S. Zhong, A. Tiwari, G. Nichols, F. Chen, X. Luo, Y. Sun, and A. W. Tsen, Origin of Magnetoresistance Suppression in Thin γ-MoTe2, Phys. Rev. B 97, 241409 (2018).

[98] T.-R. Chang et al., Prediction of an Arc-Tunable Weyl Fermion Metallic State in MoxW1-xTe2, Nat Commun 7, 1 (2016).

[99] I. Belopolski et al., Discovery of a New Type of Topological Weyl Fermion Semimetal State in MoxW1-xTe2, Nat Commun 7, 1 (2016).

[100] S. M. Oliver et al., The Structural Phases and Vibrational Properties of Mo1-xWxTe2 Alloys, 2D Mater. 4, 045008 (2017).

[101] A. Tamai et al., Fermi Arcs and Their Topological Character in the Candidate Type-II Weyl Semimetal MoTe2, Phys. Rev. X 6, 031021 (2016).

[102] H. Sakai, K. Ikeura, M. S. Bahramy, N. Ogawa, D. Hashizume, J. Fujioka, Y. Tokura, and S. Ishiwata, Critical Enhancement of Thermopower in a Chemically Tuned Polar Semimetal MoTe2, Science Advances 2, e1601378 (2016).

[103] D. Rhodes et al., Bulk Fermi Surface of the Weyl Type-II Semimetallic Candidate γ-MoTe2, Phys. Rev. B 96, 165134 (2017).

[104] F.-T. Huang, S. Joon Lim, S. Singh, J. Kim, L. Zhang, J.-W. Kim, M.-W. Chu, K. M. Rabe, D. Vanderbilt, and S.-W. Cheong, Polar and Phase Domain Walls with Conducting Interfacial States in a Weyl Semimetal MoTe2, Nat Commun 10, 1 (2019).

[105] S. Cho et al., Te Vacancy-Driven Superconductivity in Orthorhombic Molybdenum Ditelluride, 2D Mater. 4, 021030 (2017).

[106] S. Paul, S. Karak, M. Mandal, A. Ram, S. Marik, R. P. Singh, and S. Saha, Tailoring the Phase Transition and Electron-Phonon Coupling in 1T'-MoTe2 by Charge Doping: A Raman Study, Phys. Rev. B 102, 054103 (2020).

[107] Y. Wu, N. H. Jo, M. Ochi, L. Huang, D. Mou, S. L. Bud'ko, P. C. Canfield, N. Trivedi, R. Arita, and A. Kaminski, Temperature-Induced Lifshitz Transition in WTe2, Phys. Rev. Lett. 115, 166602 (2015).

[108] Y. Luo, H. Li, Y. M. Dai, H. Miao, Y. G. Shi, H. Ding, A. J. Taylor, D. A. Yarotski, R. P. Prasankumar, and J. D. Thompson, Hall Effect in the Extremely Large Magnetoresistance Semimetal WTe2, Appl. Phys. Lett. 107, 182411 (2015).

[109] D. Santos-Cottin, E. Martino, F. Le Mardelé, C. Witteveen, F. O. von Rohr, C. C. Homes, Z. Rukelj, and A. Akrap, Low-Energy Excitations in Type-II Weyl Semimetal Td-MoTe2 Evidenced through Optical Conductivity, Phys. Rev. Materials 4, 021201 (2020).

[110] P. Lu et al., Origin of Superconductivity in the Weyl Semimetal WTe2 under Pressure, Phys. Rev. B 94, 224512 (2016).

[111] Y. Ge, Z. Ding, W. Meng, J. Wang, Y. Hou, G. Wu, Q. Lu, and X. Yang, Uniaxial Negative Thermal Expansion and Band Renormalization in Monolayer Td-MoTe2 at Low Temperature, Phys. Rev. B 101, 104305 (2020).

[112] J. Yang, J. Colen, J. Liu, M. C. Nguyen, G. Chern, and D. Louca, Elastic and Electronic Tuning of Magnetoresistance in MoTe2, Science Advances 3, eaao4949 (2017).

[113] H. P. Hughes and R. H. Friend, Electrical Resistivity Anomaly in β-MoTe2(Metallic Behaviour), J. Phys. C: Solid State Phys. 11, L103 (1978).

[114] S. Thirupathaiah et al., MoTe2: An Uncompensated Semimetal with Extremely Large Magnetoresistance, Phys. Rev. B 95, 241105 (2017).

[115] A. P. Weber et al., Spin-Resolved Electronic Response to the Phase Transition in MoTe2, Phys. Rev. Lett. 121, 156401 (2018).

[116] N. Xu et al., Evidence of a Coulomb-Interaction-Induced Lifshitz Transition and Robust Hybrid Weyl Semimetal in Td-MoTe2, Phys. Rev. Lett. 121, 136401 (2018).

[117] M. Y. Zhang et al., Light-Induced Subpicosecond Lattice Symmetry Switch in MoTe2, Phys. Rev. X 9, 021036 (2019).

[118] J. A. Schneeloch, Y. Tao, Y. Cheng, L. Daemen, G. Xu, Q. Zhang, and D. Louca, Gapless Dirac Magnons in CrCl3, Npj Quantum Mater. 7, 1 (2022).

[119] A. Nakano et al., Pressure-Induced Coherent Sliding-Layer Transition in the Excitonic Insulator Ta2NiSe5, IUCrJ 5, 2 (2018).

[120] F. Ke et al., Interlayer-Glide-Driven Isosymmetric Phase Transition in Compressed In2Se3, Appl. Phys. Lett. 104, 212102 (2014).

[121] J. Zhao and L. Yang, Structure Evolutions and Metallic Transitions in In2Se3 Under High Pressure, J. Phys. Chem. C 118, 5445 (2014).